

https://dspace.org/

Unravelling the structureactivity relationship of porous binary metalbased electrocatalysts for green hydrogen evolution reaction

K Eid; Kenneth Ozoemena; Rajender S. Varma

ELSEVIER SCIENCE SA
https://hdl.handle.net/10539/46600
WOS

Downloaded from a DSpace repository. https://dspace.org/

Coordination Chemistry Reviews 523 (2025) 216238

Contents lists available at ScienceDirect

Coordination Chemistry Reviews

journal homepage: www.elsevier.com/locate/ccr

Review

Unravelling the structure-activity relationship of porous binary metal-based electrocatalysts for green hydrogen evolution reaction

Kamel Eid [a,*], Kenneth I. Ozoemena [b], Rajender S. Varma [c]

[a] Gas Processing Center (GPC), College of Engineering, Qatar University, Doha 2713, Qatar
[b] Molecular Science Institute, School of Chemistry, University of the Witwatersrand, Private Bag 3, PO Wits, Johannesburg, South Africa
[c] Centre of Excellence for Research in Sustainable Chemistry, Department of Chemistry, Federal University of São Carlos, 13565-905 São Carlos, SP, Brazil

ARTICLE INFO

Keywords:
Green hydrogen evolution
Porous metal carbides
Metal oxides
Nitrides
Metal phosphides
Metal chalcogenides

ABSTRACT

Green hydrogen (H_2) production through hydrogen evolution reaction (HER) via water splitting is deemed an efficient and sustainable fuel or energy carrier without environmental detriments. However, its higher cost remains the bottleneck in the commercialization process. Ubiquitously, porous binary metal-based catalysts so far remain the most active electrocatalysts for the HER, owing to their electronic effect, optimum hydrogen binding energy, and lower activation energies for H-desorption and recombination close to the thermodynamic potential. Despite plentiful efforts and developments, the engineering of porous binary metals for the HER still comprises numerous scientific problems to be unraveled, which still await deliberation. This review emphasizes the rational design of porous noble binary-metal-based electrocatalysts, porous transition binary-metal electrocatalysts (i.e., carbides/oxides, phosphides, chalcogenides) for the HER, both experimentally and theoretically (i.e., density functional theory (DFT) simulations and machine learning). Additionally, the associated mechanism, fundamental, and current interrogations (i.e., electronic effect, phase, strain, phase engineering, and interaction support) are highlighted related to porous bimetallic electrocatalysts for the HER. Eventually, a brief synopsis of the relevant milestones of current challenges and revitalizing perspectives to direct future research is presented aimed at developing effective porous binary metal-based electrocatalysts for large-scale HER applications.

1. Introduction

The global energy demand has increased substantially in the last decades and is expected to continue unabated, which exhausts non-renewable fossil fuels and subsequently emits hazardous greenhouse gases that instigate critical environmental issues [1,2]. To address the energy crisis and reduce carbon emissions, several promising solutions have emerged, including gas conversion reactions [3], clean energy production (i.e., fuel cells [4], batteries [5,6], solar cells [7]), and biofuels [8]. Hydrogen (H_2) is one of the most promising environmentally benign and efficient energy carriers or fuels due to its earth-abundant resources, low-cost, emission-free combustion, and impressive energy per mass relative to other traditional fuels [9,10]. Consequently, the demand for H_2 has increased, and it is logical to find the need for H_2 fuel, which has increased by almost 3-folds in the last three decades [11]. There are various scalable methods for the production of H_2, such as coal gasification and steam reforming, but they are highly energy demanded (i.e., temperature of 700–1100 °C and pressure of 3–25 bar) and consume non-renewable fuels along with gas emissions (i.e., CO_2 and CO) [12]. Unlike these methods, green H_2 production through HER only consumes water (H_2O ($2H^+_{(aq)} + 2e^- \rightarrow H_{2(g)}$)) and is conducted under ambient conditions (i.e., room temperature, low-voltage, and atmospheric pressure), which meet the sustainability values [13,14]. Notably, the excruciating cost of the HER (i.e., 3.8–8.8 €/kg H_2) relative to gasification/reforming (0.8–1.6 €/kg H_2) is as it mainly relies on noble-metal-based electrocatalysts [15–17]. Thus, reducing the cost is the main obstacle to scaling up HER (i.e., 4 % nowadays) to meet the increased demand for green H_2 fuel. The enthusiastic efforts center around the alloying of earth-rare and expensive Pt-group metals [18,19] and substitution with earth-abundant and inexpensive metals (i.e., W, Cu, Ni) [20,21] and supports (i.e., metal-organic frameworks (MOFs)-derived carbon, metal-oxide, carbon, metal-hydroxide) [22,23]. Nevertheless, the most efficient option is the utilization of alternatives to Pt-group electrocatalysts, like transition metals [24,25] and/or their nitride, sulfide, phosphide, and oxide forms [26], in addition to other catalysts, like carbon nitrides [27,28], MOFs [29] and MXenes [30].

* Corresponding author.
E-mail address: kamel.eid@qu.edu.qa (K. Eid).

https://doi.org/10.1016/j.ccr.2024.216238
Received 17 November 2023; Received in revised form 14 August 2024; Accepted 17 September 2024
Available online 11 October 2024
0010-8545/© 2024 Elsevier B.V. All rights are reserved, including those for text and data mining, AI training, and similar technologies.

Porous binary metal-based electrocatalysts possess several advantages, like porosity (i.e., huge surface area, accessible active sites, and enhanced utilization of buried atoms), which induces quick adsorption/mobility of reactants and promotes electrolyte-electrode interaction [31,32]. In addition to the electronic effect (i.e., synergic/strain, rich valence state, redox, and tunable surface properties) and low cost, which can enhance polarity and facilitate dissociation of H_2O, optimize hydrogen binding energy, and reduction of the activation energies for H_2-desorption/discharge step during HER at low overpotential [33] are some of the salient features. This is besides the ease of preparation using various methods (i.e., hydrothermal, template-based, and galvanic replacement, etc.) and the effortlessness of anchoring onto the current collector, which enhances their durability during HER electrocatalysis. Despite the noticed efforts in the fabrication of porous binary metals for HER electrocatalysis, there are plentiful scientific issues that need to be addressed, namely scalable synthesis, practical requirements, electronic effect, tailoring phase, and phase engineering, among others. The existing excellent reviews encompass MOF-based [34], transition metal phosphides [35], porous transition metals with superhydrophobic surfaces [36], and non-noble metal-based electrocatalysts for HER [37]. Notably, Guanjie et al. offered an overview that summarized the recent advances in the fabrication methods (i.e., wet chemistry, annealing, electrochemistry) of ultra-loading Pt-based electrocatalysts and their interaction with transition metals and their derivatives for HER [38].

Notably, in the last decade, there have been devoted efforts and attention to designing porous binary metal-based electrocatalysts with ultra-low Pt content for the HER, as reflected in the number of publications and their citations, including 232 articles cited 10,578 times (i.e., 45.59 citation/item) (Fig. 1a). Unlike existing ones, this comprehensive review unveils the engineering of porous noble binary-metal-based electrocatalysts, porous transition binary-metal electrocatalysts (i.e., carbides/oxides, phosphides, chalcogenides) for the HER from the viewpoint of experimental (i.e., synthesis strategies and electrochemical tests) and theoretical insights (i.e., density functional theory (DFT) simulations and machine learning) (Fig. 1b). In addition to the relevant mechanism, fundamentals, educational pathways, and deep analysis of the current queries (i.e., electronic effect, phase, strain, phase engineering, and interaction support) point to the porous bimetallic electrocatalysts for the HER. The review is concluded with a discussion of the current drawbacks and future outlook on developing porous binary metal-based electrocatalysts feasible for low-cost HER electrocatalysis.

2. Fundamentals of hydrogen evolution reaction (HER)

2.1. HER fundamentals

The fundamentals of HER, including mechanism, pathways, and effect of parameters (i.e., catalyst and electrolyte), are essential for advancing research in this area and improving the efficiency of electrolysis processes. The electrochemical overall water splitting for producing high-purity H_2 and O_2 in a neutral medium, as expressed in Eq. (1).

$$\text{Overall reaction}: 2H_2O_{(l)} \rightarrow 2H_{2(g)} + O_{2(g)}\ E^0 = 1.23\ \text{V vs.SHE} \quad (1)$$

Efforts are geared up to minimize the energy loss tend toward the utilization of highly acidic (pH = 0), with extremely high H_2 production efficiency attributable to the abundantly available protons (H^+) for rapid desorption of H_{ads} and H_2 formation, or highly alkaline electrolytes (pH = 14) with relatively poor H_2 production because of scanty H^+ supplied at high pH to the cathode during H_2O electrolysis, as expressed in Eqs. (2)–(5). This necessitates the utilization of highly active and durable electrocatalysts for optimal functioning of water splitting for high-purity H_2 production [39].

In acid solution:

$$2H_2O_{(l)} \rightarrow 4H^+_{(aq)} + O_{2(g)} + 4e^- \ (\text{Anode}, E^0 = 1.23\ \text{V vs.SHE}) \quad (2)$$

$$4H^+_{(aq)} + 4e^- \rightarrow 2H_{2(g)} \ (\text{Cathode}, E^0 = 0.00\ \text{V vs.SHE}) \quad (3)$$

In alkaline solution:

$$4OH^-(aq) \rightarrow 2H_2O_{(l)} + O_{2(g)} + 4e^- \ (\text{Anode}, E^0 = 0.40\ \text{V vs.SHE}) \quad (4)$$

$$4H_2O_{(l)} + 4e^- \rightarrow 4OH^-_{(aq)} + 2H_{2(g)} \ (\text{Cathode}, E^0 = 0.83\ \text{V vs.SHE}) \quad (5)$$

2.2. HER mechanisms

The production of H_2 via electrochemical water splitting involves the cleavage of the H-O-H bond, followed by chemisorption of proton (H_{ads}) and subsequent desorption of H_{ads} with recombination to form H_2 molecule. Thus, the HER mechanism is studied following three distinct steps, which are a function of the Tafel slopes (β) namely (i) Volmer, (ii) Tafel, and (iii) Heyrovsky [40,41]. It is well established that HER involves two key steps in acid and alkaline media, which are the electrochemical adsorption process (known as the Volmer step) and the

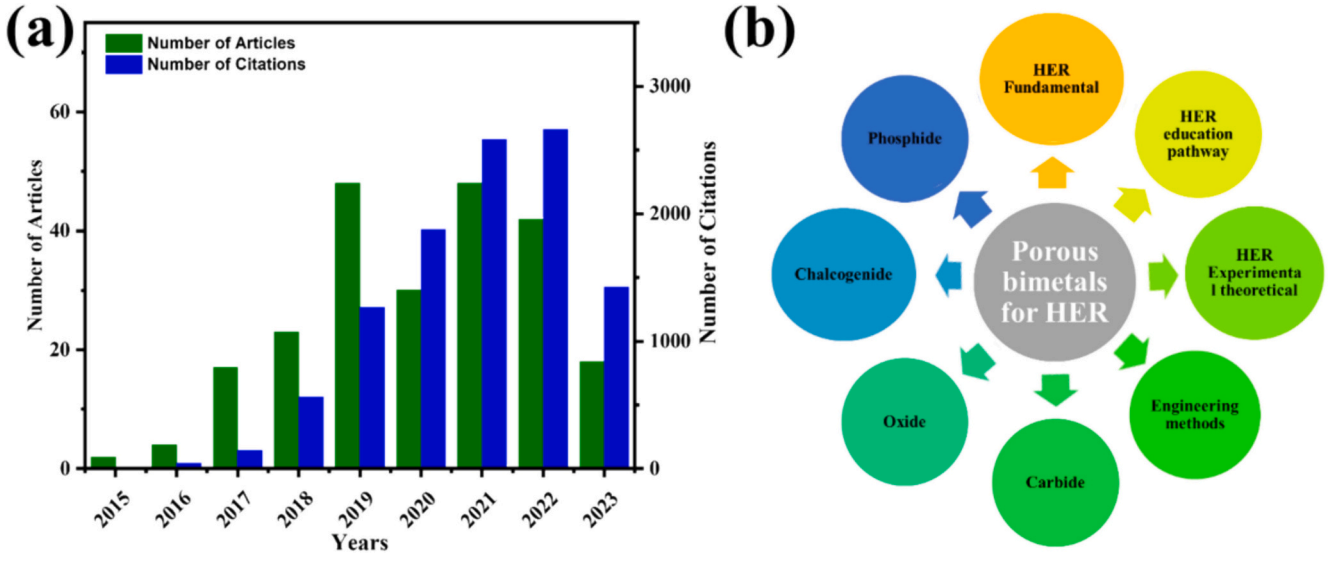

Fig. 1. (a) Number of articles vs. citations obtained from the Web of Science with keywords "porous binary metal-based electrocatalysts for HER" and (b) focus of this review.

desorption process (known as the Heyrosvsky step for electrochemical, or Tafel step for chemical). In summary, the generally accepted mechanisms consist of the following steps:

The first step is the:

1) Volmer step (electrochemical hydrogen adsorption)

This is the cleavage of the H-O-H bond and adsorption of H_{ads} on the active sites of the electrocatalysts, which is generally the slowest step and thus the rate-determining step (RDS).

$$M_{(s)} + H^{+}_{(aq)} + e^{-} \rightarrow M - H^{*} \text{ (acid solution)} \quad (6)$$

$$M_{(s)} + H_2O_{(aq)} + e^{-} \rightarrow M - H^{*} + OH^{-} \text{ (alkaline solution)} \quad (7)$$

Volmer step is followed by the

2) Heyrovsky step (electrochemical desorption of hydrogen):

This process encompasses continuous cleavage of H_2O and desorption of H_{ads} to yield H_2 (Eqs. (8, 9).

$$M - H^{*} + H^{+}_{(aq)} + e^{-} \rightarrow M + H_2 \quad \text{(acid solution)} \quad (8)$$

$$M - H^{*} + H_2O_{(aq)} + e^{-} \rightarrow M + OH^{-} + H_2 \text{ (alkaline solution)} \quad (9)$$

or the

3) Tafel step (chemical desorption of hydrogen).

$$M - H^{*} + M - H^{*} \rightarrow 2\,M + H_2 \quad \text{(acid or alkaline solution)} \quad (10)$$

Where H* represents a chemically adsorbed hydrogen atom on the active site of an electrode surface (M).

Notably, in the alkaline solution, H_2O serves as the source of a proton, giving rise to the OH^{-} as the conjugate-base product after electron transfer. In practice, the electrocatalytic activity of HER in acid is two or three orders of magnitude greater than in the alkaline medium. One of the reasons for this discrepancy is associated with the 'extra energy' of dissociating H_2O to generate the required proton (H^{+}) for the Volmer (Eq. 6,7) and Heyrovsky (Eq. 8, 9) steps to occur. In both acidic and alkaline conditions, the Tafel step (i.e., no charge-transfer is involved) remains the same.

The step that will dominate the HER activity is strongly dependent on the inherent electrochemical and electronic properties of the electrode surface (usually apprised by the electrocatalyst deployed to modify the electrode surface). Tafel slope (β = mV/dec) is an important distinguishing parameter that allows one to establish which of the steps (Volmer, Heyrovsky, or Tafel) is the possible rate-determining step (RDS), hence the underlying reaction mechanism. Tafel slope is obtained from Tafel (Eqn 10) and the conventional Tafel plot from the linear sweep voltammogram (i.e., overpotential (η / mV) vs. log current density (j / mA cm^{-2}).

Tafel equation is used in electrochemistry to describe the relationship between the rate of an electrochemical reaction and the overpotential (η) and is particularly important for understanding the kinetics of reactions like the HER. The term Tafel slope (β) is derived from the Tafel Eq. (11).

$$\eta = 2.3RT/\alpha nF \log (i/i_o) \quad (11)$$

where η, R, T, α, F, and n are the overpotential, universal gas constant, absolute temperature, electron transfer coefficient, Faraday's constant, and number of electrons. Meanwhile, (i) is current density, and (i_o) is exchange current density when there is no net current flow (equilibrium state). The Tafel slope value may be higher than the theoretically stated value due to the strong adsorption of H^{+} on the monolayer coverage of the electrocatalysts. Also, understanding the Tafel slope is crucial for designing and optimizing the electrolyzer, and the β is a key parameter in electrochemical kinetics and HER mechanism.

Theoretically speaking, the values of the Tafel slope (β) for the various steps are given as:

$$\text{Volmer step}: \quad \beta = 2.3RT/(\alpha \approx 0.5)F = 118.2 \text{ mV dec}^{-1} \quad (12)$$

$$\text{Heyrovsky step}: \quad \beta = 2.3RT/(1+\alpha)F = 39.4 \text{ mV dec}^{-1} \quad (13)$$

$$\text{Tafel step}: \quad \beta = 2.3RT/2F = 29.6 \text{ mV dec}^{-1} \quad (14)$$

In other words, the mechanism of the HER will most likely follow the Volmer-Heyrovsky or Volmer-Tafel pathways (Eqn 11, 12, 13). For example, if the HER on the surface of the electrocatalyst-modified electrode in an acidic solution is about 30 mV dec^{-1}, it means that the reaction proceeds via the Volmer–Tafel process and the RDS is the Tafel step (Eqn 13). Experimentally, the β values may vary (mostly higher than theoretical prediction) depending on the electrode surface/electrocatalyst employed in the HER. It should be noted that the Tafel slope is dependent on the coverage of the H* on the electrode surface. Thus, care ought to be taken to avoid an oversimplified interpretation of the Tafel slope [42,43]. Although the Tafel slope can indicate which of these steps is the RDS, the Tafel slope can be influenced by various factors like catalysts (i.e., shape, composition, and surface properties), electrolyte (i.e., pH, type, and additives), and the presence of other reactions like the hydrogen oxidation reaction (HOR). Therefore, for accurate comparisons among various electrocatalysts, it is crucial to have strict controls under the same conditions.

2.3. HER electrolytes

There are various electrolytes for the HER, including acidic (i.e., H_2SO_4, $HClO_4$, and HCL), alkaline (i.e., KOH, NaOH), and neutral (i.e., phosphate buffers, saline solutions) [44], besides ionic liquids (i.e., 1-ethyl-3-methylimidazolium tetrafluoroborate ([EMIM][BF4]), 1-butyl-3-methylimidazolium hexafluorophosphate ([BMIM][PF6]) [45,46], organic electrolytes (i.e., Water-in-Salt electrolytes (WiSEs) and quaternary ammonium salts) [47,48], solid polymer electrolytes (i.e., perfluorosulfonic acid polymers like Nafion and sulfonated polystyrene membranes) [49,50]. The acidic electrolytes have high ionic conductivity, enriched with protons, and show quick HER kinetics. However, they are corrosive and usually more favorable for Pt-group catalysts. The alkaline electrolytes are less corrosive and more feasible for Pt-free electrocatalysts, but they have low ionic conductivity with lower protons and subsequent sluggish kinetics. The neutral electrolytes are non-corrosive, safer to handle, and compatible with various materials, but they require a complex system and have very low ionic conductivity and slower HER kinetics. The ionic liquids has low vapor pressure, high electrical conductivity, wide operation potential window, and electrochemical stability, making them suitable for practical electrolyzers, and some of them can act as both electrolytes and catalysts in HER [45,46]. However ionic liquids are expensive, and it could be challenging to handle them including their scale up production. Organic electrolytes can enhance durability, allow for higher voltage operations, and tailor the adsorption energies on metal cathodes, but they are mostly deployed as supporting electrolytes and are difficult to scale up [47,48]. Solid polymer electrolytes can enable compact cell designs with impressive mechanical stability, but they posses low proton conductivity and usually need humidification to operate efficiently [49,50]. Notably, perfluorosulfonic acid polymers (e.g., Nafion) can allow selective conduction of protons while separating the produced gases and electrically insulating the electrodes and sulfonated polystyrene membranes; they can function as both the gas separator and the electrolyte in proton exchange membrane (PEM) electrolysis. Notably, the acidic and alkaline electrolytes are the most common in HER, and few others like ionic liquids and organic electrolytes are rarely reported. Also, most of the catalysts work either in acidic or alkaline or neutral electrolytes, and few

cathodes are able to work over different pH values. Therefore, more efforts ought to be dedicated to rationally utilize ionic liquids, organic electrolytes, and solid polymer electrolytes, and their HER performance should be optimized on porous binary metal-based cathodes.

2.4. HER working electrodes and their fabrication

Usually, porous binary metal nanostructures are formed in the form of powders, which are used to form the catalysts' ink. This includes initially weighting catalyst powder (2–4 mg) and dispersing it in a suitable solvent (1–2 mL) (i.e., water, ethanol, toluene, and isopropanol) and a binder (i.e., Nafion®, Aquivion®, and PTFE Fumion®) followed by sonication till the solution is homogenized. Nafion is the most common binder used to bind the catalyst ink to the working electrode to prevent it from peeling, besides reducing the diffusion resistance of H_2 and an ohmic (IR) drop along with promoting electrolyte-electrode interaction; the concentration of Nafion is low (50-100 μL/ml) relative the catalyst ink concentration [51]. The capping agent of the porous binary metal catalysts is mainly determined by the type of solvents. For example, catalysts prepared using non-ionic copolymers, i.e., PVP, F127, and Brig) [52–55] or uncapped are highly soluble in water, while those prepared using a hydrothermal method with Triton-X100 and oleylamine surfactant are soluble in toluene.

The catalyst ink could be loaded on working electrodes, like glassy carbon, carbon fleece sheet, carbon cloth sheet, and meta-hydroxide sheets) [56], in various ways, such as drop casting, impregnation, spray coating, and electrochemical deposition [57]. The glassy carbon is the most commonly used working electrode, and drop casting is the most common method of depositing catalysts' ink. However, carbon fleece and carbon cloth sheets, with their outstanding electrical conductivity, high surface area, porosity, and low cost, ought to be used more as they can meet sustainable and large-scale applications. After the deposition of catalyst ink on the working electrode, it should be dried in an oven under a vacuum at 80 °C, to allow polymerization of Nafion with the catalyst ink, and light is not preferred because it can destroy Nafion. Notably, non-thermally stable catalysts should be dried at low temperatures, preferably at 25 °C.

The current trend is to fabricate self-standing porous binary metal-based cathodes for HER and even other electrocatalytic applications to avoid detachment and aggregation of the catalysts. This entails the substrate support fabrication, like metal foam/sheet (i.e., Ni, Co, Ti, Pt) [58,59], carbon substrates (i.e., carbon cloth, carbon fiber paper, and carbon fleece) [60,61] and self-fabricated electrocatalysts [62], like foams, sponge, and aerogel (i.e., crosslinking of CNTS, MOF, and graphene with metals) [85]. The self-standing porous metal cathodes are usually prepared via electrospinning, film casting, hydrothermal method, and 3D printing [62]. Meanwhile, substrate-supported porous metals are commonly fabricated via electrochemical deposition [63], chemical vapor deposition [64,65], and hydrothermal deposition [66]. Among these, the free-standing porous metal-based cathodes possess many advantages over the powder ones, like superior electrical conductivity, stability, binder-free, and feasibility for practical applications.

Notably, the effect of binder type and content on the HER performance of porous binary metal cathodes has not been studied yet. For example, Marilena et al. studied the effect of Nafion concentration (i.e., 0–80 wt%) on the electrocatalytic alkaline HER activity of commercial Pt/C catalysts and the activity changed significantly with Nafion, but the optimal amount of Nafion content was nearly (25 wt%) while increasing Nafion amount led to decreased HER activity [67]. Also, the majority of previous reports only focused on using glassy carbon electrodes as the working electrode, so other electrodes should be studied and optimized.

2.5. HER measurements and calculations

The HER measurements are demonstrated by the various electrochemical techniques, including (i) cyclic voltammetry (CV) for the determination of electrochemical active surface area (ECSA); (ii) linear sweep voltammetry (LSV) for extracting crucial electrochemical HER data, (iii) chronoamperometry (CA) and chronopotentiometry (CP) for HER long-term durability; and (iv) electrochemical impedance spectroscopy (EIS) to probe the electrode-electrolyte interfacial interaction, using appropriate Voigt electrical equivalent circuit (EEC) to extract charge-transfer resistance (R_{ct}) and solution resistance (R_s). These techniques are employed to obtain and generate data relating to parameters of indicator for HER activity, such as overpotential (η), current density (j), Tafel slope (β), exchange current density (j_o), turn-over frequency (TOF), and H_2 production rate with their respective formula:

ECSA is believed to reveal a real surface area of the electrocatalyst exposed to the electrolyte and determined by several methods (i.e., hydrogen under deposition potential (H-UDP), carbon monoxide (CO) stripping, metal-oxides (M-O) reduction, and double-layer capacitance (C_{dl})). The H-UDP, CO stripping, and M-O reduction methods are commonly used for noble-metal-based electrocatalysts following Eq. (14) [68,69], while the C_{dl} method is employed for transition metal-based and/or carbon-based electrocatalysts with non-faradaic or capacitive behavior (Eq. 15) [70].

$$\text{For noble} - \text{metal} - \text{based electrocatalysts} : \text{ECSA}\left(\text{m}^2/\text{g}\right) = Q/s \text{ x } m \tag{15}$$

where integrated coulombic charge (Q) for H-UPD, CO peak, and M-O reduction peak, coulombic constant (s = 420 μC/cm^2) for monolayer noble-metal-based electrocatalysts and mass (m) loading of the electrocatalysts.

$$\text{For transition} - \text{metal} - /\text{carbon} - \text{based electrocatalysts} : \text{ECSA}\left(\text{cm}^2\right) = C_{dl}/C_s \tag{16}$$

where double-layer capacitance (C_{dl}) is the slope of the plot of (j_a - j_c)/2 against scan rates, specific capacitance (C_s) of a flat surface with 1 cm^2 (0.015–0.110 mF/cm^2 in H_2SO_4) and (0.022–0.130 mF/cm^2 in NaOH and KOH solutions).

Overpotential (η) is the most important parameter for HER activity, which is extracted from the LSV at defined current density (10 mA/cm^2, i.e., η_{10}) as the most acceptable benchmark (Eq. (17)).

$$\eta\ (\text{V}) = E - E^{\text{o}} \tag{17}$$

where measuring electrode potential (E) at specified current density, standard reduction potential (E^{o}). The lower value η of an electrocatalyst results in higher HER activity.

Current density (j) is the ratio of the measured current (i) to the geometric surface area of the working electrode (A) (Eq.18).

$$j\left(\text{mA}/\text{cm}^2\right) = i/A \tag{18}$$

Mass activity (MA) is the ratio of measured current (i_{HER}) to the mass (m) loading of the electrocatalyst (Eq. (19)).

$$\text{MA}\ (\text{A}/\text{g}) = i_{HER}/m \tag{19}$$

Specific activity (SA) is the ratio of the MA to the ECSA or the true surface area of the electrocatalyst (Eq. (20)).

$$\text{SA}\left(\text{mA}/\text{cm}^2\right) = \text{MA}/\text{ECSA} \tag{20}$$

Tafel analysis offers insight into the inherent HER kinetics of the electrocatalyst under investigation, following the conventional Butler-Volmer equation for both anode and cathode, which is translated at high η to Tafel equation for only one electrode, i.e., cathode (Eq. 21) or anode.

$$\text{Log}\, j = \text{Log}\, j_{\text{o}} + (-\alpha_{\text{c}} nF/2.303RT)\eta \tag{21}$$

Thus, a plot of ln j against η gives a straight line, where the slope

($-\alpha_c nF/2.303RT$) corresponds to the inverse of the β and the j_o (i.e., current at equilibrium potential) extrapolated the intercept ($\ln j_o$).

Turn-over frequency (TOF) is a desired kinetic parameter that measures the prompt efficiency of electrocatalysts for HER, which is calculated using Eq. (22).

$$\text{TOF}\ (s^{-1}) = j \times N_A / n \times F \times \Gamma \quad (22)$$

Avogadro number (N_A), number of electrons ($n = 2$) to evolve a molecule of product (H_2, i.e., $n = 2$), Faraday constant (96,485 C/mol), and surface concentration of active sites (Γ) obtained from the slope of a linear plot of j vs. scan rates. Also, Γ could be obtained from normalizing QN_A to nFA, where Q is the voltammetry charge and A is the the surface area of the electrode.

H_2 production rate is the amount of H_2 produced during water electrolysis and is calculated from the ratio of current ($j \times A$) to $2F$ (Eq. (23)).

$$H_2 \text{ production rate } (\mu\text{mol/h}) = (j \times A)/2F \quad (23)$$

3. Formation mechanism of porous binary metals

Continuous growth, crystallite coalescence, seed-mediated growth, and galvanic replacement are the main mechanisms for the formation of porous binary metal nanostructures. The continuous growth comprises the initial reduction of metal precursors with higher reduction potentials that in situ act as seeds for supporting growth of other metal atoms, followed by the continuous growth to form binary metal-based nanocrystals [71]. The usage of facet-specific capping agents (i.e., I, F, Cl, Br) can drive the formation of binary metal-based nanocrystals with high-index or controlled facets, whereas using oxidants (i.e., O_2 or Fe(III) and NH_4OH/H_2O_2) under air can promote the oxidative etching to form porous, concave and branched nanostructures [72,73]. The crystallite's coalescence, "direct attachment growth" occurs using a strong reducing agents lead to explosive nucleation to form multiple crystallites with a massive surface free energy, which tends to coalesce along a specific crystallographic orientation [74,75], resulting in quick diffusion of metal atoms across the interface via Brownian motion to produce porous binary metal-based nanocrystals composed of multiple crystallites [71]. Seed-mediated growth involves the initial formation of metal nanoparticles as seeds to provide abundant sites for supporting the growth of other metals according to the pathways. This occurs through either Frank-van der Merwe (layered growth) and Stranski-Krastanov "layer-plus-island growth" in case of high synergism among seeds and two metals or Volmer-Weber "island growth" under rapid reduction rate or intermediate mode to yield core-shell nanocrystals [71]. These are driven by surfactants, reducing power, temperature, and additives [76]. The galvanic replacement entails the formation of metal seeds, and then it is replaced by other metal salts with a higher redox potential via electron transfer from the seeds to other metals in the presence or absence of a reducing agent [71,77]. The dissolution and deposition occurs on the high and low surface-energy facets of the seeds, respectively, and the final shape depends on the seed shapes, but it could be directed to other shapes in the presence of surfactant facet-specific agents [71]. Another pathway for galvanic replacement is the formation of metal alloy and then dealloying using an acidic or alkaline solution [72,73]. These mechanisms could be coupled using various preparation methods.

4. Fabrication methods of porous binary-metal-based electrocatalysts

The sol-gel, hydrothermal, microwave-assisted synthesis, electrochemical methods, and template-based), solid-phase (i.e., high-temperature annealing, solid-phase combustion method, and MOF-derived), and vapor-phase (i.e., spray pyrolysis, chemical vapor deposition, atomic layer deposition, and plasma) are the main preparative methods for the controlled synthesis of porous binary metal nanostructures for HER.

4.1. Solution-phase methods

The solution-phase synthesis possesses many advantages, like simplicity, relatively high mass yield, diverse reagents, normal laboratory equipment, and a variety of produced nanostructures. This approach comprises the synthesis in an aqueous solution of binary metal precursors in the presence of structure-directing agents (i.e., surfactants) and reducing agents deploying assorted methods (i.e., sol-gel, hydrothermal, solvothermal, microwave-assisted synthesis, template-based, galvanic replacement, chemical reduction, precipitation, solution combustion, and electrochemical methods) [78–80]. The metal concentrations, redox potentials of metals, type/concentration of surfactants, and power of reducing agents are the main parameters for determining the morphology (i.e., tubes, rods, foam, honeycomb, and dendrites) of porous binary metal nanostructures [52,81]. The solution-phase methods have been highlighted in reviews but more from the view of methodology rather than mechanism [82]. In this section, the main solution-phase methods and their mechanism are discussed to understand their structural HER activity refashions.

4.2. Hydrothermal and solvothermal method

The hydrothermal method entails the direct mixing of metal precursors (i.e., nitrate, chloride, acetate, and hydroxide) in the presence of an aqueous solution (i.e., water with or without organic solvents), pH modulator (i.e., KOH and KI) as a catalyst, and surfactants (i.e. PVP and Pluronic F127) as shape modulator [83,84], followed by sealing and heating in an autoclave for 2–24 h. The high temperature and pressure generated in the sealed autoclave, metal concentration, solvents, and surfactants are the main factors for tailoring porous morphology and compositions of the products. This method is simple, efficient, and suitable for various metal salts and allows the synthesis of various metal alloys, metal oxides, nanocomposites, spinels, and perovskites with and without supports (i.e., carbon nanotubes, graphene, and graphene oxide) in different porous structures (i.e., tubes, cubes, and dendrites). The formation mechanisms comprise the initial nucleation followed by subsequent growth, while the adsorption of surfactants or interaction with the additives (i.e., ^-OH, I^- and Br^-) and sometimes in situ etching drive the formation of porous morphologies [85,86]. For instance, excavated octahedral mesoporous $PtCu_3$ nanostructures (120 nm) composed of ultrathin nanosheets (4.5 nm) (Fig. 2a) were prepared by the hydrothermal method using an aqueous solution of $CuCl_2$, H_2PtCl_6, KI, guanidine carbonate, PVP, and ethanolamine at 170 °C for 8 h [87]. This is driven by the oriented attachment process with the assistance of guanidine carbonate as a directing agent due to its ability to be hydrolyzed to release urea (guanidine carbonate $+2H_2O \rightarrow 2CO(NH_2)_2 + (NH_4)_2CO_3$) followed by decomposition to NH_3 and CO_2 ($CO(NH_2)_2 + H_2O \rightarrow 2NH_3 + CO_2$) at 100 °C which serves as in-situ bubble templates for generating pores. PtNi multicubes assembled of multiple nanocubes (5 nm) have been synthesized by the hydrothermal method at 180 °C for 12 h using curcumin as structure-directing agent (Fig. 2b–d) [54]. The formation mechanism is attributed to quick nucleation and consequent oriented attachment epitaxial growth with the aid of complexation of Pt/Ni precursors with oleylamine, curcumin, and oleic acid. The hydrothermal synthesis protocol was deployed to prepare various porous metals, like $ZnMn_2O_4$ microspheres [88], Pd—Cu alloy with hierarchical network [89], porous ternary PtPdCu alloys [90], and Ni_3S_2/NiS nanowires [91].

The solvothermal approach is essentially the same as the hydrothermal but uses non-aqueous solvents (i.e., ethanol, ethylene glycol, isopropanol, PEG, tertiary butanol, and dimethylformamide) while operating at higher temperatures [92,93]. The organic solvents may act as structure-directing agents and the formation process is faster. For

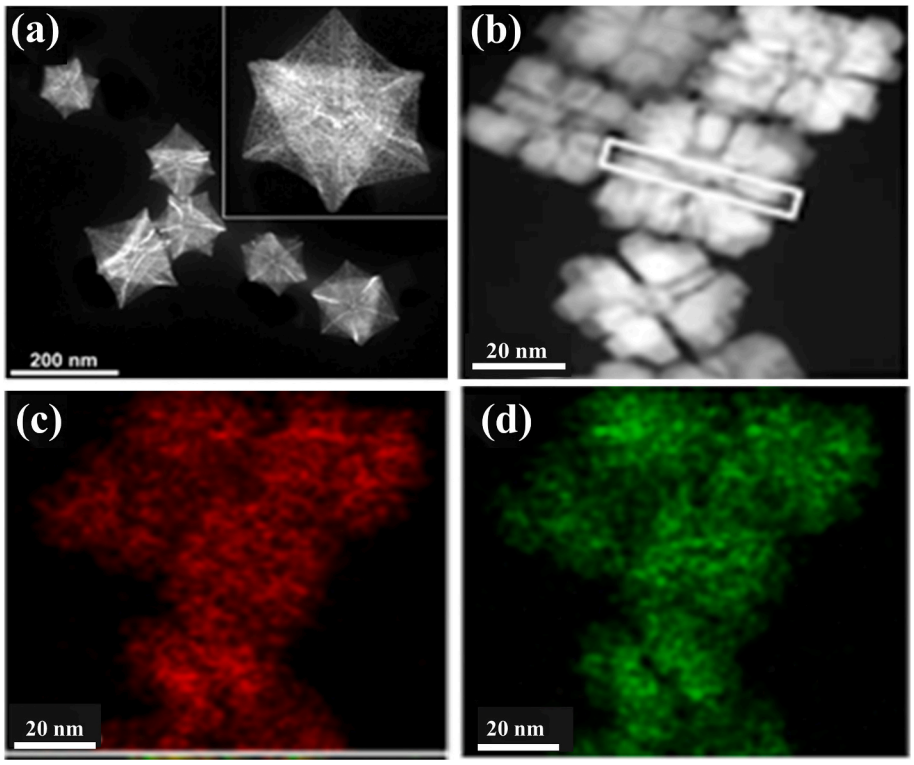

Fig. 2. (a) HAADF-STEM image of octahedral mesoporous $PtCu_3$. Reproduced with permission from Ref. [87] Copyright 2019 Wiley-VCH. (b) HAADF-STEM and elemental mapping of (c) Pt and (d) Ni. Adapted with permission from Ref. [54] Copyright 2020 American Chemical Society (ACS).

example, porous Co/Mn, Ni/Mn, and Co/Mn/Fe mixed-metal oxides were synthesized using the solvothermal method using methanol and diethylene glycol at 300 °C for 10 min (Fig. 3a) [94]. The slow heating led to sluggish nucleation and yielded nonhomogeneous nanoparticles due to aggregates, while homogenous quick heating accelerated nucleation to yield homogenous porous nanocrystal assemblies with narrow size distribution. This is due to the quick consumption of the metal ions in the precursor solution under homogenous heating. Therefore, understanding the mechanism drove the formation of various porous morphologies like MOF-199 [95], 3D porous V_2O_5 [96], porous Ni/ ZrO_2 sphere [97], Cu—Pt Nanocage [98], and porous network $NiCo_2S_4$ [99]. Porous PtAg neural-like network nanowires (PNWS) with lengths up to ~1.5 μm length and width of 20 nm enriched with pores (2–10 nm), and high Ag content (~34 at.%) were prepared via the solvothermal of Pt/Ag slats in a solution of DMF, ethylene glycol, and KOH at 170 °C [100], driven by the autocatalytic and oriented attachment growth mechanism. However, the underlying mechanisms of both hydrothermal and solvothermal methods are still ambiguous and the role of precursors ought to be underlined with in situ characterization tools like TEM during the synthesis process.

4.3. Microwave-assisted method

The microwave (MW)-assisted method involves MW irradiation of an aqueous solution of metal precursors in organic solvents (i.e., ethylene glycol, ethanol, dimethylformamide, oleylamine, and glycerol) and inorganic additives as co-catalysts (i.e., KI, KOH), which is simple, quick, effective and low-energy demanding [103–105]. The irradiation power, time, and reaction parameters (solvents and additives) are the main factors for tailoring the morphologies and compositions of porous binary metal-based nanostructures. For example, mesoporous $NiCo_2O_4$ microspheres composed of various randomly distributed interconnecting thin nanosheets (Figs. 3b, c) [101], were formed via the MW irradiation of an aqueous solution of $Ni(NO_3)_2$, $Co(NO_3)_2$ and urea at 100 °C at 300 W for 30 min. The mesoporous structure originated from the thermal decomposition of hydroxides and consequent recrystallization at 100 °C. The microwaves assisted the formation of various porous binary metal-based materials, such as Pt—Cu nanosheets and nanocones [106], 3D single-layered MoS_2 [107], NiAl-LDH hollow microspheres [108], and MnO_2-NW@ [109] at low temperature and in shorter reaction time relative to hydrothermal/solvothermal methods. However, the microwave protocol favors the formation of microstructure materials with less size and porosity controlled, which are not favored in HER.

4.4. Electrochemical method

Electrochemical deposition is fast, one-step, less energy-demanding (i.e., low temperature and volt), and low-cost approach for the formation of porous binary metal-based nanostructures in the form of thin films or coatings in diverse shapes and compositions (i.e., alloy, core-shell, and oxide) [110,111]. It entails the reduction/oxidation of metal ions in the electrolyte solution (i.e., acid, alkaline, and neutral) and their simultaneous deposition on the conductive substrates (i.e., carbon cloth and metals sheet) under applied potential [112]. The electrolyte type, applied potential, cell set-up, and time are the main factors for tailoring the shapes and compositions of porous metal nanostructures. This method allowed the formation of various porous binary metal nanostructures, like porous PdAu nanostructures [113], *Re*—Co [114], Pt–MoS_x [115], and Pt_{SA}-NiO/Ni 3D nanosheets [116] in different electrolytes (i.e., KCl, $Na_3C_6H_5O_7$ + $(NH_4)_2SO_4$, and NaOH). For example, mesoporous Fe—Pt smooth thin films, proved by the SEM (Figs. 3d–f), on different supports (i.e., Au, Cu, and Al) were prepared by the micelle-assisted electrodeposition in electrolyte, which entailed $FeCl_2{\cdot}4H_2O$, Na_2PtCl_6, and P-123 triblock copolymer at pH 2.1 at the applied potential (−1.1 V) for 600 s at 35 °C in three-electrode cell [102]. The film thickness was controlled depending on the deposition time, and P-123 acted as a template for porosity. Although the electrodeposition method yields materials that can be used as working electrodes for HER, it needs a lot of precaution and skills to tailor the morphology and composition.

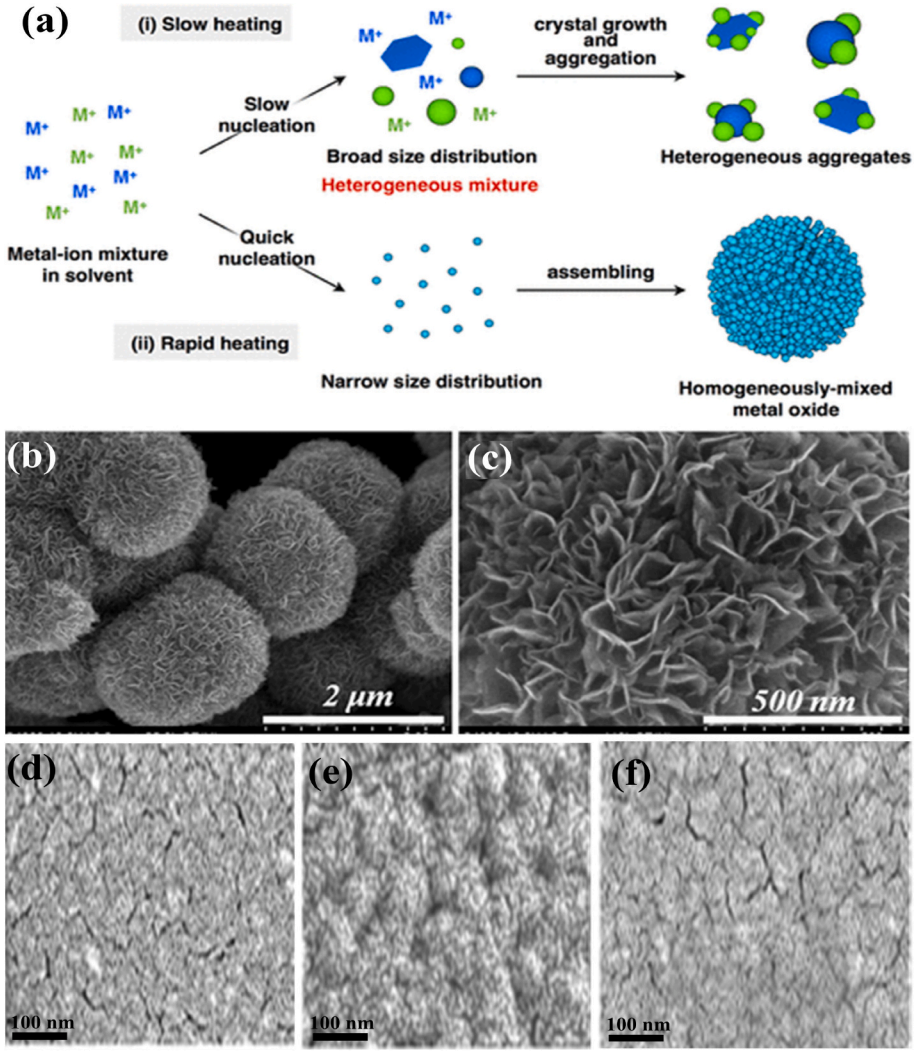

Fig. 3. (a) Formation mechanism of mixed metal oxides. Reproduced with permission from Ref. [94] Copyright 2017 ACS. (b-c) Fe-SEM of porous $NiCo_2O_4$ microspheres. Ref. [101]. SEM image of mesoporous Fe—Pt films electrodeposited on surfaces of (d) Au, (e) Al, and (f) Cu. Reproduced with permission from Ref. [102] Copyright 2017 Wiley-VCH.

4.5. Template-based method

Template-based methods comprise hard templates (i.e., colloidal crystals, mesoporous silica, zeolites, and alumina membranes, containing 3D interconnected mesopores) while the soft templates (i.e., liquid crystal, block copolymers, and surfactants) are the ideal options to fabricate well-ordered porous binary metal-based nanostructures. The morphology, porosity (i.e., pore size and volume), surface area, and other properties of the porous binary metal-based nanostructures follow the dynamic structure of the templates used.

4.5.1. Hard templates

The hard templates involve the infiltration of metal precursors via (i.e., in situ deposition, co-deposition, and self-assembly) into the hard templates silica (e.g., MCM-48, MCM-41, KIT-6, and SBA-15), anodic aluminum and latex crystals) followed by template removal using acidic/alkaline solutions (i.e., HF, NaOH etching, and heating), leaving behind a porous metal replica of the starting template [117,118]. The template properties (i.e., porosity, surface area, size, and shape), metal precursor concentration, and reaction parameters (i.e., heating and etching) are the main factors for tailoring the shape and properties of porous binary metal-based nanostructures. Hierarchical Au/Pt porous nanosphere [119] and 3D hexagonal mesoporous PtRu [120] were prepared using silica templates. PtCu nanotubes were prepared by reduction of H_2PtCl_6 and $CuCl_2$ with ascorbic acid in the presence of Te nanowire, followed by etching using NaOH (Fig. 4a) [121]. Nanotubes, with their short electron-path, enhanced the electrocatalytic activity. The same method was deployed to form 1D hierarchical mesoporous PtCu, but with the addition of F-127 as a soft template (Fig. 4b) [122]. Salt-like (i.e., KCl) was used as a hard template for the formation of NiFe/N-doped 3D porous carbon nanosheets [123]. However, the volume collapses during the reduction of metal precursors, leading to incomplete retention of the shape and porosity of the templates after the removal step. This issue could be circumvented by coupling hard templates with other methods, like electrodeposition or chemical reduction [124,125]. Notably, the utilization of hard templates for porous binary metals for HER ought to be sufficiently highlighted.

4.5.2. Soft template

Soft templates are categorized into lyotropic liquid crystals, micelle assembly, and degradable block copolymers, which vary in their ability to fabricate porous nanostructures.

- **Lyotropic Liquid Crystals (LLCs)**

LLCs are formed by the self-assembly of amphiphilic molecules (i.e.,

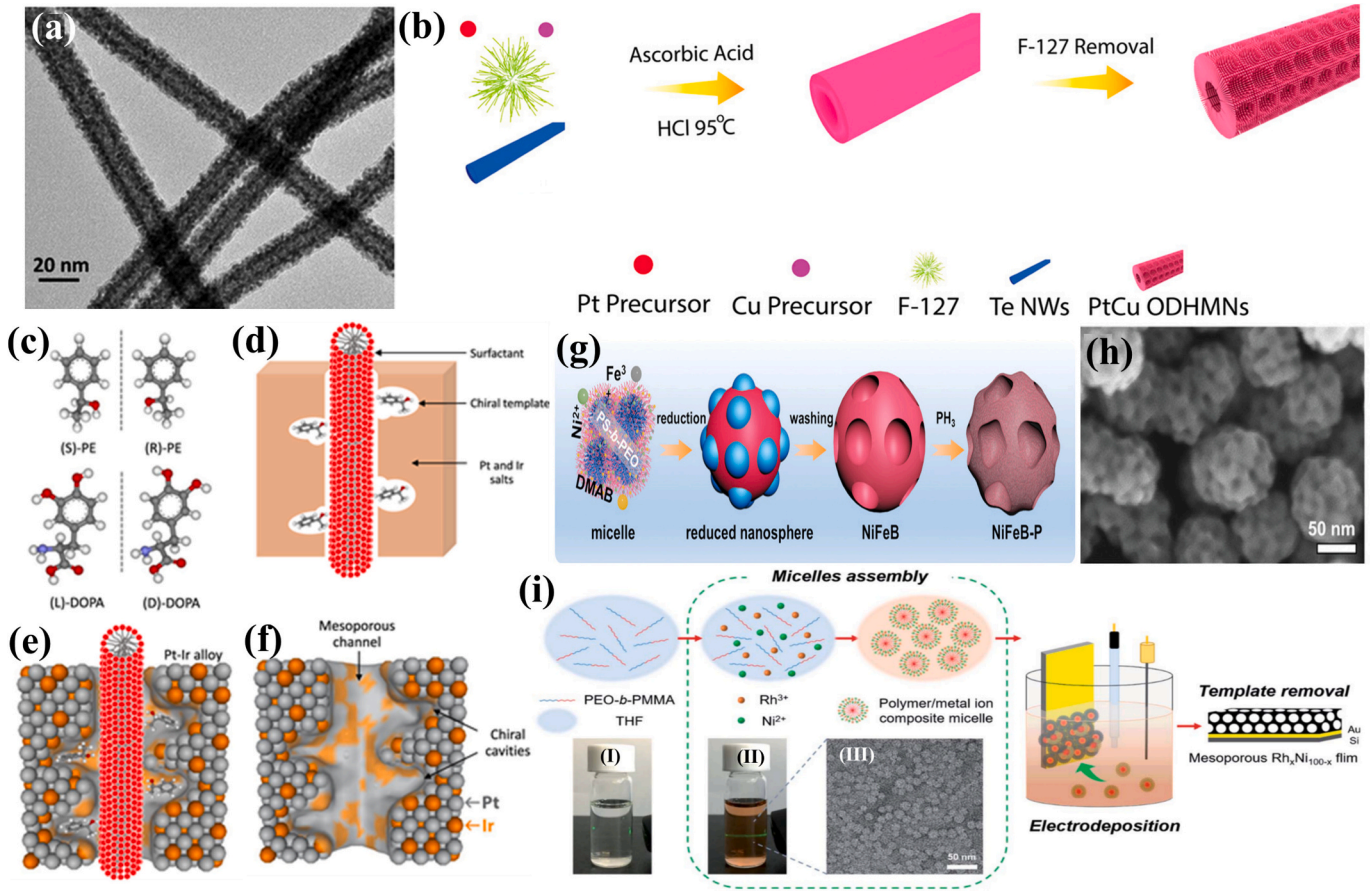

Fig. 4. (a) TEM image of PtCu nanotubes. Reproduced with permission from Ref. [121] Copyright 2016 Royal Society of Chemistry (RSC). (b) Soft template synthesis of 1D hierarchical mesoporous PtCu. Reproduced with permission from Ref. [122] Copyright 2016 ACS. Formation mechanism of mesoporous Pt—Ir using LLC template (c-f)Reproduced with permission from Ref. [128] Copyright 2021 Nature. (g) The preparation process of NiFeB-P MNs and its SEM (h). Reproduced with permission from Ref. [131] Copyright 2022 Wiley-VCH. (i) Preparation scheme of mesoporous RhNi and its optical images of the Tyndall phenomenon confirming the formation (I) $PEO_{(10500)}$-*b*-$PMMA_{(18000)}$ + THF, (II) $PEO_{(10500)}$-*b*-$PMMA_{(18000)}$ + THF + Na_3RhCl_6 + $NiCl_2$ + water and (III) TEM of micelles in the solution. Reproduced with permission from Ref. [132] Copyright 2021 RSC.

surfactants and block copolymers) at high concentrations (i.e., ≥ critical micelle concentration (CMC)) in a solvent (i.e., water). The LLCs were initially used for mesoporous Pt-based nanostructures like PtNi and PtRu [126,127] and then coupled with other methods (i.e., electrodeposition and microwave). Regarding this, mesoporous chiral Pt—Ir was obtained via co-electrodeposition of $[PtCl_6^{2-}]$/$[IrCl_6^{2-}]$ on Au-coated SiO_2 slide in the presence of LLC template (i.e., 3,4-dihydroxy-*L*-phenylalanine, and 3,4-dihydroxy-*D*-phenylalanine, (*R*)-phenylethanol, and (*S*)-phenylethanol) and non-ionic surfactant Brij® C10) (Figs. 4c, 5f) [128]. The unique molecular structure of LLCs (Fig. 4c) self-assembled to form columns of non-ionic surfactant decorated with chiral template (Fig. 4d) that induces growth of PtIr alloy around the LLCs by co-electrodeposition (Fig. 4e). Finally, the chiral-imprinted mesoporous Pt—Ir alloy are obtained after templates removal (Fig. 4f). Mesoporous NiCo alloys/rGO (MNi_xCo_{100-x}/rGO_5) have been synthesized using LLCs (i.e., Brij 58) as a template with $NiCl_2$/$CoCl_2$ and rGO as a support at (80 °C) through reduction using dimethylamine borane at 12 °C and finally LLC removal by ethanol [129]. MNi_xCo_{100-x}/rGO_5 had a high surface area (161 m^2/g) and high pore volume (0.17 cm^3/g), which have been significant merits for electrocatalytic HER activity. Notably, deploying a high concentration of LLCs (≥40 wt%), multiple reaction steps, improper mechanical/thermal stability, and limited formation of a mesoporous structure with a larger pore size (>4 nm) endure changes in the LLCs-based method [130]. This could be solved via evaporated organic solvents (i.e., ethanol and tetrahydrofuran) and using other templates (i.e., anodic alumina membranes) with LLCs as has been observed in the synthesis of mesoporous PtRu [126], driven by facilitating the filtration of diluted surfactants with LLCs templates. However, LLCs with high-cost and complication reaction steps limit their utilization in HER. P/B-codoped porous NiFe nanostructures (Fig. 4g,h) [131] and mesoporous RhNi (Fig. 4i) [132] with large pore size (10–15 nm) have been prepared using LLCs of (i.e., rPS_{5000}-*b*-PEO_{2200}).

- **Micelle Assembly**

Micelle assembly comprises the self-assembly of amphiphilic polymer with a hydrophobic tail and hydrophilic head to form micelle. It has a long history, as it was originally discovered as early as 1913 by McBain [133], and later it was combined with other methods, like electrodeposition and galvanic replacement [134], for tailoring the synthesis of mesoporous metal-based nanostructures. In this context, Pt/Pd films with controlled thickness were formed via micelle assembly combined with the electrodeposition method using Brij 58 surfactant with K_2PtCl_4 and Na_2PdCl_4 with P123 surfactant [135]. Afterwards, various porous binary metal-based nanostructures were prepared using a micelle assembly approach coupled with electrodeposition like Pt—Au using Brij 58 [136] and mesoporous Pt—Ru using Brij 58 [137], and 3D porous FeNi using Pluronic F127 [138]. Pluronic F127 micelle assembly was even used to form interweaved porous Pd—Ru nanosheets on Ni foam (PdRu NS-NF, Fig. 5a) with the assistance of a galvanic replacement reaction [139]. Ni foam has been deployed as a reducing agent and substrate in the electrolyte of HCl and KBr for 12 h, but the longer time

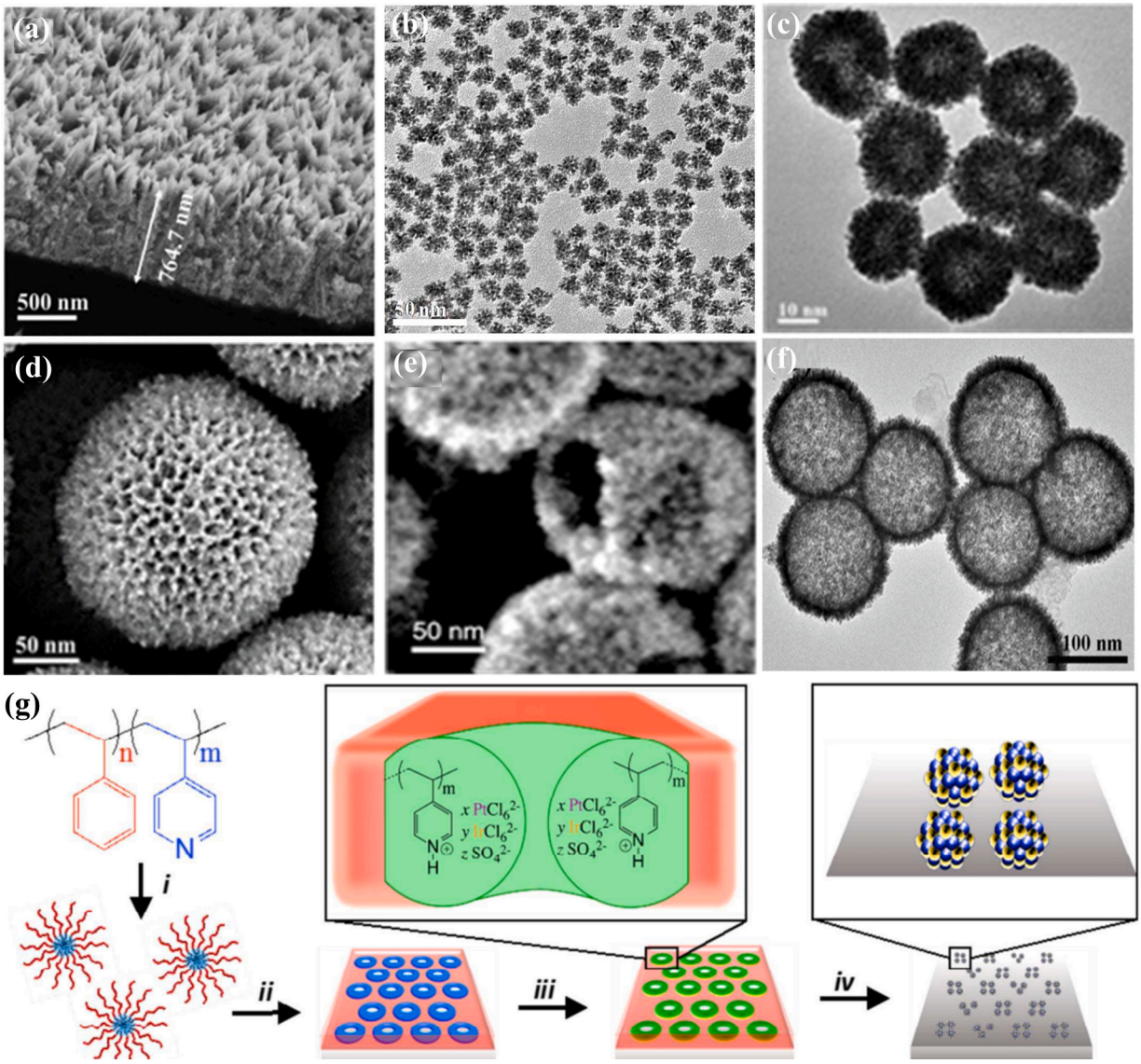

Fig. 5. TEM images of (a) interweaved Pd—Ru nanosheets. Reproduced with permission from Ref. [139] Copyright 2020 Elsevier. (b) TEM image of PtCo non-dendritic. Reproduced with permission from Ref. [144] Copyright 2016 Elsevier. (c) TEM image of PtPdRu nanocages. Reproduced with permission from Ref. [142] Copyright 2015 ACS. (d) TEM image of cage-bell Pt@mPt. Reproduced with permission from Ref. [159] Copyright 2018 ACS. (e) Au@ porous Pt yolk-shell, and (f) PtPd hollow nanospheres. Reproduced with permission from Ref. [55, 79] Copyright 2015,2016 Wiley-VCH. (g) Preparation scheme of PtIr bimetallic catalysts using thin polystyrene-*block*-poly(4-vinylpyridine) micelles. Reproduced with permission from Ref. [160] Copyright 2017 RSC.

and multiple reaction steps remain grand challenges. To circumvent these issues, we have used the concept of micelle assembly method to synthesize porous PtPd [79,80], PtCu [140], AuPt [55,141], PtPdRu [142,143], PtCo [144], PtNi [145] branched nanostructures with well-defined porosity (4–16 nm) and high surface area (38–179 m^2/g), using *co*-polymers (i.e., PVP, Pluronic F127) and ascorbic acid as a reducing agent (Fig. 5b–f) [145]. Furthermore, our group prepared PtAg nanochains (20 nm width) with interconnected pores (10 nm) and a high surface area (55.02 m^2/g) using pluronic P-123 based on direct nucleation and oriented attachment growth mechanism while deploying sonication at room temperature [146]. This approach is simple, green (i.e., no organic solvents), and quick (i.e., few minutes) without the need for heating or additional steps to etch non-ionic-copolymers, and the HER activity of such materials ought to be emphasized. Notably, micelle assembly was extensively used for coupling noble metals with transition metals without the underlying formation of Pt-free porous transition metals. Meanwhile, the low-mass production of micelle assembly method makes it unfeasible for large-scale HER applications.

- **Degradable block copolymers**

Unlike other templates, degradable block copolymers (i.e., polystyrene-*b*-poly(L-lactide), poly(lactic-*co*-glycolic acid), isoprene-*block*-styrene-*block*-ethylene oxide) entail two or more chemically different polymer chains covalently linked [147,148], which can self-assemble into porous nanostructures (i.e., 0D, 1D, 2D, and 3D) after removal of the template via hydrolytic treatment, ozonolysis, UV degradation, and reactive ion etching [149]. Polystyrene-polybutadiene and PS-polyisoprene were used for the first time to synthesize porous dense periodic arrays of holes (20 nm) and dots in a silicon nitride-coated silicon wafer [150] and then polystyrene-*block*-poly(4-vinylpyridine) was used to prepare porous Au metal nanoparticles in 2003 [151]. Branched structures are easily prepared using degradable copolymers like PtRuPd [152], sea-urchin-like PdAuCu [153], and nanodenderities AuPtAg using [154] were formed using hexadecylpyridinium chloride, polyethylene oxide, and *L*-proline, respectively. Degradable copolymers can be easily combined with other methods like electrodeposition to

form mesoporous AuCuNi [155], AuAg using chemical reduction, e.g., core-shell PtAu using [156], argon plasma reduction, e.g., core-shell PtAu [157], and galvanic replacement, as exemplified by AuAg using [158] using polystyrene-based copolymers.

Arrays of PtIr alloy nanoclusters (4–13 nm) with ordered intercluster spacing (~60 or ~100 nm) were synthesized via self-assembly of polystyrene-*block*-poly(4-vinylpyridine) with periodic pyridinium-rich domains followed by thermal annealing/reduction (Fig. 5g) [160]. The arrays were produced via initial self-assembly of PS-*b*-P4VP into spherical micelles in toluene, then spin coating onto electrode and followed by thin film reconstruction into an array of inverted-micelles by soaking in methanol. This offered abundant sites for accommodation of $PtCl_6^{2-}$/$IrCl_6^{2-}$ ions after eventual removal of polystyrene-*block*-poly(4-vinylpyridine) by thermal annealing under Ar. The high-cost of template-based method and the involvement of multiple reaction steps, and low mass production are great barriers for practical HER applications.

5. Porous transition binary transition metals

Porous materials comprising micropores, mesopores, and macropores, with pore sizes of ≤2, 2–50, and ≥ 50 nm, respectively, follow the classification according to the International Union of Pure and Applied Chemistry (IUPAC). According to the electronic structure, transition metals are defined as those elements that have valence electrons in two shells partially filled d orbitals or the capacity to produce cations with an incomplete d subshell based on IUPAC nomenclature. They occupy the middle portions of the long periods of periodic table elements from Groups 3–11 (i.e., Cu, Co, Mo, and Ni).

5.1. Transition with noble metal electrocatalysts for HER

Alloying with other metals not only reduces the loading of rare and expensive Pt but also modulates its d-band center with respect to the Fermi-level results, thus optimizing the binding energies of reactants and tolerating the intermediates during the HER. Thereby Pt–M (M = Pd, Rh, Ru) decorated nano-porous silicon flour (Nano-PSiF) enhances the HER activity in 0.5 M H_2SO_4, in the order Pt-Pd/PSiF> Pt-Rh/PSiF> Pt-Ru/PSiF> Pt/C > Pt/PSiF. This implies better performance using Pd with Pt. The Pt-Pd/PSiF had η_{10}/Tafel slope of −225 mV_{AgCl}/41.9 mV dec^{-1}, and it decreased to −213 mVAgCl/39.6 mV dec^{-1} via the deployment of rGO support with Pt-Pd/PSiF [161]. Besides, Pt-Pd-rGO core-shell showed η_{10}/Tafel slope of −10 mV/10 mV dec^{-1} [162]. Pd@PdPt NCs concave octahedral had a lower η_{10}/Tafel slope of −39 mV/ 38 mV dec^{-1} relative to its individual counterparts [163]. AuPt nanodendrites with a size of 35.3 nm and Au loading of 62.04 Wt% were synthesized by the ultrasonication-assisted wet-chemical reduction through ascorbic acid in presence of 4-amino-2,6-dihydroxypyrimidine (ADHP) as structure directing agent (Fig. 6a) had a η_{10}/Tafel slope (48 mV/34 mV dec^{-1}) comparable to Pt/C (38 mV/32 mV dec^{-1}) in 0.5 M H_2SO_4 (Fig. 6b) [164]. This is owing to the alloying effect, which modulates the d-band center of Pt, resulting in controlling the adsorption of reactants and tolerating the adsorption of intermediates besides porous dendritic morphology with accessible active sites and stability against aggregation. Thus, AuPt NDs reserve their stability with negligible decrease after 1000 cycles and durable current at 100 mV after 1.1 h (Fig. 6c). This implies the significant effect of branched structures for promoting the HER. However, Au metal is expensive and rare, and hence other metals with lower coats could be more favored. Pt decorated carbon cloth (CC)-supported $Co(OH)_2$ nanosheets array ($PtCo(OH)_2$/CC)

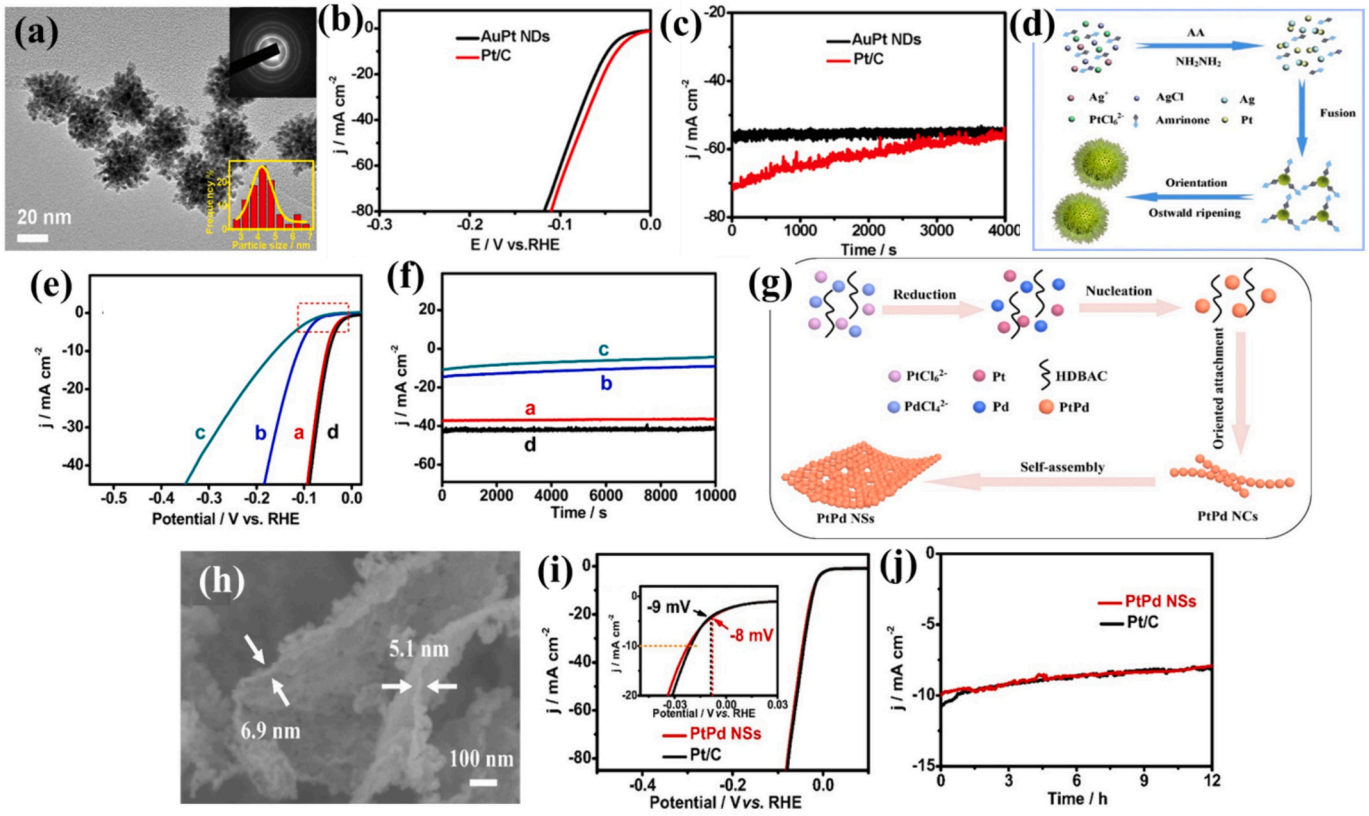

Fig. 6. (a) TEM image, (b) LSV curves at 1600 rpm, and (c) CA test @ η_{100} of AuPt NDs. Reproduced with permission from Ref. [164] Copyright 2017 Elsevier. (d) Preparation schematic of $Pt_{68}Ag_{32}$ nanodandelions and its LSV (e) and CA test @ η_{60} (f) compared with $Pt_{68}Ag_{32}$ nanodandelions (line a), $Pt_{75}Ag_{25}$ nanocrystals (line b), $Pt_{56}Ag_{44}$ nanocrystals (line c) and Pt/C (line d). Reproduced with permission from Ref. [167] Copyright 2018 Elsevier. (g) Schematic preparation method of PtPd (h) and its SEM image, (i) LSV curves, (j) CA test @ η_{22}, of PtPd nanocrystals. Reproduced with permission from Ref. [170] Copyright 2019 Elsevier.

formed by the electrodeposition showed a similar performance to Pt/C with a η_{10}/Tafel slope of −32 mV/ 70 mV dec^{-1}, which was significantly superior to Pt/CC and M-Co$(OH)_2$/CC (M = Ni, Fe, and Co) in 1 M KOH [165]. This is in addition to good activity in PBS electrolyte on Pt-Co$(OH)_2$/CC with a lower η_{10} of 10 mV than Pt/CC and than Co$(OH)_2$/CC thus indicating the feasibility of inexpensive and earth-abundant Co metal to enhance the HER performance of Pt.

The solid-core@porous branched shell of PtAg NCs prepared by the chemical reduction using ascorbic acid in the presence of diprophylline (DPP) showed a lower η_{10}/Tafel slope (149 mV/40 mV dec^{-1}) relative to Pt black but close to Pt/C (140 mV/31 mV dec^{-1}) in 0.5 M H_2SO_4 [166]. Additionally, a better durability with maintained stable current after 2.8 h, was attained due to optimal utilization of Pt active sites and its synergism with Ag besides core-shell structure, which provides a shorter path for electrons during HER. This also indicates that using Ag, which is relatively low-cost, and earth-abundant, can decrease the cost for HER. Therefore, porous $Pt_{68}Ag_{32}$ nanodandelions with an average diameter of 78.6 nm were formed by the co-reduction using ascorbic acid and hydrazine in the presence of amrinone as stabilizer/structure directing agent driven by the oriented and Ostwald ripening growth mechanism (**Fig. 6d**) [167]. The composition could be easily tuned by changing the ratio of Pt/Ag to form $Pt_{75}Ag_{25}$ NCs and $Pt_{56}Ag_{44}$ NCs. The HER performance of $Pt_{68}Ag_{32}$ was superior to $Pt_{75}Ag_{25}$ and $Pt_{56}Ag_{44}$ with a lower η_{10}/Tafel slope of 51 mV/39 mVdec^{-1} similar to Pt/C in 0.5 M H_2SO_4 (**Fig. 6e**) [167]. However, $Pt_{68}Ag_{32}$ displayed 96.68 % of its initial current density after 2.8 h, which was greater than its counterparts $Pt_{75}Ag_{25}$ NCs (curve b, 61.64 %) and $Pt_{56}Ag_{44}$ NCs (curve c, 39.96 %) (**Fig. 6f**) [167]. This implies that Ag loading with 32 wt% is the optimum for enhancement of the HER activity of Pt, but this loading is still relatively low, and optimization of the adsorption energy of hydrogen on PtAg alloys with higher Ag loading ought to be scrutinized. Exfoliated 2D-$Ti_3C_2T_x$ MXene supported PtPd nanoparticles ($PtO_aPdO_bNPs@Ti_3C_2T_x$) where (a = 0,1,2 and b = 0,1) were prepared via initial HF-etching assisted formation of $Ti_3C_2T_x$ followed by plasma-irradiation under varying times (1, 3, and 5 min) to form PtPd NPs for promoting the HER activity in 0.5 M H_2SO_4 [168]. Mainly, $PtO_aPdO_bNPs@Ti_3C_2T_x$ (3 min) showed a lower η_{10}/Tafel slope of 26.5 mV/ 39 mV dec^{-1} than $PtO_aPdO_bNPs@Ti_3C_2T_x$ (5 min), $PtO_aPdO_bNPs@Ti_3C_2T_x$ (1 min), and HT-$PtO_aPdO_bNPs@Ti_3C_2T_x$ and comparable to Pt/C (12.5 mV/37 mV dec^{-1}) [168]. This also delivered good activity in 0.1 M KOH with η_{10}/Tafel slope of 57 mV/95 mV dec^{-1} due to the alloying/synergetic effect, variety of metal oxidation state, high surface area/defects of MXene with highly distributed small-sized (2.5 nm) and stabilized nanoparticles with low loading as 1.07 μg cm^{-2}. This indicates the possibility of using MXene as a support for metal-based catalysts with low loading (0.074 wt%) for the HER. The size of this Pt-based is usually larger than 10–15 nm, and their loading is high. Ultrafine sub-3 nm PtNi embedded in microspores carbon nanosheets ($PtNi_2$/CNS-x) were prepared via in-situ polymerization of metals precursors in acetylacetone and annealing at varying temperatures (x = 400, 500, 600, 700 and 800 °C for 3 h in Ar) [169].

Changing the annealing temperature and Pt/Ni ratio had a noticeable effect on the HER performance wherein $PtNi_2$@CNS-600 was found to be the best with a lower η_{10}/Tafel slope of 68 mV/35.27 mV dec^{-1} relative to $PtNi_{1.5}$@CNS-600, PtNi1@CNS-600, $PtNi_3$@CNS-600, $PtNi_2$/CNS-700, $PtNi_2$/CNS-800, $PtNi_2$/CNS-400, and $PtNi_2$/CNS-500 in 0.5 M H_2SO_4. In addition to alongside durability for 2000 cycles and reserved current density for 30 h on $PtNi_2$@CNS-600 [169]. The superior HER activity is attributed to the synergistic effect of PtNi and their tiny size, with quantum effect, and the high surface area beside porosity and surface area of CNS, which hasten the charge-transfer efficiency. This study indicates the possibility of promoting the HER at a low loading of PtNi 0.074 wt% and could also be extended for other metals, which is significant development for the large-scale applications.

Porous PtPd curled nanosheets with a thickness of 6 nm (PtPd NSs) were prepared by co-reduction with ascorbic acid and hydrazine hydrate in the presence of benzyldimethylhexadecylammonium chloride (HDBAC) as structure directing agent (**Fig. 6g, h**) [170]. The high surface area (40.12 m^2/g), 2D structure, rough surface, and porosity of ensued PtPd NSs, led to HER activity close to Pt/C with η_{10}/Tafel slope 22 mV/ 37 mV dec^{-1} in 0.5 M H_2SO_4 in addition to durability for 1000 cycles and reserved current density for 12 h (**Fig. 6i, j**) [170]. This study implies the effect of porous 2D nanosheets on promoting the HER activity and also raises the possibility of the formation of Pt-based alloy in 2D sheets, which has been a grand challenge because metals tend to grow into 0D to rescue their total surface energy during the reduction process. However, both Pd and Pt are highly expensive and rare, which can not reduce the cost of HER and do not match the sustainability requirements, thus necessitating the replacement of Pd with other transition metals. MCo@NC (M = Pt, Pd, Ru) were synthesized via mixing metal precursor with ZIF-67 template and then annealing them at 900 °C for 2 h in N_2 (**Fig. 7a**) to form wrinkled polyhedral carbon cages (200–300 nm) with mesoporous structure and high surface area of 171.4–178.7 m^2/g derived from ZIF-8 decorated with monodispersed nanoparticles (**Fig. 7b**) [171]. Among them, PtCo@NC displayed the highest HER activity with the lowest η_{10}/Tafel slope of 38 mV/51 mV dec^{-1} compared with PdCo@NC, RuCo@NC, Co@NC, and NC (**Fig. 7c**) in 1 M KOH. Also, PtCo@NC displayed 90 % retention after 24 h and 2000 cycles durability (**Fig. 7d**), owing to a highly synergistic effect and abundant Co-N_x centers, the modulated d-band center of Pt in addition to outstanding properties of NC, which accelerated charge mobility and reduced binding energies of intermediates. However, the MOF-derived synthesis method is time-consuming and demands energy, which does not satisfy the practical requirement. PtCo nanoparticles with small-sized 2.7 nm embedded in porous carbon derived from ZIF-67 MOF (CPt@ZIF-67) were prepared via direct annealing of Pt-doped ZIF-67. They had a lower η_{10}/Tafel slope of 50 mV/ 27 mV dec^{-1} than Pt/C and C@ZIF-67 in 0.5 M H_2SO_4 beside exhibiting durability for 24 h [172]. Furthermore, the TOFs of CPt@ZIF-67 (2.94 s^{-1}@η_{100}) were found to be superior to other published noble-metal or non-noble metal-based catalysts like Ni-C-N NSs (η_{10} = 100, TOF = 0.44 s^{-1}) [173] and Li-PPS ND (η_{10} = 140, TOF = 1.6 s^{-1}) [174]. The annealing temperature and time had a significant effect on the HER performance of CPt@ZIF-67, which was in the order CPt@ZIF-67-900-6 > CPt@ZIF-67-800-2 > CPt@ZIF-67-1000-2 > CPt@ZIF-67-900-2 > CPt@ZIF-67-600-2 > CPt@ZIF-67-700-2. The superior activity is due to quick charge transfer, high electron conductivity of carbon with N—Co x sites, and its ability to stabilize PtCo against aggregation or dissolution. This study implies the possibility of low-loading Pt on enhancement of the HER activity relative to commercial Pt/C. Porous Au_3Pt alloy was grown on Ni foam (pAu_3Pt/NF-x) by self-assembly using a polystyrene-b-poly ethylene oxide template, and in-situ galvanic replacement had a well-defined spatial structure with interwoven network pores (**Fig. 7e, f**) [175]. The concentration of polystyrene-b-poly ethylene oxide and reaction time had a significant effect on the HER performance, where pAu_3Pt/NF obtained using 10 mg surfactant after 10 min reaction time delivered excellent HER activity with the lowest η_{50}/Tafel slope of 40.1 mV/42.4 mV dec^{-1} than pAu_3Pt/NF-0-20 and Pt/C in 1.0 M KOH (**Fig. 7f**) [175]. Additionally, pAu_3Pt/NF remained stable for 2000 cycles with durable current for 30 h (**Fig. 7h**). This is due to the alloying effect and interconnected porous structures with high surface area, which make Pt more accessible during the HER. However, alloying Pt with Au can not reduce the HER cost because both metals are highly expensive and not earth-abundant.

Porous carbon-supported Pd with surface-decorated Pt (CS-PdPt) was obtained deploying a PdAg template and galvanic replacement which had a higher HER activity than PdPt and PdAg [176]. The CS-PdPt displayed a superior HER activity with a lower η_{10}/Tafel slope 26 mV/ 33 mV dec^{-1} in 0.5 M H_2SO_4, 46 mV/88 mV dec^{-1} in 1 M KOH, and 50 mV/107 mV dec^{-1} in 1 M PBS, respectively relative to Pt/C, RuO_2, PdPt, and PdAg [176]. This is due to the porous structure and coupling alloy effect with enhanced electrical conductivity and high surface area of CS,

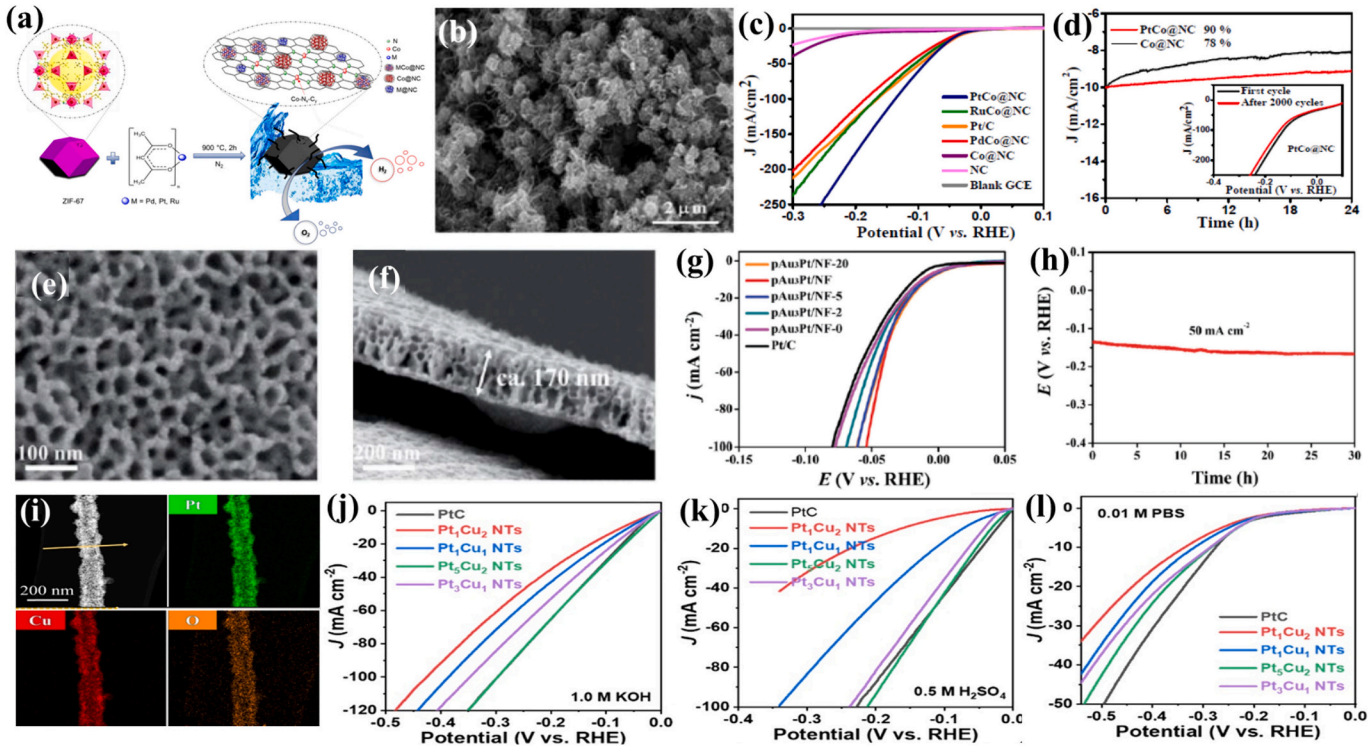

Fig. 7. (a) Synthesis process, (b) SEM, (c) LSVs of PtCo@NC compared with its counterparts, and (d) CA and LSV stability 2000 cycles of PtCo@NC. Reproduced with permission from Ref. [171] Copyright 2020 RSC. (e-f) SEM image of pAu_3Pt/NF and its (g) LSVs compared with counterparts, and (h) CA stability test@η_{100}. Reproduced with permission from Ref. [175] Copyright 2020 RSC. (i) EDX elemental mapping images, LSVs of Pt_5Cu_2 NTs, and their counterparts in (j) 1 M KOH, (k) 0.5 M H_2SO_4, and (l) 0.01 M PBS. Reproduced with permission from Ref. [177] Copyright 2023 Elsevier.

which reduces the charge transfer resistance and enhance the interaction with electrolytes.

Porous nanocarbon (PC) derived from nano-MOF-5(Zn) at 950 °C supported on FePt (Fe-Pt/PC) prepared by the solvothermal method at 160 °C in ethylene glycol encompassed metal precursor promoted the HER activity than that of Nano-MOF-5(Zn), Fe—Pt, and PC with a lowest η_{10}/Tafel slope of 85.4 mV/42.4 mV dec^{-1} in 1 M NaOH [178]. This is due to coupling properties of PC (i.e., great surface area 986 m^2 g^{-1}, pore volume 0.584 cc g^{-1}, and electrical conductivity) with alloy effect of Fe—Pt and modulated d-band of Pt. These merits not only enhance the charge mobility but also tune the hydrogen adsorption energy during HER [178]. This study proved the feasibility of earth-abundant and low-cost Fe in the enhancement of Pt's HER activity. However, PC could be obtained from other sources rather than MOF to decrease the overall cost.

Porous nitrogen-doped carbon (BMNC) rhombic dodecahedron structure derived from Zn—Co zeolite imidazolate (ZIF) supported ultrafine Pt_xNi_y nanoparticles were prepared by hydrothermal treatment at 160 °C and carbonization at 900 °C, and their HER activity depended on the Pt/Ni ratio [179]. Pt_2Ni_2/BMNC was found to be optimum with a lower η_{10}/Tafel slope of 27 mV/ 17.7 mV dec^{-1} than those of Pt_2Ni/BMNC, Pt_2/BMNC, PtNi/BMNC, Pt/C, Pt/BMNC (36 mV) and Ni/BMNC in 0.5 M H_2SO_4; the durability for 3000 cycles with only 7.4 % activity loss was discerned. This is due to combination the properties of alloy with BMNC, which accelerate HER kinetics and enhance the usage of exposed Pt active sites, making Pt_2Ni_2/BMNC being superior to other PtNI-based catalysts like PtNi/CNFs (η_{10}/Tafel slope of 34 mV/31 mV dec^{-1}) [180], PtNi/10PG CNCs (η_{10}/Tafel slope of 31/18 mV dec^{-1}) [181]. However, these porous binary Pt-based catalysts and their morphologies do not offer a short path for electrons during the HER, compared to porous one-dimensional shapes. Thereby, hollow porous Pt_xCu_y nanotubes with different Pt/Cu ratios (i.e., Pt_1Cu_2 NTs, Pt_1Cu_1 NTs, Pt_5Cu_2 NTs, and Pt_3Cu_2 NTs) were prepared by the solvothermal at 180 °C/4 h and then etching [177]. The Pt_5Cu_2 had a hollow nanotube shape with a width of 50 nm and a surface area 3.3 m^2g^{-1} (Fig. 7i). Pt_5Cu_2 NTs were highly active with a lower η_{10}/Tafel slope of 32 mV/27 mV dec^{-1} in 0.5 M H_2SO_4, 34.0 mV/56 mV dec^{-1} in 1.0 M KOH, and 275 mV/ 136 mV dec^{-1} in PBS (Fig. 7j–l). In addition, it has excellent durability after at least 10,000 cycles and stable current density for 50 h in KOH and 30 h in H_2SO_4 and PBS [177]. This reflects the substantial effect of porous nanotubes on providing a short electron path during HER and making Pt active sites more accessible. Meanwhile, this method is highly promising for large-scale applications because it can decrease Pt-loading by 50 % via alloying with earth-abundant metals. Since Pd-based alloys are also known for their outstanding performance for HER, so porous binary systems were synthesized deploying assorted methods on different supports. To this end, porous $PdBi_2$-BA-D 3-D interconnected spherical-like formed by the $NaBH_4$ reduction and then annealing showed a lower η_{10}/Tafel slope of −78 mV/ 63 mV dec^{-1} relative to Pd/C catalyst [182].This is because of the alteration of the d-band center of Pd by Bi, lead to the optimal energy requirement for hydrogen adsorption. Porous Pd-Cu-S nanocubes formed via the dealloying of Ti-Cu-Pd followed by sulphurization enhanced the HER with a lower η_{10}/Tafel slope of −58 mV/35 mV dec^{-1} than Pd—S and Pd nanoparticles in H_2SO_4 electrolyte [183]. In addition, they had great durability for 48 h even in in 7 M H_2SO_4 solution, due to nanoporous morphology and alloy effect. PdNi nanoparticles well dispersed on carbon nanofiber (PdNi/CNF-1:2) (Fig. 8a, b) were formed by the electrospinning and annealing method, which enhanced the HER with a lower η_{10}/Tafel slope 55 mV/57 mV dec^{-1} than Pd/CNF and Ni/CNF in 0.5 M H_2SO_4 (Fig. 8c) [184]. They exhibited good durability with maintained current density for 36 h, owing to stabilization of PdNi into CNF and short electron path on 1D fiber (Fig. 8d). This method is promising for practical application due to the simplicity of the electrospinning method, but the ratio of Ni/Pd ought to be optimized in different electrolytes. The performance of Pt@Pd nanoflowers/rGO was

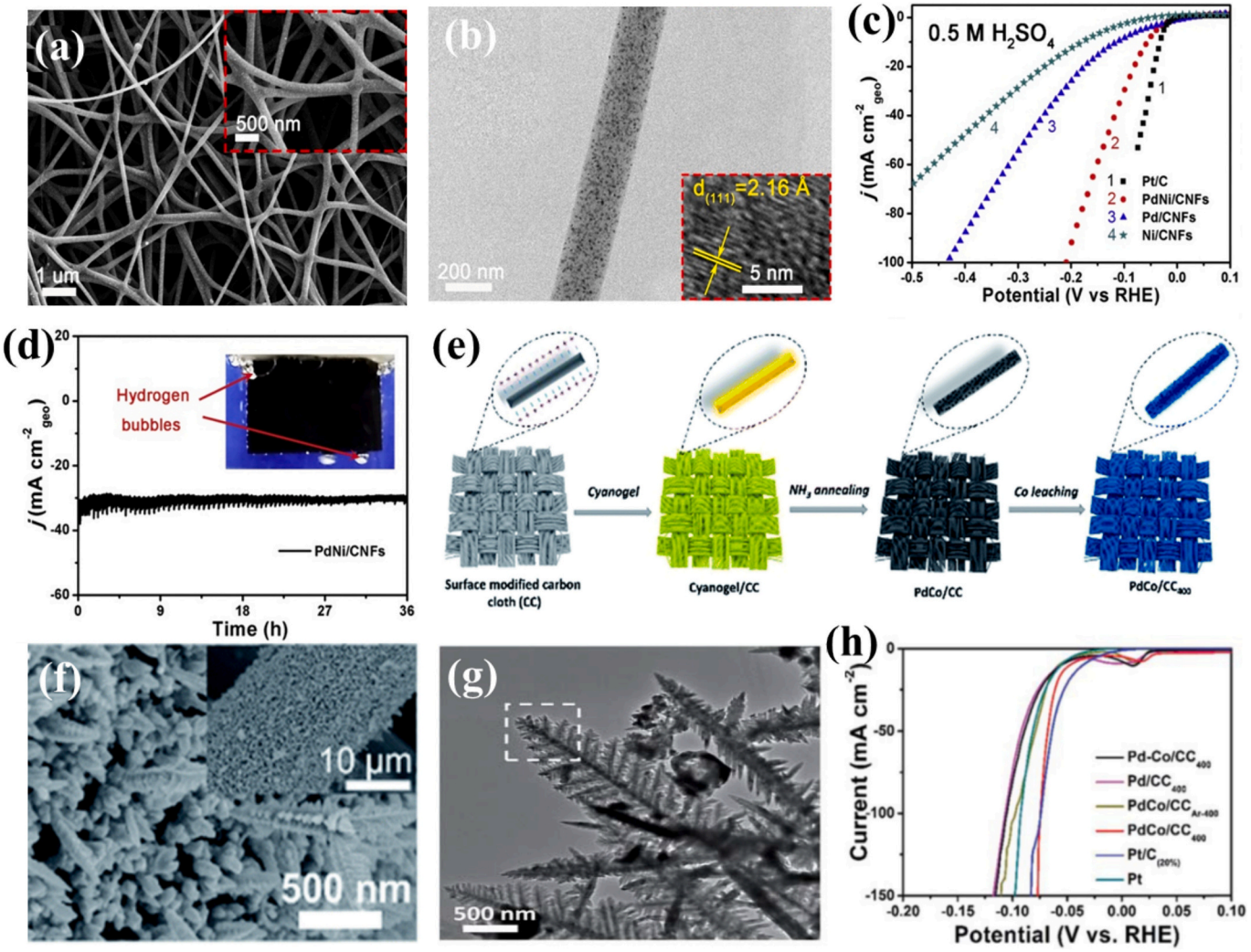

Fig. 8. (a) SEM, (b) TEM, (c) LSVs of PdNi/CNFs relative to its counterparts, and (d) CA test at η_{50} of PdNi/CNFs. Reproduced with permission from Ref. [184] Copyright 2017 Elsevier. (e) Preparation scheme, (f) SEM and (g) TEM of $PdCo/CC_{400}$ and its (h) LSVs compared with its counterparts in 0.5 M H_2SO_4. Reproduced with permission from Ref. [187] Copyright 2020 RSC.

higher than that of Pt NPs/rGO, Pd/C, and Pd NCs/rGO with a lower η_{10}/Tafel slope of −56 mV/39 mV dec^{-1} in 0.5 M H_2SO_4 [185]. With stability for 2.77 h, owing to coupling merits of Pt@Pd nanoflowers with rGO, which enhanced the electrolyte interaction, reduced charge transfer resistance, and stabilized Pt@Pd against aggregation. However, both Pd and Pt are highly scarce on the earth and expensive, so alloying Pd with earth-abundant transition metals is preferred for low-cost HER. The Pd nanoparticles/Mn_3O_4 nanooctahedron (Pd-Mn_3O_4–1) formed via thermodynamic protocol allowed redox transformation reaction using 1 mL Pd solution which enhanced the HER performance relative to that of Pd-Mn_3O_4–2, Pd-Mn_3O_4–0.5, and Mn_3O_4 with a η_{10}/Tafel slope of 50 mV/42 mV dec^{-1} in 0.5 M H_2SO_4 [186]. This is besides durability for 5000 cycles and 97 % activity retention after 36 h. Furthermore, Pd-Mn_3O_4–1 showed higher HER activity in 0.5 M H_2SO_4 than in 0.1 M PBS and 0.5 M KOH. This study indicates the substantial combination effect of Pd with Mn_3O_4 on the enhancement of the HER activity, which is important for the large-scale application because of the good activity at varying pH values.

A series of Pd_xRu_{100-x} spherical-like alloys embedded porous carbon nanosheets (CNs) prepared by $NaBH_4$ burst reduction enhanced the HER relative to Pd/C wherein $Pd_{50}Ru_{50}$/CNs was found to be optimum with a lower η_{10}/Tafel slope of 37.3 mV/67.9 mV dec^{-1} in 0.1 M KOH and 45.1 mV/ 67.6 mV dec^{-1} in 0.5 M H_2SO_4 compared to $Pd_{33}Ru_{67}$/CNs $Pd_{67}Ru_{33}$/CNs, Pd_{100}/CNs, Ru_{100}/CNs and Pd/C) [188]. This is due to the lower particle size of ~3.67, high specific surface area of ~489.565 m^2g, and coupling alloy effect with CNS merits. These properties stabilize PdRu against aggregation and optimize hydrogen adsorption energy, as $Pd_{50}Ru_{50}$/CNs remained stable for 3000 cycles. However, Ru metal is also expensive, which can not decrease the HER cost of a Pd-based catalyst. To circumvent this barrier, PdCo nanodendrites alloys were grown on a carbon cloth sheet ($PdCo/CC_{400}$) by cyanogel template and annealed at 400 °C under NH_3/Ar and then electrochemical cycling under acidic conditions (Fig. 8e). $PdCo/CC_{400}$ had well-defined porous dendritic structure with high-index facets (Fig. 8f–g) which enhanced the HER with a lower low η_{10}/Tafel slope of 75.0 mV/22.6 mV dec^{-1} and TOF of 10.96 s^{-1} in 0.5 M H_2SO_4 relative to PdCo/CC spherical-like and Pt/C (Fig. 8h) [187]. This originated from the porous dendritic shape with high-index facets and high-density active sites beside the alloying effect, which renders Pd active sites more accessible and stabilized against agglomeration. The $PdCo/CC_{400}$ maintained its stability for 1000 cycles and stable current density after 48 h without any changes in the shape or composition. This indicates the great feasibility of Co for enhancement of the HER activity of Pd, with the option of additional transition metals ought to be explored with Pd. In this context, PdCu nanoparticles supported on ordered mesoporous silica and multi-walled carbon nanotubes (PdCu/SBA-15-MWCNTs-CPE) were synthesized by

electrochemical deposition and galvanic replacement [189]. PdCu/SBA15-MWCNTs-CPE outperformed PdCu/SBA15-MWCNTs, PdCu/MWCNTs-CPE, PdCu/SBA15-CPE, Cu/SBA15-MWCNTs-CPE, SBA15-MWCNTs-CPE, and MWCNTs-CPE with a lower η_{10}/Tafel slope of ~250 mV/45 mV dec^{-1} in 0.5 M H_2SO_4 electrolyte with 0.1 M sodium dodecyl sulfate [189]. This is in addition to great stability for 11.5 h, due to the alloying and synergetic effect of PdCu besides the physicochemical merits of SBA-15 and MWCNTs (i.e., porosity, high surface area, and short electron path). This study may open new avenues for the utilization of surfactants with various electrolytes to realize higher HER current density at a lower potential.

Compared with Pt, Pd, and other binary noble-metal electrocatalysts were also synthesized for enhancement of the HER. Fig. 9a shows the SEM image of Ni_xRh_{1-x}@200 °C nanofibers with a porous bundle of rocks obtained by electrospinning, calcination under O_2 at 1000 °C, which were then reduced under H_2/Ar flow at 100–300 °C [190]. The HER performance of Ni_xRh_{1-x} depended on reduction temperature in different electrolytes, but Ni_xRh_{1-x}@200 °C was found to be the best with the lowest η_{10} of 7, 9.4, and 24 mV in 1 M NaOH, 1 PBS, and 1 M $HClO_4$, respectively relative to $NiRh_2O_4$, and Pt/C, and Ni_xRh_{1-x}@200 °C and Ni_xRh_{1-x}@300 °C (Fig. 9b–d) [190]. This is due to the alloying effect synergistic effect besides porous nanofibers, which ease hydrogen adsorption, shorten the charge mobility, stabilize against aggregation, and accelerate kinetics. Thus, Ni_xRh_{1-x}@200 °C showed the lowest Tafel slope of −36.7, −31.4, and − 29.6 mV dec^{-1} in 1 M NaOH, 1 PBS, and 1 M $HClO_4$, respectively, besides great durability for 1000 cycles, which indicate the quick HER kinetics [190]. This study raises the importance of porous fiber structure for promoting HER activity, but the fabrication method should be simplified before rendering it feasible for large-scale applications. Ru, Co nanoclusters decorated on nitrogen-doped porous rhombic polyhedron carbon (Ru-pCo@NC), prepared by the impregnation and calcination of ZnCo-ZIF template at 950 °C for 2 h, displayed outstanding HER activity with a lower η_{10}/Tafel slope of 30 mV/32.1 mV dec^{-1} compared to pCo@NC, and Co@NC in 1 M KOH [191]. This is due to the morphology and Ru—Co active sites within abundant Co-Nx sites of NC derived from MOF with high surface area, which make metal sites more accessible and stabilized during the HER [191]. The Ru-pCo@NC remained stable for 10,000 cycles and maintained durable current density for 40 h. This study raises the possibility of efficient HER activity at a low metal loading of 3.13 wt%, which is important for large-scale operation and sustainability requirements. However, MOF-derived porous carbon requires multiple reaction steps and deploys expensive chemicals. Thus, the exploration of novel supports for binary metal systems is important for reducing the HER cost and large-scale applications. In so doing, vanadium ruthenium oxide/graphdiyne ($VRuO_x$/GDY) (x = 0.012–0.042 V/Ru molar ratio)

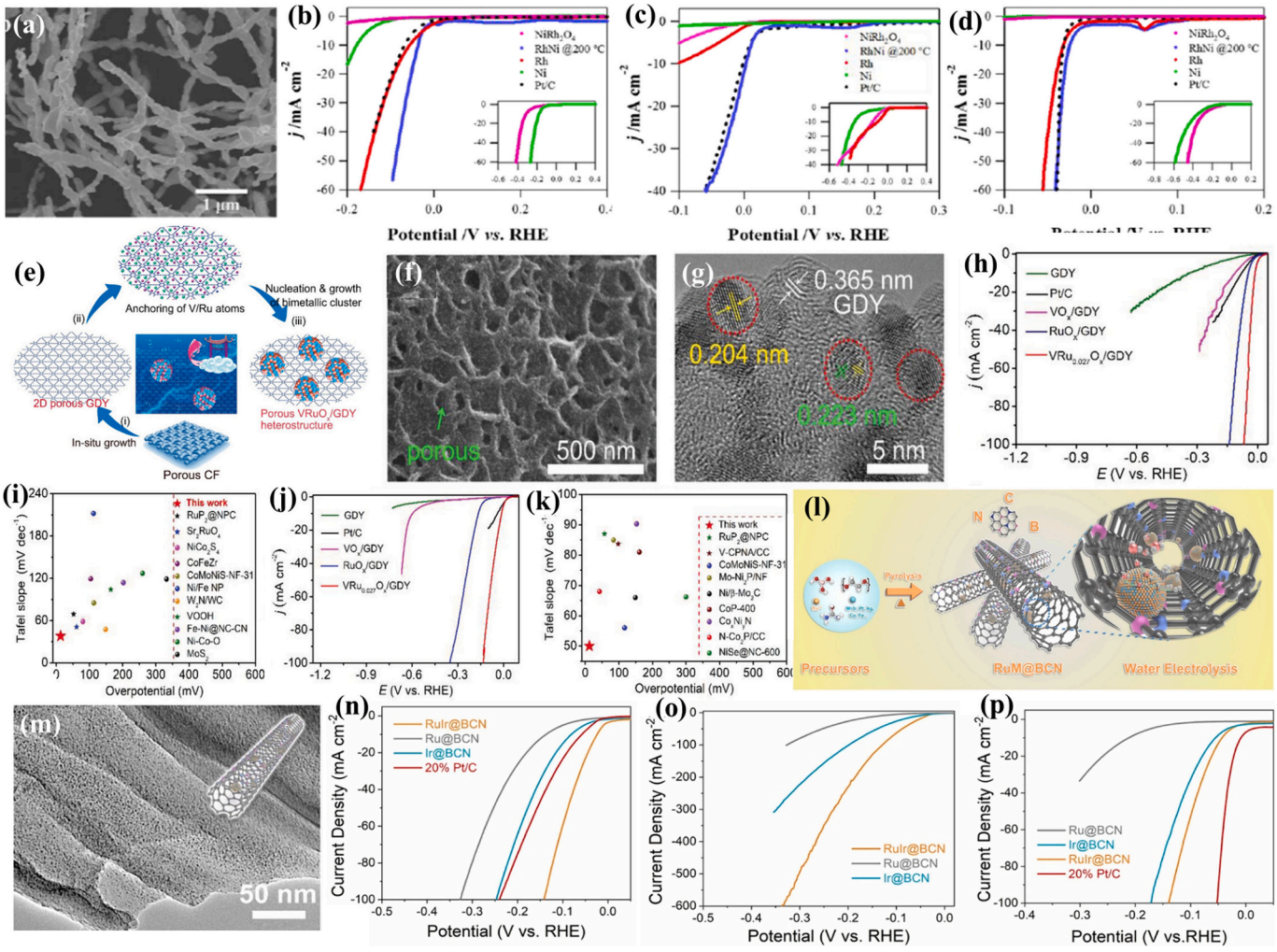

Fig. 9. (a) SEM of Ni_xRh_{1-x}@200 °C, and its LSV with their counterparts in (b) 1 M NaOH, (c) 1 M PBS, and (d) 1 M $HClO_4$. Reproduced with permission from Ref. [190] Copyright 2020 RSC. (e) Schematic preparation method, (f) SEM, and (g) TEM of $VRuO_{0.027}$/GDY and its (h) LSVs in 1 M KOH, (i) HER comparison with reported electrocatalysts, (j) LSVs in 1 M PBS, and (k) it's HER comparison with reported. Reproduced with permission from Ref. [192] Copyright 2021 Wiley. (l) Schematic synthesis and (m) SEM image of RuIr@BCN and its LSVs with its counterparts in (n-o) 1 M KOH, (p) 0.5 M H_2SO_4. Reproduced with permission from Ref. [196]. Copyright 2022 Elsevier.

was prepared by an initial coating of porous GDY coated on carbon cloth fiber (CF) by solvothermal using Cu foil and pyridine at 110 °C under Ar, followed by growth of $VRuO_x$ clusters via the hydrothermal method at 150 °C (Fig. 9e) [192]. The as-formed $VRu_{0.027}O_x$/GDY is composed of spherical nanoclusters with an average size 2.75 ± 0.04 nm on 2D porous and well-distributed GDY with a thickness of 5.47 nm (Fig. 9f–g). The HER activity of $VRu_{0.027}O_x$/GDY was superior to lower $VRu_{0.027}O_x$, RuO_x/GDY, VO_x/GDY, GDY, and Pt/C with the lowest η_{10}/Tafel slope of 13 mV/38 mV dec^{-1} in 1 M KOH (Fig. 9h) [192]. Moreover, $VRu_{0.027}O_x$/GDY outperformed various binary systems like Sr_2RuO_4 (61 mV/ 51 mV dec^{-1}) [193], $NiCo_2S_4$ (80 mV/ 58.5 mV dec^{-1}) [194], and NiRu-LDH (166 mV/ 107 mV dec^{-1}) (Fig. 9i) [195]. Notably, $VRu_{0.027}O_x$ graphdiyne ($VRu_{0.027}O_x$/GDY also enhanced the HER activity with the lowest η10/Tafel slope of 12 mV/50 mV dec^{-1} in 1 M PBS relative to its counterparts (Fig. 9j) and other binary systems (Fig. 9k). This became possible in view of the coupling and unique physicochemical merits of GDY (i.e., electrical conductivity, surface area, and abundant sites for metal atoms) as well as the catalytic properties of $VRuO_x$ and its stabilization within GDY [192]. The $VRu_{0.027}O_x$/GDY remained durable for 23,000 cycles with stable current density after 18 h in KOH and maintained stability for 16,000 cycles while decreasing the current density from 10 to 2 mA after 18 h CA in PBS [192]. Thus, using GDY with Ru/V stabilizes metal active sites and also reduces the energy barrier for hydrogen adsorption, as revealed by the DFT study which affirmed the feasibility of using GDY as a support for binary metals to enhance the HER activity and stability. Besides, it opens the possibility for exploration of other non-noble metals for deployment with GDY [192].

Ir_x-Co electrodeposited on micropore Cu foam with varying Ir loading (x = 4.6, 3.2, and 0.8 mg/cm^2) at pH = 5 and at different temperatures enhanced the HER activity which depended on the Ir loading and temperatures. The $Ir_{3.2}$-Co obtained at 40 °C exhibited the highest HER activity with a lower η_{10}/Tafel slope of ~50 mV/36 mV dec^{-1} compared to $Ir_{4.6}$-Co, $Ir_{0.8}$-Co, Ir, and Co electrocatalysts [197]. It maintained stable current density for 10 h, owing to the alloy effect and modulating the d-band center of Ir with Co that reduced the adsorption energy of intermediates. However, the preparation method requires a lot of precautions, and the loading of Ir is still high. Porous carbon-confined Ru-doped Cu nanoparticles (Ru-Cu@C-n) were prepared by the ion exchange of Cu-BTC with Ru metal and then pyrolysis at 500 °C for 3 h in N_2; the ensued material enhanced the HER activity, which was depended on the Ru contents ($n = 1$, 2 and 3) [198]. The Ru-Cu@C-2 delivered the highest HER activity with a lower η_{10}/Tafel slope of 20 mV/37 mv dec^{-1} compared with Ru-Cu@C-1, Ru-Cu@C-3, and Pt/C along with stability after 1000 cycles in 1.0 M KOH. This is due to the alteration of the d-band center of Ru with Cu and their synergism besides porous morphology with a high specific surface area (156 m^2/g). This study indicates the significant effect of Cu on reducing the Ru loading and enhancing the HER activity suggesting that the preparation method could be applied to other earth-abundant metals. Mo co-doped Ru ultrasmall nanoparticles (3.8 nm) embedded in P-doped porous carbon (P, Mo-Ru@PC) derived from MoCu-MOF (POM@MOF) was synthesized by self-assembly followed by annealing at 700 °C and etching. This resulted in formation of hierarchical porous octahedral nanostructure with meso/micropores and surface area 222 m^2 g^{-1} wherein etching had noticeable effect on the HER activity. Etched P, Mo-Ru@PC displayed a higher activity at a lower η_{10}/Tafel slope of 21 mV/21.7 mV dec^{-1} relative to unetched P, Mo-Ru@PC, Ru@C, commercial Ru/C, commercial Pt/C, PC, and Mo@PC in 1 M KOH. Also, etched P, Mo-Ru@PC had a higher mass activity of 1525 mA mg_{Ru}^{-1} @ η_{10} = 25 mV, high stability for 5000 cycles, and stable current density after 10 h. Meanwhile, etched P, Mo-Ru@PC showed a higher activity in 0.5 m H_2SO_4 with a η_{10} /Tafel slope of 22 mV/25.4 mV/dec. This was derived from the doping effect and rich active sites after etching along with modulation of the electronic structure of Ru by doping, which induces a higher-positive charge state and eases H_2O dissociation at low potential [199]. This study highlights the effect of the co-doping effect and support on the enhancement of the HER performance by Ru.

The RuM-encapsulated B/N co-doped graphitic nanotubes (RuM@BCN, M = Ir, Pt, Ag, Co, and Fe) were synthesized by mixing metal precursors, boric acid, urea, and polyethylene glycol-2000 in water followed by drying and pyrolysis at 950 °C (Fig. 9l) [196]. RuIr@BCN had a well-defined porous nanotube of BCN with uniformly distributed nanoparticles (~2.5 nm) (Fig. 9m) which enhanced the HER activity [196]. RuIr@BCN-2 exhibited the choicest HER kinetic at a low η_{10}/Tafel slope of 23.6 mV/49.6 mV dec^{-1} in 1.0 M KOH relative to RuPt@BCN, RuAg@BCN, RuCo@BCN, RuFe@BCN, Pt/C, Ru@BCN, and Ir@BCN (Fig. 9n) besides stable current density for 110 h. Notably, RuIr@BCN consumed only 335.9 mV to deliver a high current density of 600 mA cm^{-2}, which was superior to Ir@BCN and Ru@BCN, while both delivered a current density of 300 and 100 mA/cm^2, respectively (Fig. 9o). Furthermore, RuIr@BCN showed higher activity at a low η_{10}/Tafel slope of 42.9 mV/59.4 mV dec^{-1} relative to RuPt@BCN, RuFe@BCN, RuCo@BCN, and RuAg@BCN (Fig. 9p) besides stable current for 20 h in 0.5 M H_2SO_4. The outstanding performance of RuIr@BCN originated from the synergism of RuIr and their uniform dispersion on BCN nanotubes, which make them more accessible and durable during HER. This endows the feasibility and competitive advantages of RuIr@BCN for industrial applications. However, the loading of RuIr is relatively high (7.9 %), and both metals are expensive and rare on earth. Therefore, using other earth-abundant metals with either Ru or Ir on BCN will be worthier for the practical low HER cost. Table S1 shows the detailed comparison of thus obtained porous binary noble metal-based electrocatalysts prepared by different methods with various morphologies. It appears that the obtained current density and stability are not up to the level of large-scale applications (i.e., current density only <1 A/cm^2 and stability for a few hours), and their preparation methods are still complicated requiring multiple reaction steps and deployment of hazardous chemicals and that too with the very low yield (i.e., few milligrams/run).

5.2. Porous transition binary-metal carbides/oxides/nitrides for HER electrocatalysis

Porous transition binary metal-based carbides, oxides, and nitrides are among the most promising electrocatalysts for HER, and their performance is shaped by catalyst morphology, composition, and using support (i.e., carbon cloth, graphene, and nickel foam). There are countless porous binary transition metal carbides, oxides, and nitrides synthesized in different shapes, including two-dimensional (i.e., nanosheets and flakes), one-dimensional (i.e., tube, wires, and rods), zero-dimensional (i.e., nanospheres), and multi-dimensional (i.e., polyhedron and cube) for the HER. To this end, $NiMoN_x$ nanosheets enhanced the HER performance with a lower η of 170 mV at two mAcm^2 relative to MoN/C and NiMo/C in 0.1 M $HClO_4$ [200]. $Co_{0.6}Mo_{1.4}N_2$ formed by impregnation and annealing under NH_3 had higher HER activity at a low η_{10} of 200 mV relative to δ-MoN and Co in 0.1 M $HClO_4$ besides durability for 3000 cycles [201] in H_2SO_4. However, the activity of these structures is inferior due to their lower porosity, lower electrical conductivity, and the absence of interfacial interaction. To overcome these barriers, hierarchical nanoporous copper-titanium (np-CuTi) was synthesized by initial formation of $Al_{80}Cu_{19}Ti1$ by arc melting pure Al, Cu, and Ti, followed by immersion in 6 M KOH to etch Al and then dealloying 0.05 M H_2SO_4 solution to partially remove Ti for enhancement of the HER [202]. The np-CuTi showed higher HER activity than commercial Pt/C catalysts, np-Cu, and bare Cu with η_{10} of 50 mV and Tafel slope of 110 mV dec^{-1} besides durability for 5000 cycles, owing to its highly active surface, great surface area, and multimodal porosity with open channels, thus enhancing the accessibility of active sites and accelerate mass transport [202]. Notably, the HER activity of np-CuTi depended on the Cu/Ti ratio, but np-$Cu_{95}Ti_5$ was found to be optimum. This process conversion made CuTi active for HER, because of their unique porous structure and high synergism, which possess

hydrogen-binding energy very similar to that of Pt, as confirmed by the DFT. This preparation process could be extended for the synthesis of other multimetallic transition metals.

Ni_3FeN formed by the thermal ammonolysis of ultrathin NiFe-LDH nanosheets had a higher HER activity than Ni_3FeN-bulk, Ni_3N, NiFe mixed oxide with a low η_{10}/Tafel slope of 158 mV/ 42 mV dec^{-1} beside durability for 9 h in 1 M KOH [203]. This is due to porous morphology with abundant active sites, alloy effect, and interaction with support that enhances the electrical conductivity and adsorption of water, and reducing the adsorption energy of intermediates during the HER. Ni/Mo_2C nanoparticles wrapped with graphene shells (**$NiMo_2C$@C**) were prepared by the carburization treatment of NiMo-MOF and they could deliver a higher HER activity than $NiMo_2C$@C-mixture at a lower η_{10}/Tafel slope of 181 mV/84 mV dec^{-1} mV in KOH and 169 mV/100 mV dec^{-1} in H_2SO_4, besides high stability for 2000 cycles [204]; high electrical conductivity derived from both graphene and carbon contributed to this attribute. This unprecedented study on Ni and Mo_2C nanocomposite derived from binary metal MOF, raises the feasibility for the synthesis of MOF-derived porous binary metals with high electrical conductivity for promoting the HER performance. Spatial Co_6Mo_6C nanoframes on graphene (Co_6Mo_6C-G) were assessed for enhanced HER activity and synthesized using impregnation followed by lyophilization, and annealing under argon atmosphere at 900 °C for 2 h and finally etching in 5.0 mol/L HCl solution. The Co_6Mo_6C-G outperformed $Co_6Mo_6C_x$-G $Co_6Mo_6C_2$-G, and graphene with η_{10} of 154 mV, Tafel slope of 49 mV dec^{-1}, and stability for 10,000 cycles in 0.5 M H_2SO_4 [205] attributable to the porous nanoframe structure with highly exposed active sites and high electrical conductivity of two supports (carbon and graphene). However, the performance of Co_6Mo_6 on individual carbon or graphene support has not been reported. Ni/Mo_2C nanoparticles wrapped with graphene shells ($NiMo_2C$@C) were produced via the carbonization process of porous MOF (NiMo-MOF) and they displayed higher HER activity than $NiMo_2C$@C-mixture (prepared from glucose and urea) with a lower η_{10}/Tafel slope of 169 mV/100 mV dec^{-1} in 0.5 M H_2SO_4 and 181 mV/ 84 mV dec^{-1} in 1 M KOH [204]; it maintained a stable current for 10 h and nearly 5 % loss in activity after 2000 cycles. The superiority of $NiMo_2C$@C is derived from the synergism of NiMo and higher electrical conductivity of graphene shell with carbon, which enhances the interaction with electrolytes and accelerate charge mobility. Among other binary Ni-based and Co-based electrocatalysts for the HER performance, comprise Mo_6Ni_6C/NF with η_{10}/Tafel slope of 51 mV/35.7 mV dec^{-1} in 0.5 M H_2SO_4 [206]. Ni/Ni_2P/Mo_2C@C with η_{10} of 223 mV/183 mV in KOH/H_2SO_4, CoP_3/$NiMoO_4$-NF with η_{10} of 92 mV [207], MoS_2/NiCoS nanosheets with η_{10} of 189 mV [208], and Co_2P/Mo_2C/Mo_3Co_3C@C with η_{10} of 182 mV in 0.5 M H_2SO_4 are some additional examples [209] including CoP_3/CoMoP/NF HNAs with η_{10} of 89 /125 mV in KOH/ H_2SO_4 [210], CoFe/N_H-C NS with η_{10} of 230 mV in 1 M KOH [211], and $NiCo_2S_4$ nanowire with η_{10} of 210 mV [212]. However, their complicated preparation process involving multiple reaction steps and low HER activity have been pronounced barriers.

Covalent organic frameworks (COFs) composed of Fe—Co alloy nanoparticles which were coated by mesoporous carbon layers (C—Fe, Co-COF) enhanced the HER relative to C-COF with η_{10}/Tafel slope of 280 mV/100 mV dec^{-1} in 0.5 H_2SO_4 and 149 mV/330 mV dec^{-1} in 1 M KOH [213]. Notwithstanding the lower activity, the preparation process was very complicated and time-consuming. A leaf-like ZnCo-11-NC derived from self-assembly of MOF and annealing under different temperatures followed by etching in 0.5 M H_2SO_4 afforded a lower η_{10}/Tafel slope of 213 mV/76 mV dec^{-1} in 0.5 M H_2SO_4 and 200 mV/86 mV dec^{-1} in 1 M KOH electrolyte relative to Co-NC and Zn-NC [214]. The performance of ZnCo-11-NC depended on the annealing temperatures 600, 700, 800, and 900 °C, but the sample at 700 °C was found to be optimum in both electrolytes [214]. This is due to the leaf-like morphology and bimetallic effect besides Co-N_x active sites, as ZnCo-11-NC maintained 61 % in H_2SO_4 and 73 % in KOH of its initial current density after 12 h. However, the ratio of Zn in ZnCo-11-NC is very low, which may devalue its effect [214]. Notably, the C—Fe, Co-COF outperformed FeS/Fe_3C@N-S-C-800 (η_{10} = 446 mV) [215], and Fe_3C-Co/NC(η_{10} = 238 mV) [216]. Porous honeycomb carbon (Ni/MoCat@HCC) was formed via the in situ thermal decomposition of $(NH_4)_6Mo_7O_{24}$ followed by a reduction-nitridation reaction deploying SiO_2 as a template and glucose as a carbon source (**Fig. 10a**) [217]. Ni/MoCat@HCC had a well-defined spatial interconnected honeycomb macroporous structure with open channels between adjacent spherical voids of HCC accommodated ultra-small Ni/MoCat nanoparticles (**Fig. 10b**) [217]. These merits endowed the HER performance of Ni/MoCat@HCC with the lowest η_{10}/Tafel slope of 95 mV/74 mV dec^{-1} and durability for 20 h with only 17 % loss in 0.5 M H_2SO_4 along with 136 mV/ 84 mV dec^{-1} and stability for 20 h with 11 % loss in 1 M KOH relative to Ni/MoCat@HCC-L, Ni/MoCat@HCC-H, and HCC-Free Ni/MoCat, respectively (**Fig. 10c, d**) [217]. The higher activity of Ni/MoCat@HCC is attributed to its rich and accessible metal active sites, while others have an insufficient active phase; for instance in Ni/MoCat@HCC-L and excessive Ni/MoCat with lower conductivity relative to others.

Porous MnFeO-NF-0.8 (0.8 is the ratio of Fe/Mn) was formed in flower-like sheets (**Fig. 10e**) via hydrothermal synthesis at 180 °C for 3 h over NF and its HER activity was higher than those of MnO_2-NF, NF, Fe_2O_3-NF, and Mn_3O_4-NF, with η_{10} of 64 mV, Tafel slope of 97 mV dec^{-1} (**Fig. 10f**), and durability for 500 cycles and stable current for 20 h in 1 M KOH [218]. This is due to the lower charge transfer resistance of MnFeO-NF-0.8 and its flower-like shape, which provides channels for ion diffusions. Although the preparation method is simple, the effect of the ratio of Fe/Mn is still ambiguous and not well understood. Meanwhile, the activity of bare NF is higher than Fe_2O_3-NF and Mn_3O_4-NF, which diminishes the activity of Fe or Mn active sites.

A porous CoW carbide nanosheets was grown on an N-doped carbon matrix (Co_6W_6C@NC) via the initial synthesis of leaf-like ZIF-L MOF nanosheets on carbon cloth (CC) by self-assembly then loading with Co/W by ion-exchange and finally annealing under air/H_2 at 700 °C for 2 h (Fig. 10j) to form porous nanosheets (**Fig. 10h**) [219]. Co_6W_6C@NC enhanced the HER activity relative to those of W_2C@NC/CC, Co/CC, and CC with η_{10} of 59 mV and Tafel slope of 45.39 mV dec^{-1}, and stability for 50 h in 1 M KOH (**Fig. 10i**). This is due to the synergistic effect of Co/W modulated electron state and high porosity, which optimizes the hydrogen-binding energy and enhances the electrolyte-electrode interaction, as shown in the lower charge-transfer resistance. Notably, Co_6W_6C@NC outperformed Co_3W_3C NSs/G (η_{10} = 84 mV) [221], Ni/Mo_2C-NCNFs (η_{10} = 143 mV) [222], and C-CWC/glassy carbon (η_{10} = 73 mV) [223]. However, the fabrication process is complicated, and MOF precursors are always expensive. A series of 3D network foam-like aloe waste-derived carbon (3D-AWC)-supported binary metals ($ZnMoO_4$/3D-AWC, $Cu_3Mo_2O_9$/3D-AWC, and $MnMoO_4$/3D-AWC) were synthesized using the hydrothermal treatment of aloe waste followed by mixing with metal salts and co-precipitation followed by annealing at 600 °C for 5 h under N_2 (**Fig. 10j**) [220]. The η_{10}/Tafel slope of $ZnMoO_4$/3D-AWC was 124 mV/54 mV/dec, which was significantly lower than that of $Cu_3Mo_2O_9$/3D-AWC, $MnMoO_4$/3D-AWC, and 3D-AWC in 1 M KOH (**Fig. 10k**). This is beside reserved durable current density for 2.77 h and stability for 1000 cycles, derived from the high synergism and better metallic features of $ZnMoO_4$ [220]. This is evidenced in the calculated DOS which showed a higher working function than the I^-/I_3^- and HER equilibrium potentials on $ZnMoO_4$/3D-AWC. This study is of great importance because it proved the feasibility of biomass waste derived porous carbon-supported binary metal systems for promoting HER performance and aloe waste is earth-abundant and can grow in a variety of harsh conditions. Therefore, other biomass-derived porous carbon ought to be investigated in future. Hierarchical porous dubbed Ni/Mo_6Ni_6C@C was obtained using PEI as a soft template followed by annealing together with POM and metal ions for promoting the HER performance with a lowest η_{10}/Tafel slope of 101 mV/88 mV dec^{-1} in 1 M KOH and 122 mV/116 mV dec^{-1} in 0.5 M H_2SO_4 relative to Mo_2C@C, Ni@C, C and Ni/MoC@C, respectively

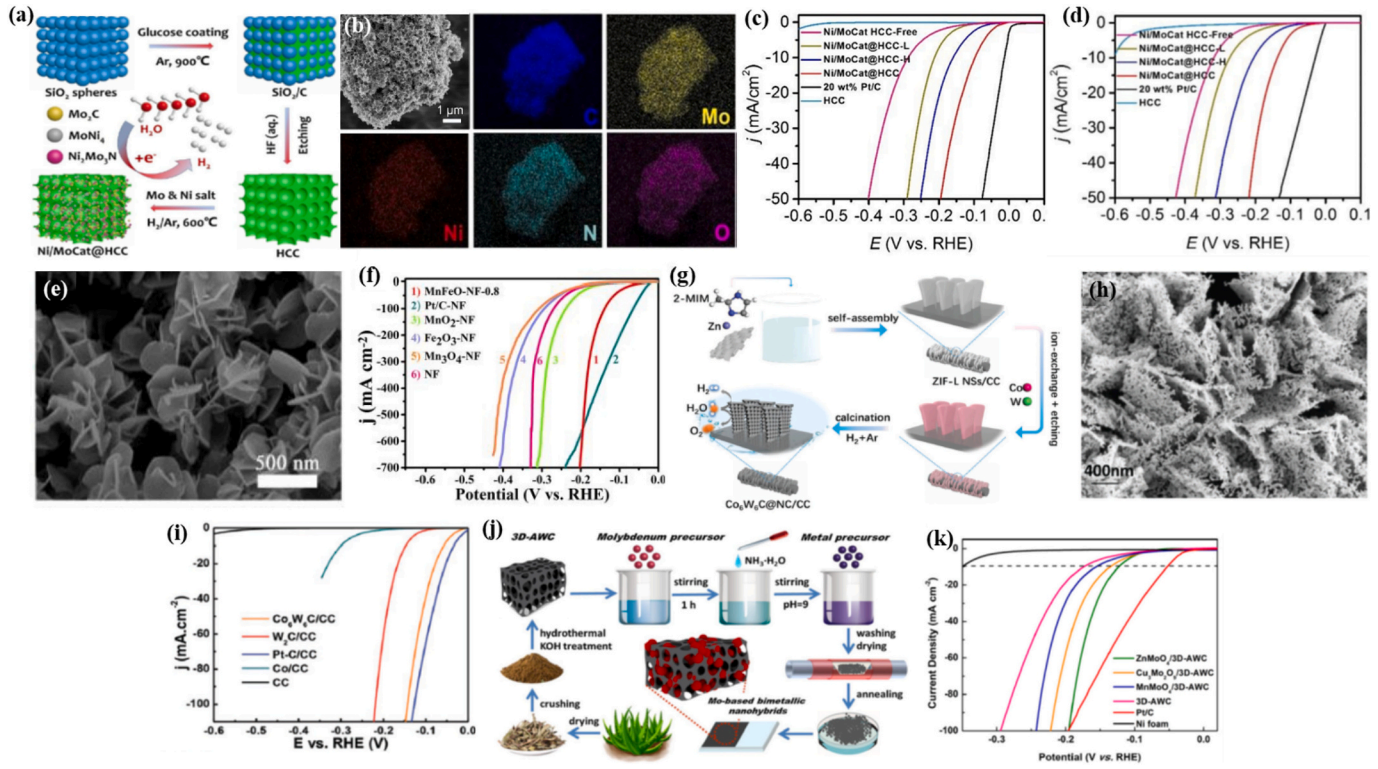

Fig. 10. (a) Formation scheme, (b) EDX elemental mapping of Ni/MoCat@HCC and its LSV compared with its counterparts in (c) 0.5 M H_2SO_4, and (d) 1 M KOH. Reproduced with permission from Ref. [217] Copyright 2019 RSC. (e) SEM image of MnFeO-NF-0.8 and its (f) LSVs in 1 M KOH compared with related counterparts. Reproduced with permission from Ref. [218] Copyright 2020 RSC. (g) Preparation scheme and (h) SEM of Co_6W_6C@NC and its (i) LSVs with related counterparts in 1 M KOH. Reproduced with permission from Ref. [219] Copyright 2020 Willey. (j) Formation scheme of $ZnMoO_4$/3D-AWC and its (k) LSVs relative to its counterparts in 1 M KOH. Reproduced with permission from Ref. [220] Copyright 2020 Elsevier.

[224]. This is besides maintaining better stability for 20 h, owing to the porous morphology, C@C support with high electrical conductivity, and bimetallic effect, which reduces the activation energy for the adsorption of hydrogen as affirmed by the DFT studies, which showed the lowest $\Delta G_{H^*\ on}$ Ni/Mo_6Ni_6C@C relative to its counterparts [224].

CoMo oxyfluoride on graphite felt (CoMoOF/GF) was prepared by the electrodeposition on GF to form CoMoO@GF, followed by the selective Co etching by electrochemical anodic treatment in the presence of NH_4F escorted by the insertion of F atoms (Fig. 11a) [225] to form CoMoOF layer thickness (~1 μm) warped GF enriched with F atoms (Fig. 11b). This implies the structure is maintained after anodic treatment. The HER performance of CoMoOF/GF outperformed CoMoO/GF, CoOF/GF, MoOF/GF, Co oxide/GF, Mo oxide/GF, and GF with η_{10} of 79 mV in 1.0 M KOH, Tafel slope of 43.3 mV dec^{-1}, and durability for 5000 cycles and stable current for 100 h (Fig. 11c, d) [225]. Additionally, CoMoOF/GF showed η_{10} of 94 mV in 0.5 H_2SO_4, and η_{10} of 363 mV in 0.1 M PBS thus making it superior to $CoMoP_2$ (η_{10} = 155) [226], Ag@MoS_2 (η_{10} = 195.7) [227], CoFeP (η_{10} = 114 mV) [228], Co-SA/P-in situ (η_{10} = 98) [229], Co_9S_8-MoS_2/NF (η_{10} = 167 mV) [230], and meso-Fe-MoS_2/$CoMo_2S_4$ (η_{10} = 122 mV) [231] in KOH.

The superior performance of CoMoOF/GF is attributed to the synergism of CoMo and their exposed atoms as well as higher ECSA and electrical conductivity, as has been further attested in the DFT, which showed the smallest ΔG_{H^*} of hydrogen adsorption (close to zero) relative to its counterparts [225]. NiCo NPs (~20 nm) dispersed in 2D foam-like porous N, P-codoped carbon nanosheets (NiCo@N, P-CNSs) were synthesized using the hydrogel-bridged carbothermal method (Fig. 11e) and they had porous 2D puffy nanosheets with rugged surface (Fig. 11f). These features endowed the catalytic activity of NiCo@N, P-CNSs with lowest η_{10} of 99 mV, Tafel slope 46 mV dec^{-1} beside durability for 1000 cycles and stable current for 13.8 h (Fig. 11g) relative to NiCo@N, P-C, Ni@N, P-CNSs, and Co@N, P-CNSs in 1 M KOH [232]. This is because of the alloying effect, porous structure modulated electronic structure, rich active sites, and abundant mass diffusion pathways, which reduces the activation energy for H_2 adsorption on NiCo, as revealed by the lower ΔGH^* value on NiCo (− 0.37 eV) relative to on Co (− 0.40 eV) and Ni (111) plane (−0.42 eV) (Fig. 11h). Therefore, NiCo@N, and P-CNSs were superior to various binary Ni-based systems like $Cu_{0.3}Co_{2.7}P$/NC (η_{10} = 220 mV) [233], NiFe LDH (η_{10} = 210 mV) [234], NiFe LDH/rGO (η_{10} = 560 mV) [235], NiFe-NCs (η_{10} = 197 mV) [236], $Ni_{1.5}Co_{0.5}$@N-C NT/NFs (η_{10} = 114 mV) [237], NiSe@NC (η_{10} = 250 mV) [238], and FeCo@NGC (η_{10} = 211 mV) [239] in 1 M KOH electrolyte.

Finding newer supports for metals is important for promoting their HER performance. Along these lines, $Ti_3C_2T_x$ MXene was used as a co-support for the enhancement of the HER activity of various binary metals systems like NiMo bimetallic carbide encapsulating N-doped carbon (NC) on the 2D $Ti_3C_2T_x$ nanosheets (Ni_3Mo_3C/Mo_2C/$Ti_3C_2T_x$/NC). This was formed by using POM as the soft template, DCA as the carbon source, and $Ti_3C_2T_x$ MXene as a conductive matrix (Fig. 11i) [240]. Coupling properties of MXene with NC and catalytic merits and alloy effect of NiMo endowed the HER performance of Ni_3Mo_3C/Mo_2C/NC with a lower η_{10}/Tafel slope of 99 mV/58 mV.dec^{-1} in 0.5 M H_2SO_4 and 98 mV/69 mV dec^{-1} in KOH, besides 621 mV/304 mV.dec^{-1} in PBS electrolyte compared to Ni_3Mo_3C/Mo_2C/NC, Mo_2C/$Ti_3C_2T_x$/NC, Ni/$Ti_3C_2T_x$/NC, Mo_2C/$Ti_3C_2T_x$, and Ni_3Mo_3C/Mo_2C/$Ti_3C_2T_x$ (Figs. 11j-11l).

Notably, Ni_3Mo_3C/Mo_2C/$Ti_3C_2T_x$/NC maintained stable current for 24 h and durability for 2000 cycles in H_2SO_4, KOH, and PBS electrolytes [240]. This implies the significant effect of combination properties of co-supports $Ti_3C_2T_x$ and NC with electrocatalytic advantages of Ni_3Mo_3C/Mo_2C on enhancing the HER activity relative to either of the supports, Ni_3Mo_3C or Mo_2C [240] which may further promote the utilization of

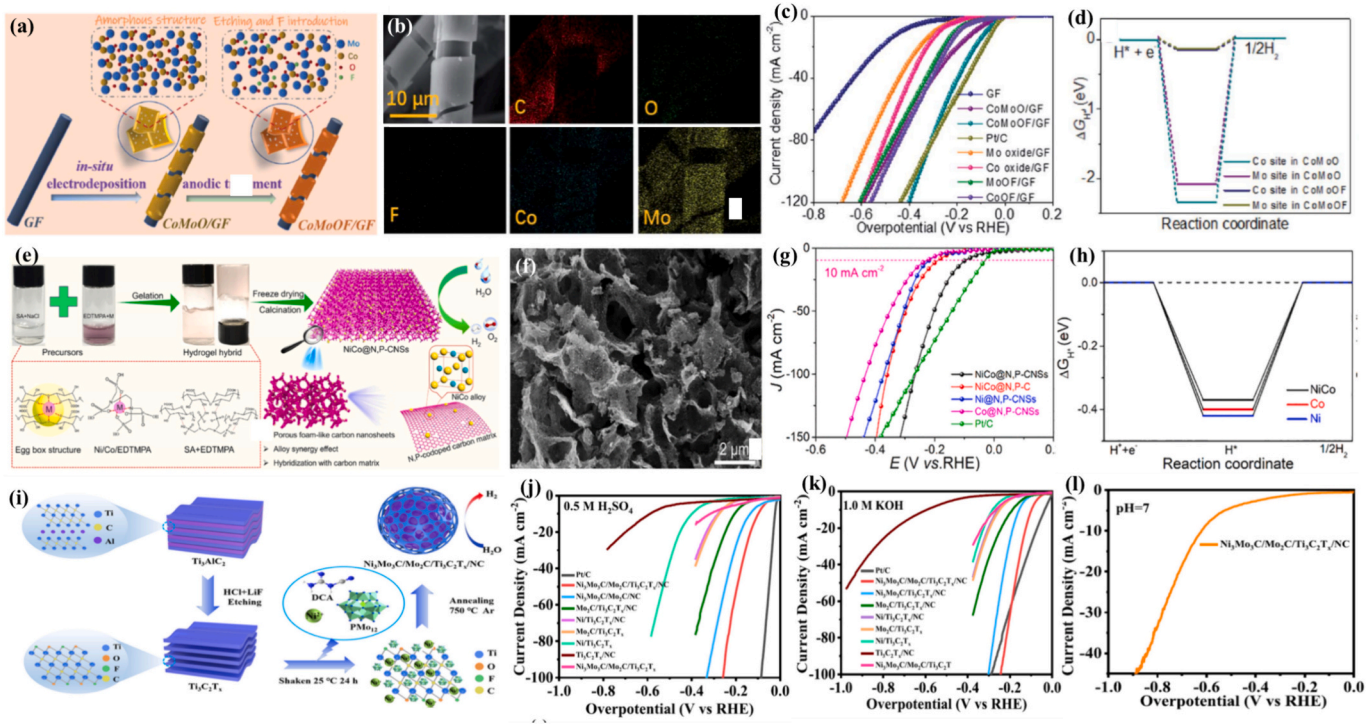

Fig. 11. (a) Scheme for synthesis and (b) EDX elemental mapping of CoMoO@G and its (c) LSVs with other catalysts tested in 1 M KOH, and (d) their HER Gibbs free-energy. Reproduced with permission from Ref. [225] Copyright 2021 RSC. (e) Preparation scheme and (f) SEM image of NiCo@N, P-CNSs and its (g) LSVs with other counterparts in 1 M KOH and (h) Gibbs free-energy of adsorbed hydrogen. Reproduced with permission from Ref. [232] Copyright 2021 Elsevier. (i) Formation process of $Ni_3Mo_3C/Mo_2C/NC$ and its LSVs with other electrocatalysts in (j) 0.5 M H_2SO_4, (k) 1 M KOH, (l) 1 M PBS. Reproduced with permission from Ref. [240] Copyright 2022 Elsevier.

MXenes as co-support in the HER. Various porous binary metals nanospheres were synthesized for the HER like $Ni_3Mo_3C/Mo_2C/Ti_3C_2T_x/NC$ outperformed Mo_2CT_x MXene with η_{10}/Tafel slope of 189 mV/70 mV dec^{-1} [241], $MoS_2/Ti_3C_2T_x$ η_{10}/Tafel slope of 152 mV/70 mV dec^{-1} [242], and $MoS_2/Ti_3C_2T_x$@C η_{10}/Tafel slope of 135 mV/45 mV dec^{-1} in H_2SO_4 electrolyte. Other binary Mo-based electrocatalysts were synthesized for enhancing the HER in KOH, like CoMoP@C η_{10}/Tafel slope of 81 mV/55 mV dec^{-1} [243], MoS_2/Mo_2C microsphere η_{10}/Tafel slope of 115 mV/45 mV dec^{-1} [244], and Ni-doped Mo_XC η_{10}/Tafel slope of 192 mV/98 mV.dec^{-1} [245], which enhanced the HER performance relative to their mono-metal counterparts. Furthermore, in the H_2SO_4 electrolyte, binary Ni-Mo_2C@C with η_{10}/Tafel slope of 72 mV/66 mV dec^{-1} [246], CoP/Co-MOF ($\eta_{10} = 27$ mV) [247], Mo_2C/VC@C with η_{10}/Tafel slope of 122 mV/44 mV dec^{-1} [248], $Co_{0.6}Mo_{1.4}N_2$ 200 mV [201], MoS_x/graphene/Ni Foam ($\eta_{10} = 141$ mV) [249], Mo_xC/Ni ($\eta_{10} = 150$ mV) [250], Co_4Mo_2@NC ($\eta_{10} = 218$ mV) [251], and Mo_xCo_xC@C ($\eta_{10} = 83$ mV) [252] in KOH, which were superior to their monometallic system. Porous spherical-like $Ni_3ZnC_{0.7}$-x (x = annealing temperatures) was derived from NiZn-MOF by the self-assembly and autoclaving followed by annealing under varying temperatures [253]. $Ni_3ZnC_{0.7}$–550 exhibits excellent HER activity with a lower η_{10}/Tafel slope of 93 mV/48 mV dec^{-1} in 1 M KOH compared with Ni/C-550, $Ni_3ZnC_{0.7}$-650, and $Ni_3ZnC_{0.7}$-450 besides durable current density for 24 h [253]. Zn, with its fulfilled 3d orbitals, can not show higher electrocatalytic activity, but it modulated the electronic property of Ni by hybridization with the active metal sites in $Ni_3ZnC_{0.7}$. This study could open the gates for the utilization of atomic cation modulation of metals and their synergy with carbon support for enhancement of the HER activity and durability. However, the effect of metal ratio on the ΔG_{H^*} of hydrogen adsorption need to be investigated in different electrolytes for better optimization [253]. NiCu nanoparticles in situ grown on framework (Ni_xCu_y/C) with tunable Ni/Cu ratio were synthesized via the impregnation of metal salts with tissue papers followed by annealing at 700 °C, and etching in H_2SO_4 [254]. The HER performance was found to be Ni/Cu ratio-dependent, where the $Ni_{0.25}Cu_{0.75}$/C was found to be the best with the lowest η_{10} of 184 mV and Tafel slope of 84 mV dec^{-1} beside maintaining 99 % of its activity after 5.5 h relative to $Ni_{0.75}Cu_{0.25}$/C, $Ni_{0.50}Cu_{0.50}$/C, Cu/C, and Ni/C. This is due to the coupling of the alloying effect of NiCu with electrical conductivity and a high surface area of C, which reduces the hydrogen adsorption energy and tolerates the intermediates, as revealed in the DFT which showed a lower ΔGH^* on $Ni_{0.25}Cu_{0.75}$/C (−0.05 eV) than its counterparts. The preparation approach is feasible for large-scale applications, and while cellulose in tissue paper could act as a reducing agent for metal salts, but it could be simplified further.

A porous carbon-based MoNi electrocatalyst ($Mo_{0.84}Ni_{0.16}$-Mo_2C@NC) with a well-defined nanosphere structure was synthesized by the self-assembly and hydrothermal method to form PMo_{12}@PVP@Zn/Ni-ZIF MOF (Figs. 12a, b) [255]. The meticulous distribution of small Mo—Ni alloy and Mo_2C nanoparticles (15 nm) over N-rich carbon sphere endowed $Mo_{0.84}Ni_{0.16}$-Mo_2C@NC, with higher activity than those of Ni@NC and Mo@NC with lowest η_{10} of 151 mV, Tafel slope of 112 mV dec^{-1}, and highest TOF of 4.5 s^{-1} at η_{380} in 1.0 M KOH (Fig. 12c). The distribution of metal act sites inside the carbon framework makes them more accessible and stabilizes against aggregation, where $Mo_{0.84}Ni_{0.16}$-Mo_2C@NC maintained a stable current for 20 h and durability for 2000 cycles. Notably, the performance depended on the Mo/Ni ratio, but $Mo_{0.84}Ni_{0.16}$-Mo_2C@NC was found to be optimum. However, the relationship between these metal ratios and hydrogen adsorption energy should be scrutinized further. The HER performance of Zn, N co-doped Mo_2C formed in a porous quasi-sphere structure via the solvothermal approach combined with a template-based method using Zn-MOF was found to be superior to commercial MO_2C and Mo_2C-900 with the lowest η_{10} of 169.5 mV and Tafel slope of 62.2 mV dec^{-1} besides durable current for 16.6 h and higher TOF (27.5 μmol/h), in H_2SO_4 solution [256]. This is due to the porous morphology with abundant channels for ion diffusion and enhanced accessibility of

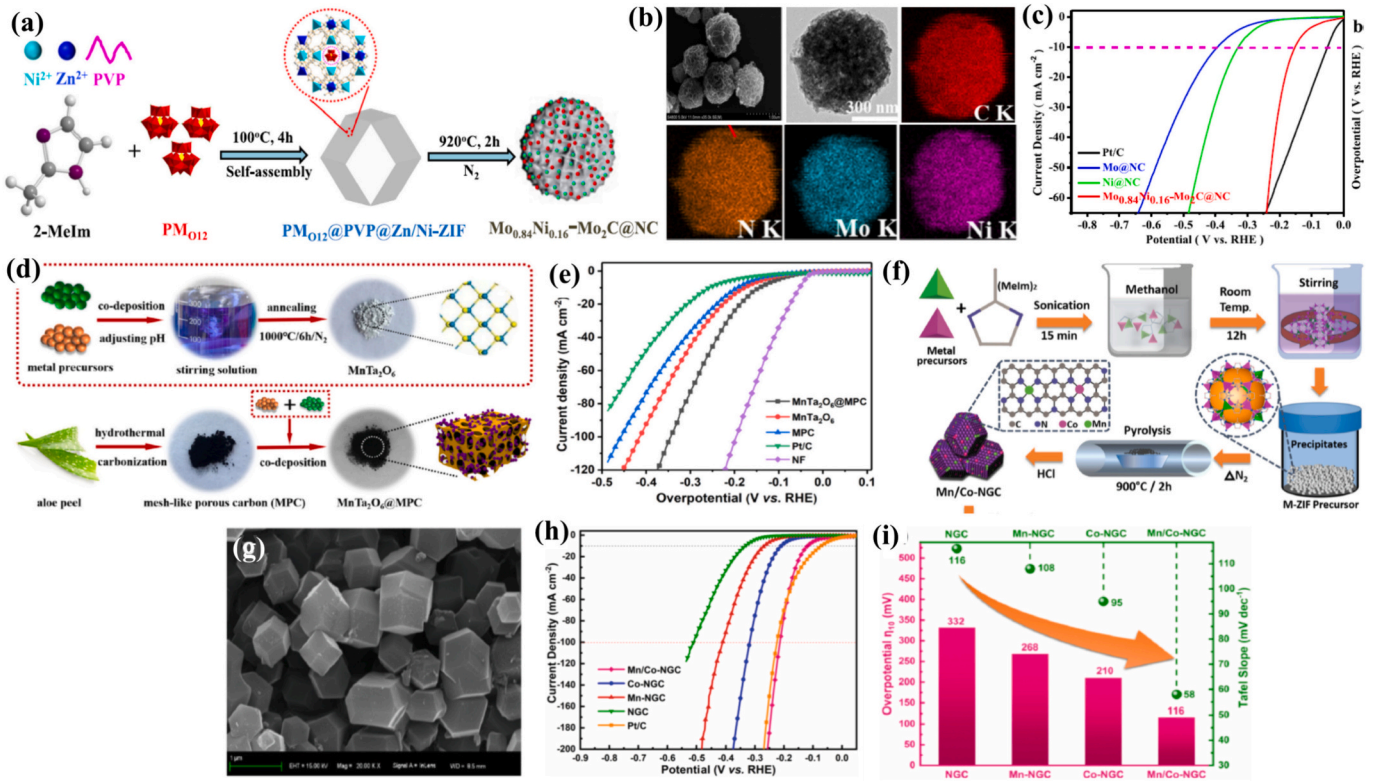

Fig. 12. (a) Preparation scheme and (b) EDX elemental mapping of $Mo_{0.84}Ni_{0.16}$-Mo_2C@NC and its (c) LSVs with other electrocatalysts tested in 1 M KOH. Reproduced with permission from Ref. [255] Copyright 2021 Elsevier. (d) The formation process of $MnTa_2O_6$@MPC and its (e) LSVs with other catalysts measured 1 M KOH. Reproduced with permission from Ref. [257] Copyright 2022 Elsevier. (f) Preparation process and (g) SEM image of Mn/Co-NGC and its (h) LSVs and (i) η_{10} vs. Tafel slopes compared with others in 1 M KOH. Reproduced with permission from Ref. [259] Copyright 2022 Elsevier.

metal act sites in addition to the co-doping effect, which reduces the ΔGH* on Zn, N co-doped Mo_2C relative to undoped Mo_2C as confirmed by the DFT. However, MOF-derived metal carbide catalysts require multiple reaction steps, which devalue their feasibility for large-scale adaptability.

$MnTa_2O_6$ over mesh-like bio-based porous carbon (MPC) was obtained by co-precipitation method and annealing at 1000 °C for 6 h and its HER assessment demonstrated a lower η_{10} of 141.9 mV and Tafel slope of 105 mV dec^{-1}, besides stability for 1000 cycles and stable current for 2.7 h relative to $MnTa_2O_6$, MPC, and NF with hierarchical porous structure in 1 MKOH (Fig. 12d, e) [257]. This outcome is derived because of a great specific surface area (332.743 m^2/g) and coupling catalytic merits and synergism of $MnTa_2O_6$ with electrical conductivity and hierarchical porosity of MPC. The preparation method is simple, but its energy demand and ratio effect of Mn/Ta ratio have not been studied. Hollow NiFe@NPC dodecahedron was formed by autoclaving to form NiFe-ZIF MOF followed by annealing at 900 °C for 4 h under N_2 and then etching in HCl. It showed a lower η_{10}/Tafel slope than that of 150 mV/103 mV dec^{-1} relative to Fe@NPC, Ni@NPC, and NPC in 0.5 M H_2SO_4 [258]. This is beside durable current density for 20 h with only 6.6 % loss in the activity due to a combination of porous morphology and electrical conductivity of NPC with the alloying effect and synergism of NiFe [258]. However, the preparation method of MOF-derived synthesis of NPC is still time-consuming, and energy is demanded along with the necessity for expensive chemicals.

In light of the aforementioned discussed compelling examples, the rational synthesis of porous binary transition metal carbides, oxides, and nitrides for HER electrocatalysts requires multiple reaction steps, hazardous chemicals, and allows the segregation of metals instead of their mixing at the atomic level, which diminishes the effect of metal active sites. Meanwhile, their HER performance is still far from replacement of commercial Pt-group catalysts. Mo_2C nanoparticles (3–4 nm) embedded in hierarchically porous NC polyhedron (ZnMo-MI-1000) derived from ZnMo-MI MOF were formed via solvothermal protocol and then annealing at 1000 °C. They had a lower η_{10}/Tafel slope in H_2SO_4 and KOH compared with ZnMo-MI-900, ZnMo-MI-800, and ZnMo-MI-700 [260]. Mainly, ZnMo-MI-1000 had a η_{10}/Tafel slope of 83 mV/53.1 mV dec^{-1} with 96.8 % durability after 2000 cycles in H_2SO_4 and 101 mV/88.2 mV dec^{-1} with 95.5 stability after 2000 cycles in KOH, due to porous polyhedron structure and inherent metal active sites. 3D structure CoCu@NC nanocubes were synthesized using the surfactant-assisted approach to form ZIF-67 NCs followed by coating with SiO_2 shell via hydrolytic condensation, subsequent annealing and finally etching in HF enhanced the HER activity than that Co@NC with a η_{10} of 199 mV, Tafel slope 143.2 mV dec^{-1}, and durability for 1000 cycles in 1.0 M KOH [261]. This is plausibly attributed to tolerating the adsorption of H^+ intermediate over CoCu, thus pushing the adsorption energy to the top of the volcano plot. The Tafel slope of CoCu@NC higher than Co@NC, which makes the reaction kinetics ambiguous. N-coordinated Mn/Co nanoparticles were grown on rhombic dodecahedral graphitic carbon (Mn/Co-NGC) that was prepared by self-assembly and annealing at 900 °C for 2 h and HCl etching (Figs. 12f, g). They displayed HER activity closer to Pt/C but superior to Co-NGC, Mn-NGC, and NGC with η_{10} of 116 mV and Tafel slope of 58 mV dec^{-1} (Fig. 12h, i) [259]. This is owing to binary metal's active sites, multiple charge transfer channels, and optimized H_2-adsorption energy, as verified by the DFT simulation [259]. Notably, Mn/Co-NGC is promising, although the complicated preparation method and inferior durability of Mn/Co-NGC for only 1000 cycles are some of the limitations.

Various nanotubes were synthesized for the HER, like Ni/CeO_2-CNT η_{10} = 91 [262], Mo_2C-NCNT (η_{10} = 257 mV) [263], CP/CTs/Co-$S_{0.32}$ in 1 M KOH η_{10}/Tafel slope of 190 mV/ 131 mV dec^{-1} [264], $Ni_xCo_{3-x}O_4$ (η_{10} = 450 mV) [265], Mo_2C-Ni@NCNF (η_{10} = 372 mV) [266], and $Co_6Mo_6C_2/Co_2Mo_3O_8$ (η_{10} =220 mV) [267], which had higher

performance than their monometal counterparts. N-doped carbon nanotube frameworks (NCNTFs) accessed via the pyrolysis of a bimetallic metal-organic framework (Co_3Fe_7@NCNTFs) formed by autoclaving at 115 °C for 24 h and annealing at 600 °C for 3 h showed higher HER activity than those of Co_3Fe_7@C, CoFe@C, and CoFe@NC powder with η_{10} of 197 mV, Tafel slope 62 mV dec^{-1}, and 96 % stability after 15 h in 1.0 M KOH [268]. The superior performance of Co_3Fe_7@NCNTFs has been attributed to the synergistic effect of Co_3Fe_7 and NCNTs besides the porous framework structure. NiCo oxide-incorporated 3D N-doped graphene/CNT conductive matrix (NCGC) was obtained by the hydrothermal and annealing approaches and was found to promote the HER with a lower η_{10} of 214 mV and Tafel slope of 106 mV dec^{-1} beside higher durability for 60 h relative to CGC, GC, and NGC in 1 M KOH [269]. This implies coupling two supports NCG and CNT, is preferred over one support due to their impressive surface area and higher electrical conductivity; NCGC being more active than other one-dimensional Ni-based catalysts, among others.

Nanofiber morphology can also offer a short electron path like nanotubes. In this context, FeCo nanoparticles dispersed in hierarchical N-doped CNTs/nanofiber (FeCo@NC-12) were formed by the electrospinning followed by thermal annealing for enhanced HER activity, and its performance depended on the Fe/Co ratio. The ratio of 0.5 mmol/1 mmol was found to be optimum as it revealed the lowest η_{10} of 296 mV and Tafel slope of 106 mV dec^{-1}, and higher durability for 48 h relative to FeCo@NC-11, FeCo@NC-12, FeCo@NC-21, and CNT@CNFs in 1.0 M KOH [270]. Additional binary Co-Fe-based systems were synthesized for enhanced HER performance, like FeS/Fe_3C@N-S-C-800 (η_{10} = 446 mV) [215], CoFe/NH-C NS (η_{10} = 230 mV) [211], NCNT/CoFe-$CoFe_2O_4$ (η_{10} = 227 mV) [271], Co@Co_3O_4/FeNS-rGO (η_{10} = 130 mV) in 1 M KOH [272], and NiCoFeB nanochains (η_{10} = 347 mV) [273]. However, these studies were mainly conducted using glassy-carbon electrodes, which are known for their lower interaction with the electrolytes. Thus, the effect of Co/Fe ratio impeded on 1D nanostructures should be investigated in future over other electrodes like metal foam or carbon cloth due to their outstanding electrical conductivity and better interaction with the electrolytes. Mo_2C and Ni spherical-like nanoparticles have been synthesized with in-situ formed interfaces encapsulated by porous carbon nanofibers (Ni-Mo_2C-CNF) via electrospinning, annealing, and hydrothermal methods for augmenting the HER with the lowest η_{10} of 196 mV and Tafel slope of 54.7 mV dec^{-1}, relative to Ni-Mo_2C-CNF-H and Ni-CNF besides maintained current density for 10 h in 1 M KOH [274]. This implies that the in situ formed interface is preferred over the ex-situ interface to promote the HER performance. However, the preparation method is complicated, which lessens its feasibility for practical utilization. The annealing temperature had a noted effect on the catalytic activity, but 800 °C was found to be ideal. CoFe-N-CNTs/CNFs-900 was synthesized by the electrospinning of PVP containing Zn/Co/Fe precursors followed by pre-oxidation at 200 °C for 7 h to form CoFeZn-PVP nanofibers followed by annealing at 550 °C with melamine under H_2/Ar 550 °C and then at 900 °C (Fig. 13a) [275]. CoFe-N-CNTs/CNFs-900 had dense ultra-long nanofibers wrapped nanotubes in the form of an interconnected network (Fig. 13b), which is important for promoting ion diffusion and making metal sites accessible during HER. The CoFe-N-CNTs/CNFs-900 had a lower η_{10} (181 mV), Tafel slope (101 mV dec^{-1}) than those of CoNi-N-CNTs/CNFs-900 and FeNi-N-CNTs/CNFs-900 in 1 M KOH (Fig. 13c), besides higher durability for 3000 cycles and stable

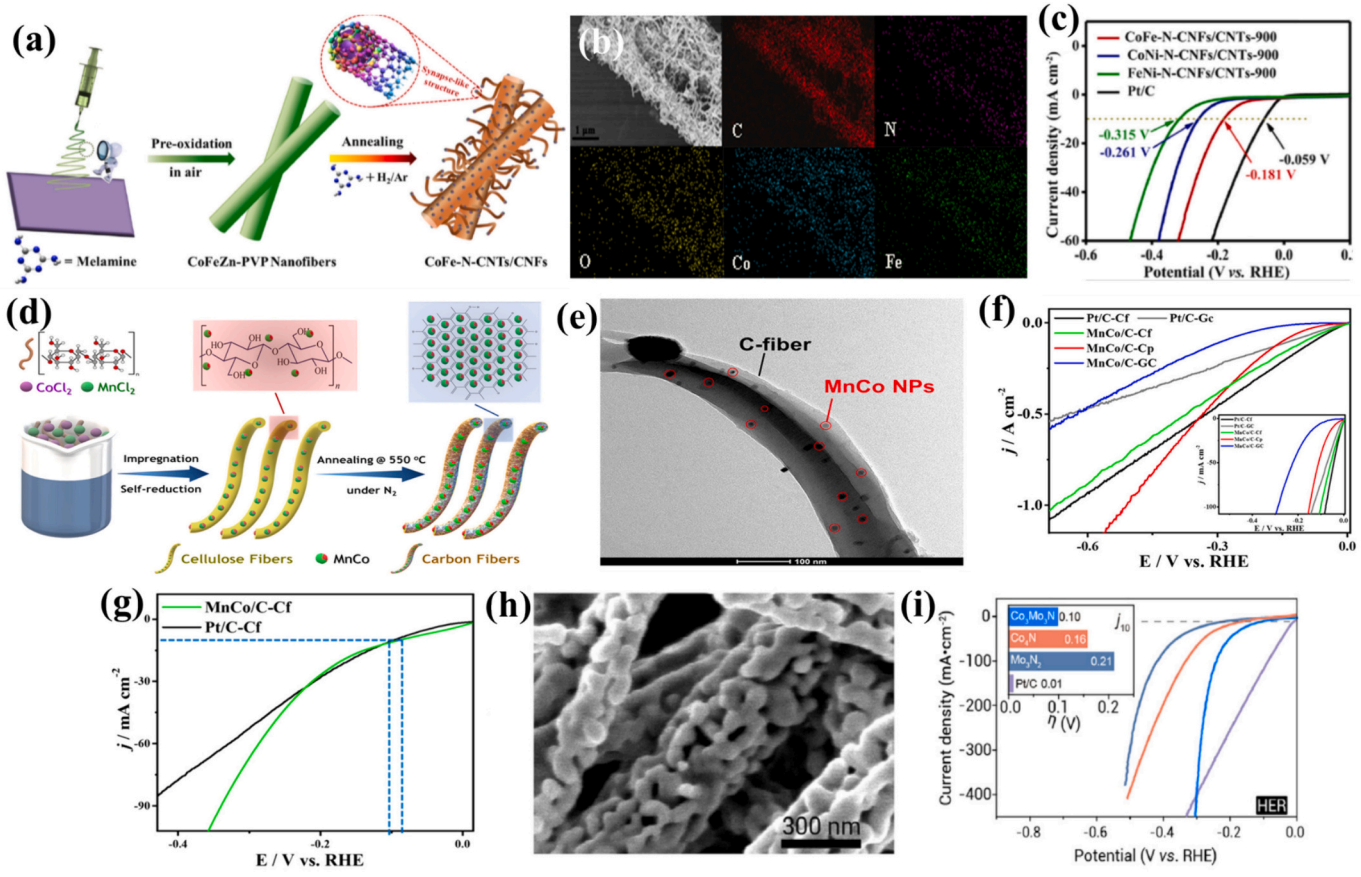

Fig. 13. (a) Synthesis process and (b) EDX elemental mapping of CoFe-N-CNTs/CNFs-900 and its (c) LSVs with other catalysts tested in 1 M KOH. Reproduced with permission from Ref. [275] Copyright 2021 Elsevier. (d) Synthesis scheme and (e) TEM image of MnCo/C fibers and its LSVs with other catalysts on different electrodes tested in (f) 0.5 M H_2SO_4. (g) LSV of MnCo/C fibers and Pt/C measured on carbon foam (CF) in 1 M KOH. Reproduced with permission from Ref. [277] Copyright 2023 ACS. (h) SEM image of $CoMoO_4$ and its (i) LSVs with other catalysts tested in 1 M KOH. Reproduced with permission from Ref. [278] Copyright 2021 Elsevier.

current for 11.1 h [275]. This is due to coupling of the synergetic and catalytic effect of CoFe and the unique physicochemical merits of N-CNTs/CNFs namely high surface area, 1D shape with shorter electron pathway, porosity with accessible active sites and quick mass transfer. This study implies the significant effect of coupling NFs with CNTs in promoting HER activity. Meanwhile, the preparation method is promising for large-scale applications with high feasibility for tailoring the composition.

Sponge-like arrays of NiCu–MOF arrays grown on GO/CC (C-NiCu–BDC-GO-CC) and formed by the hydrothermal at 200 °C for 24 h and annealing at 450 °C for 4 h under Ar showed close activity to C-NiCu–BDC-GO with η_{10} of 400 mV in 1 M KOH [276]. This indicates the significant effect of coupling two supports GO/CC, which are wired in view of their impressive electrical conductivity, as shown in the lower charge transfer resistance for C-NiCu–BDC-GO-CC relative to C-NiCu–BDC-GO [276].

Despite the noted progress in the synthesis of binary metal systems for HER, it is still a substantial challenge to explore simple and scalable synthesis methods to rationally design efficient Pt-free electrocatalysts. To this end, recently, we have synthesized MnM (M = Co, Cu, Ni, and Fe) nanoparticles in situ grown over carbon fiber (MnM/C NFs) which are derived from the cellulose via simple direct impregnation of metal salts with cellulose in water followed by annealing at 550 °C for 2 h under N_2. The cellulose with its functional groups (i.e., ether and hydroxyl) acts as a source for carbon fiber and as a reducing agent for metal salts for easing scalable production (i.e., several grams in one run) of ultra-long (5 ± 1 μM) carbon nanofibers supported small MnM nanoparticles (10–14 nm) with metal loading of 2.87 wt% (Fig. 13d, e) [277]. The HER activity was synergetic-effect-dependent, but MnCo/C loaded on carbon foam revealed the highest activity with the lowest η_{10} of 11 mV, Tafel slope 56.5 mV dec^{-1}, a hydrogen production rate of 2448 mol g^{-1} h^{-1}, and a long-term durability for 2 weeks in H_2SO_4 (Fig. 13f). Meanwhile, MnCo/C displayed a higher HER activity than Pt/C with a lower η_{10} of (88 mV) and an onset potential of 0 V in the KOH electrolyte (Fig. 13g). This study may pave the way for high-mass one-pot production of metal alloys over carbon and the replacement of Pt-group electrocatalysts. Nanorod morphology is among the most promising structures, and accordingly, the Co/Fe-MOF nanorods were obtained by the solvothermal method which promoted the HER relative to those of Co/Fe-LDH, Co-MOF, Co-OH with η_{10} of 286 mV and Tafel slope of 75 mV dec^{-1}, alongside durability for 2000 cycles, in 1 M KOH, due to bimetallic effect and using MOF support [279]. This study implies better activity using MOF support than LDH and self-standing electrocatalysts, which may open the entrance for the deployment of MOF support in HER. Porous one-dimensional Co_3Mo_3N nanorods formed via the ammonolysis of $CoMoO_4$ at 800 °C (Fig. 13h) had lower η_{10} of 100 mV and Tafel slope of 49 mV dec^{-1} than those of Co_3N and Mo_3N_2 in 1.0 M KOH besides 84 % stability after 5 h (Fig. 13i) [278]. This is ascribable to the porous nanorod shape with a short pathway for electrons and better electrolyte-electrode interaction besides the bimetallic effect. The porous nanorod morphology is highly promising for practical HER due to its ability to maintain its shape and composition during HER. Branched shapes, with their accessible active sites and stability against aggregation, are promising for the HER. Porous Ni/Cu nanodendrites prepared by the dynamic hydrogen bubble template (DHBT) method assisted by the electrodeposition of Ni over Cu-substrate enhanced the HER performance than those of Ni foam and Cu bare with η_{10} of 80 mV and Tafel slope of (123 mV dec^{-1}) in KOH electrolyte [280]. This is due to the porous dendritic morphology with high surface area, which renders Ni and Cu active sites more exposed and accessible during HER. Meanwhile, the co-deposition of Cu within Ni enriches the Ni surface by electro-active species (i.e., catalytic mediators). Although the preparation method is simple, it needs a lot of precautions, and it is not easy to scale up, and additionally, the durability of Ni/Cu nanodendrites is very low (only 2 h). The HER performance of Ni/Cu nanodendrites was superior to CoNi-OOH-30(40) η_{10} = 210 mV [281], Fe-Ni_3C-2 % η_{10} = 178 mV [282], and $NiMoO_4$-$Ni(OH)_2$/NF η_{10} = 93 mV [283]. These porous transition binary metal-based carbides, oxides, and nitrides are highly promising for the HER, but their performance is still not feasible for practical applications that require high current density and stability for several days or weeks. For the moment, their fabrication methods are still complicated with low-mass production.

5.3. Porous transition binary-metal chalcogenides for HER

Porous transition binary-metal nanostructures with chalcogenide anion (i.e., S^{2-}, Se^{2-}, Te^{2-}, and Po^{2-}) are promising electrocatalysts for HER in different electrolytes over wide pH values. This is because of their unique electron states near their Fermi levels besides electro-conductive metallic nature, durability, and low free energy for H_2 chemisorption [284,285]. $CoMo_2S_4$/Ni and $CoMoO_6$/Ni porous nanoflakes were prepared by coupling the hydrothermal and annealing followed by ion exchange reaction methods over Ni-foam support (Fig. 14a) [286]. Both $CoMo_2S_4$/Ni and $CoMoO_6$/Ni were obtained in porous foam structure composed of nanoflakes (2–5 nm), with interconnected pores (2 nm) (Fig. 14b, c), which is highly beneficial for the full water splitting. The HER activity of $CoMo_2S_4$/Ni was superior to $CoMoO_6$/Ni, including a lower η_{10} (162 mV), Tafel slope (116 mV dec^{-1}), and greater durability for 10 h (Fig. 14d–f). This is due to the synergistic effect of the Co-Mo-S bond as well as porous morphologies with abundant changes easing adsorption and diffusion of reactants with tolerance for intermediates, which enhances kinetics.

The lower charge transfer resistance is exemplified by $CoMo_2S_4$/Ni. In this context, porous Co-M-S/carbon composite (M = Mo or W) were synthesized via initial synthesis of polydopamine coated ZIF-67 nanocube (ZIF-67@PDA) through in situ polymerization followed by in situ etching and functionalization with Mo or W via mixing with acidic POM (i.e., phosphomolybdic or phosphotungstic) to form POM@ZIF-67@PDA nanocubes [287]. The obtained nanocubes were annealed at diverse temperatures and then sulfurized to yield Co–Mo–S/C-x (x = 600, 800, 1000 °C) (Fig. 14f) [287]. Porous CoMoS/C-600 nanocube and CoWS/C-800 revealed the highest HER activity with η_{10}/Tafel slope of (235 mV, 65.5 mV dec^{1}) and (240 mV, 71.13 mV dec^{-1}), respectively, besides stability for 1000 cycles (Fig. 14g, h). This is attributed to the synergistic effect, high surface area, pore volume, lower charge transfer resistance, and defect-rich Co–Mo–S or Co-W-S besides doping effect active N—C sites derived from carbonization of ZIF-67. Although this performance is very low compared to Pt/C and the obtained J_{HER} is low [287], this approach could be extended to other acidic metal precursors due to the etching and chelation effect of functional groups in ZIF-67@PDA.

$CoSe_2$-$MoSe_2$/rGO-amorphous carbon (CS-MS/rGO-C) was generated by the spray drying and subsequent selenization method (Fig. 15a), and it had a porous microsphere structure (Fig. 15b). CS-MS/rGO-C enhanced the HER activity in 0.5 M H_2SO_4 and 1 M KOH electrolytes with a η_{10} of −195 mV and − 215 mV, respectively (Fig. 15c, d), which was higher than that of CS-S/C, CS-MS/rGO, CS-MS, and $CoMO_4$ beside a lower Tafel slope, and good durability for 55 h and 1000 cycles [288]. Notably, changing the ratio of Co:Mo:Se had a significant effect on the activity, while the ratio, 1:1:3:9 was found to be optimum. The superior performance of CS-MS/rGO-C has been attributed to the deployment of two supports comprising rGO-C with their unique physicochemical and electronic properties, which enhanced the electrical conductivity and interacted more efficiently with the electrolyte, as can be seen further in the EIS data. So, using two supports is better than one support rGO or CFurther, the spray drying approach is facile, low-cost, and scalable, which could be extended for the synthesis of other porous binary or ternary metal chalcogenides. Hybrid CoSe/$MoSe_2$ hierarchical nanospheres were prepared by integration of Co and Mo into ZIF-67 via impregnation followed by carbonization and selenization at 500 °C for 6 h. The ensued material promoted the HER activity in with η_{10} of 110 mV relative to those $MoSe_2$ and CoSe in KOH electrolyte [289].

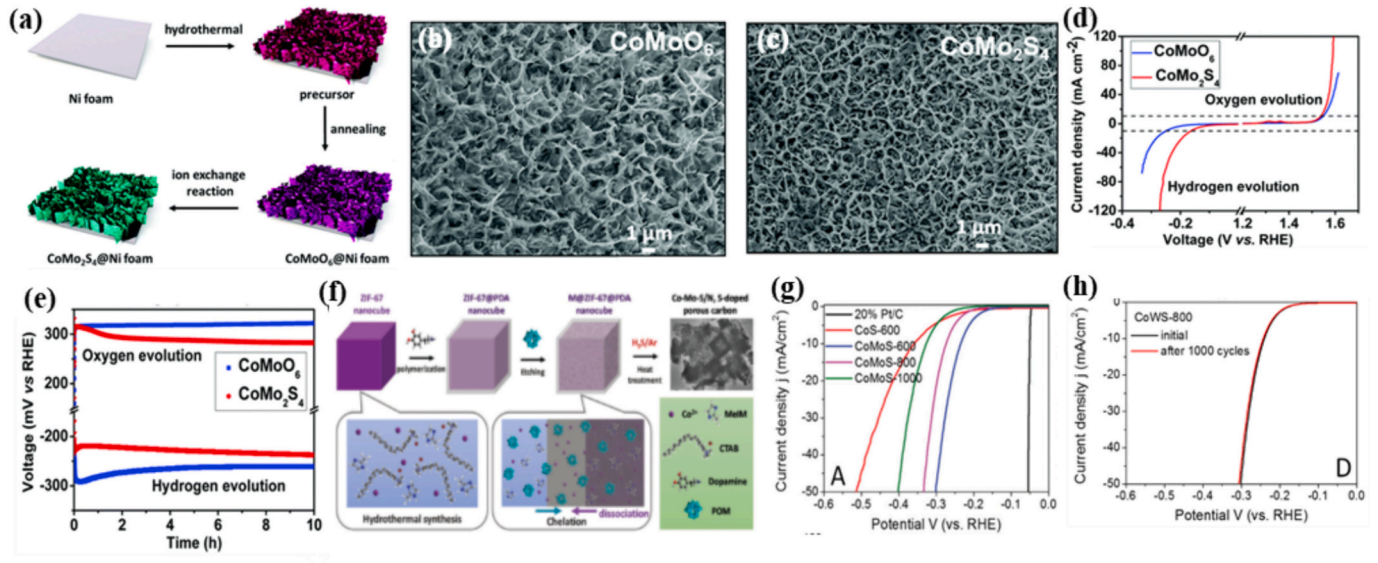

Fig. 14. (a) Scheme for the preparation process and SEM image of (b) $CoMoO_6$/Ni and (c) $CoMo_2S_4$/Ni and (d) their LSV for OER and HER process, and (e) Stability tests at 10 mA cm^{-2}. Reproduced with permission from Ref. [286] Copyright 2020 RSC. (f) Scheme for formation of Co-M-S/C-X and SEM of CoMoS-600. (g) LSV of Co-M-S/C-$_X$ tested in 0.5 M H_2SO_4, and (h) LSV of CoMoS-600 before and after 1000 CV cycles. Reproduced with permission from Ref. [287] Copyright 2022 RSC.

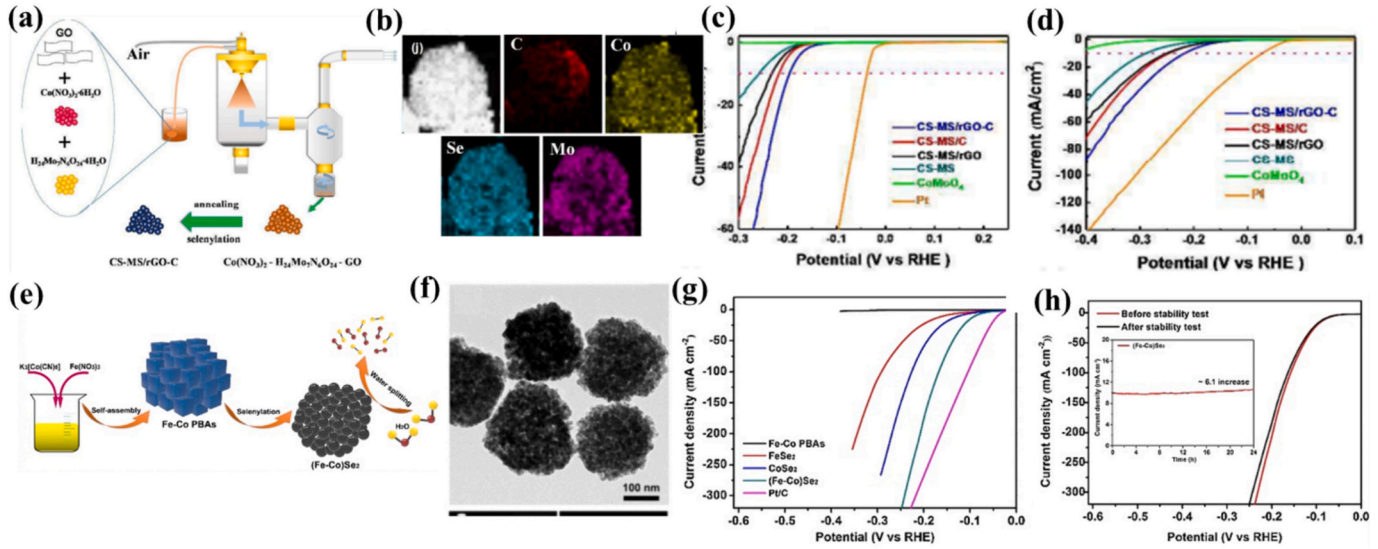

Fig. 15. (a) Preparation process and (b) STEM with elemental mapping images of CS-MS/rGO-C. LSV curves of CS-MS/rGO-C with other catalysts benchmarked in (c) 0.5 M H_2SO_4 and (d) 1 M KOH. Reproduced with permission from Ref. [288] Copyright 2018 RSC. (e) Preparation scheme and (f) TEM image of (Fe—Co)Se_2 and its (g) LSV with other catalysts tested in 1 M KOH and (n) stability of (Fe—Co)Se_2 for 24 h at 10 mA/cm^2. Reproduced with permission from Ref. [295] Copyright 2019 Elsevier.

Interestingly, CoSe/$MoSe_2$ was close to Pt/C 130 mV, besides a lower Tafel slope of 54.24 mV dec^{-1} and stability over 16 h in KOH. This is ascribed to the high surface area of CoSe/$MoSe_2$ (159.9 m^2/g), synergetic effect, porosity, and abundant active sites. CoSe/$MoSe_2$ was superior to various other electrocatalysts like Co_9S_8 –MoS_2/CNFs (η_{10} = 190 mV) [290], CoS_2 nanowires (η_{10} = 145 mV) [291], and Co–NiO/N-rGO (η_{10} = 160 mV) [292]. However, the role of carbon derived from the carbonization of MOF has not been delineated, which could be one of the main reasons responsible for promoting the HER activity of CoSe/$MoSe_2$. The HER activity of WS_2/$Co_{1-x}S$/ porous carbon *co*-doped with N and S (xWZ-y) derived from polyoxometallate@ZIFs (ZIF = Zeolitic imidazolate) via the hydrothermal method followed by annealing at temperatures (y = 600, 800 and 1000 °C and x = Co/W ratio) under Ar and then under H_2S depended on the both y and x [293]. 20WZ-800 was found to be optimum with a η_{10} = 221 mV and Tafel slope of 83 mV dec^{-1} in 0.5 M H_2SO_4. The performance of 20WZ-800 is attributed to the enriched active sites and enhanced mass transport between H^+_{ads} and the electrodes derived from modulating the electronic structure and charge density of C by N/S dopant. However, 20WZ-800 showed a lower durability (12 % activity loss) after 8000 s, which may be attributed to the detachment of metal active sites or aggregation.

Likewise, the HER performance of Fe—Mo sulfide/carbon nanocomposites (xMo@MIL-y) derived from phosphomolybdic acid encapsulated MOF via hydrothermal synthesis at 130 °C followed by chemical vapor sulfurization depended on the different Mo content (x = 150, 250, and 350 mg) and temperatures (y = 600, 800, and 1000 °C). Here, the 1Mo@MIL-800 was found to be optimum with a η_{10} of 321mVbesids lower Tafel slope of 62 mV dec^{-1} in 0.5 M H_2SO_4 [294]. This is due to

the higher metal-active sites and their well-dispersed nature besides the doping effect. However, the durability of 1Mo@MIL-800 was insufficient, with only 1000° cycles and 800 s and notably it showed poor HER activity in 1 M KOH electrolyte and 0.5 M Na_2SO_4 electrolyte. (Fe—Co)Se_2 was synthesized via self-assembly of Prussian blue analogs as precursors, followed by a post-selenization process at 400 °C (Fig. 15e). It had a nanocube structure assembled in a porous spherical-like structure (Fig. 15f) with a surface area 103.5 m^2/g and pore size 0.193 cm^3/g [295]. The HER activity of (Fe—Co)Se_2 was superior to $CoSe_2$, $FeSe_2$ Fe-Co-Prussian blue analogs with η_{10} of 90 mV (Fig. 15g) and lower Tafel slope of 58.7 mV dec^{-1} in 1 M KOH besides durability for 2000 CV cycles, and 6.1 % activity loss after 24 h (Fig. 15h). This activity is higher than those of previously reported binary metal chalcogenide, in view of its porous structure, high surface area, and synergism of (Fe—Co)Se_2. (Fe—Co)Se_2 was more active than those of various binary systems like Ni_3Se_2 nanoforest/Ni, ($\eta_{10=}$ 203 mV) [296], (Ni, Co)Se_2-GA ($\eta_{10=}$ 128 mV) [297], among others.

Ni_3S_2/MoS_2 hollow spheres were prepared via solvothermal method at 180 °C followed by sulfidation at 550 °C. The ensued product showed η_{10} of 166 mV and Tafel slope of 78.2 mV dec^{-1}, which outperformed NiMo-MOF and bare Ni_3S_2 in 1 M KOH [298]. Notably, Ni_3S_2/MoS_2 was stable for 100 h with ~13.1 % current attenuation due to the bimetallic heterostructure, large surface area, and porosity with more exposed metal active sites. Owing to these merits, Ni_3S_2/MoS_2 was superior to MoS_2/NiCoS (η_{10} = 189 mV) [208], Ni_3S_2/NiS/NOSCs (η_{10} = 180 mV) [299], and $CoSe_2/MoSe_2$ (η_{10} = 168 mV) [300]. Moreover, Ni_3S_2/MoS_2 maintained its crystallinity, electronic structure properties, and composition. Although the lower η_{10}, the durability is not up to the level of commercial scale, and various analysis need to be conducted to confirm structural changes after the durability tests. The HER performance of MoS_2–Ni_3S_2 nanoflake grown on 3D Ni foam and formed by hydrothermal method at 200 °C was higher than those of MoS_2, Ni foam, Ni_3S_2, and MoS_2–Ni with η_{10} of 125 mV in 1 M KOH beside durability for 50 h [301]. This is ascribed to higher electrical conductivity derived from 3D interconnected porous heterostructures, bimetallic structure, and super hydrophilic surface, which enhances the usage of metal active sites with increased interaction with electrolytes. MoS_2–Ni_3S_2 with its lower η_{10} is promising, but the durability is very low. The HER activity of Fe-Ni-S film interwoven nanosheets deposited on 3D nickel foam by electrodeposition assisted in the presence of liquid crystal template (LCT) depended on Fe/Ni ratio, but Fe-Ni-S with a ratio of 3/1 was found to be the best with a lower η_{10} as 47 mV and Tafel slope of 178 mV dec^{-1} in 1.0 M KOH [302]. Notably, the electrodeposition in water without LCT, the Fe-Ni-S had η_{10} of 77 mV. This indicates the significant effect of LCT on the realization of porous morphology, however, the stability was only conducted for 500 cycles and 1000 s. The aforementioned porous morphologies (i.e., nanocubes, nanospheres, and nanosheets) provide a longer path for the charge transfer during HER, so their performance and durability are still inadequate. Porous one-dimensional nanostructures are imminent with their ability to provide short paths for electrons and charge transfer besides durability against aggregation, but they have been rarely reported. The porous $NiCo_2S_4$ NS/CC nanowires composed

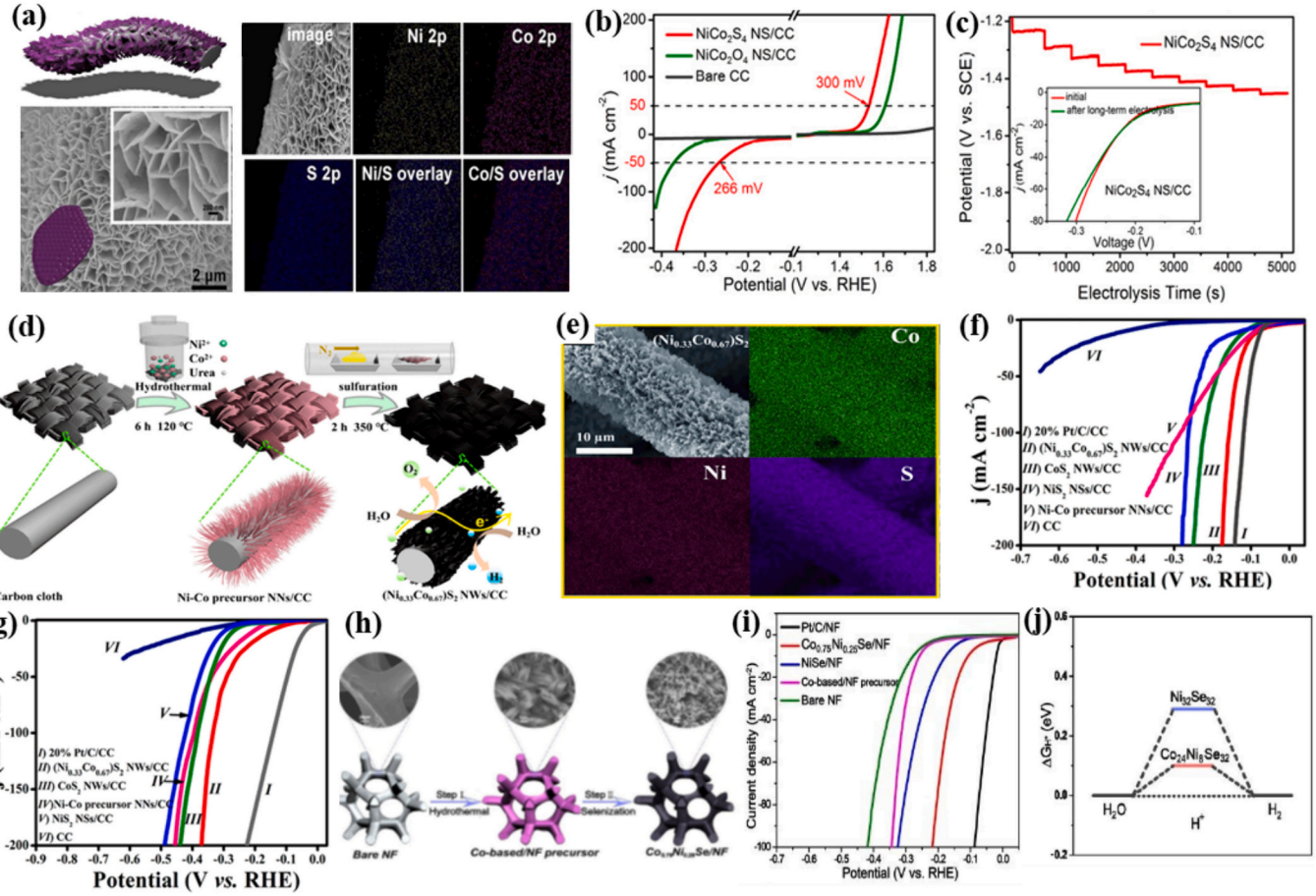

Fig. 16. (a) SEM and elemental mapping of $NiCo_2S_4$ NS/CC nanowires, (b) polarization curves of $NiCo_2S_4$ NS/CC nanowires relative to its counterparts, and (d) CA test of $NiCo_2S_4$ NS/CC nanowires in 1.0 M KOH. Reproduced with permission from Ref [303]. Copyright 2018 ACS. (d) the preparation process, (e) SEM and elemental mapping of $(Ni_{0.33}Co_{0.67})S_2$ NWs/CC and its LSV with other catalysts tested in (f) 0.5 M H_2SO_4, (g) 1.0 M KOH. Reproduced with permission from Ref. [306] Copyright 2018 ACS. (h) Preparation process of $Co_{0.75}Ni_{0.25}Se$/NF and its (i) LSV with other catalysts tested in 1.0 M KOH. (j) HER free energy for the $Co_{24}Ni_8Se_{32}$ and $Ni_{32}Se_{32}$. Reproduced with permission from Ref. [311] Copyright 2019 RSC.

of porous nanosheets (NS) arrays with rough surfaces within a thickness of 1.64 μm were grown on carbon fiber cloth sheet nanofibers (CC) (Fig. 16a) were synthesized by anion exchange via a hydrothermal process 100 °C and 150 °C followed by a wet-chemistry topotactic conversion of Ni/Co precursors [303]. The nanosheet comprised of rough, closely connected nanospheres with a thickness 25.2 nm and height 1.64 μm, and had a high BET surface area 88.324 m^2/g, and an average pore volume/pore radius (0.228 mLg^{-1} /1.818 nm). The HER performance of $NiCo_2S_4$ NS/CC was higher than $NiCo_2O_4$ NS/CC with η_{10} of 181 mV and Tafel slope of 130.5 mV dec^{-1} in KOH (Fig. 16b), besides durability for 5000 s (Fig. 16c). This is due to the high surface area (88.324 m^2/g), pore volume (0.228 mL/g), rich redox properties, spinel structure, nanoporous with open-shelled nanosheets with rich exposed active sites. The one-dimensional shape which accelerates the diffusion and charge mobility, assisted $NiCo_2S_4$ NS/CC to outperform others with lower η_{10} like Ni_3S_2/Ni foam 223 mV [304], $NiCo_2S_4$/Ni foam 210 mV [212], CoS_2/Carbon cloth 193 mV [305], and CNTs@Co-S/Carbon paper 190 mV [264]. Notably, $(Ni_{0.33}Co_{0.67})S_2$ nanowires grown on CC $(Ni_{0.33}Co_{0.67})S_2$ and the synthesis of NWs/CC via hydrothermal method at 120 °C coupled with sulfuration at varying temperatures (Fig. 16d). The ensued product had porous honeycomb-like network with pore average size (9.1 nm) (Fig. 16e) enhanced the HER activity relative to NiS_2 NSs/CC and CoS_2 NWs/CC in H_2SO_4 and 1.0 M KOH electrolytes. The HER activity depended on the hydrothermal temperature where $(Ni_{0.33}Co_{0.67})S_2$ NWs/CC obtained at 350 °C was found to be optimum with η_{10}/Tafel slope of 81 mV/60 mV dec^{-1} in H_2SO_4 relative to KOH electrolyte $\eta_{10=}$156 mV/127 mV dec^{-1} (Fig. 16d–g) as well as the durability for 2000 cycles and 24 h with 22 % and 19 % activity loss activity [306]. $(Ni_{0.33}Co_{0.67})S_2$ NWs/CC was superior to previously reported $Mn_{0.05}Co_{0.95}Se_2$/glassy carbon ($\eta_{10=}$ 218 mV) [307], NiS_2/MoS_2/CC ($\eta_{10=}$ 241 mV) [308], $Fe_{1-x}Co_xS_2$/graphene ($\eta_{10=}$ 241 mV) [309], and $CoS_{2x}Se_{2(1-x)}$/CC ($\eta_{10=}$ 129 mV) [310] in H_2SO_4.

Similarly, the HER activity of porous NiMoS NWs/NF prepared by electroplating followed by hydrothermal at 180 °C was higher than NF with η_{10} of 79 mV and Tafel slope of 103 mV dec^{-1} with stability for 13 h and 1000 cycles in KOH [312]. This implies the effect of porous nanowire structure and deployment of CC, which was preferred over glassy carbon and graphene working electrodes; thus, other working electrodes could also be explored for promoting the HER. Likewise, porous NiFeSe nanocube deposited on carbon fiber paper (NiFeSe/CFP) were obtained via the electrodeposition protocol followed by a facile selenization at 450 °C. The ensued product enhanced the HER activity relative to NiFe PBA/CFP and FeSe/CFP with η_{10} of 186 mV and Tafel slope of 52 mV dec^{-1} in KOH and durability for 20 h [313]. The HER activity of $Co_{0.75}Ni_{0.25}Se$/NF nanorods, grown on porous nickel foam (NF) by two-step hydrothermal process at 160 °C (Fig. 16h) [311], enhanced the HER relative to NiSe/NF, Co-based/NF precursor, and bare NF with η_{10} of 106 mV and Tafel slope of 58 mV dec^{-1} besides durability for 16 h in 1.0 M KOH (Fig. 16i). Moreover, $Co_{0.75}Ni_{0.25}Se$/NF showed lower H_2O adsorption energy and lower Gibbs free-energy (ΔGH*) for intermediates than $Ni_{32}Se_{32}$, suggesting quick HER kinetics as confirmed by the DFT (Fig. 16j). This is due to the synergism of Co/Ni and its one-dimensional structure, which has abundant active sites and higher conductivity. The $NiCo_2X_4$/CP (X = O, S, and Se) grown on carbon paper (CP) was generated by solvothermal method at 120 °C followed by oxidation, sulfidation, or selenidation treatments at 450 °C. It enhanced the HER activity, as $NiCo_2Se_4$/CP was found to be optimum with η_{10} of 56 mV and Tafel slope of (51.8 mV dec^{-1}) besides durability for 20 h in KOH [314]. This is due to the η_{10} higher surface area in addition to Se/S substitution, which increases the electron density around the metal atoms, as confirmed by the DFT. $NiCo_{2S}e_4$, with its special monoclinic phase, possesses more unoccupied orbitals near the Fermi energy level relative to $NiCo_2S_4$ and $NiCo_2O_4$, thus leading to the ease of H_2O/OH^- species absorption and accelerating the HER kinetics.

5.4. Porous transition binary-metal phosphides for HER electrocatalysis

Porous binary transitions metal phosphide have emerged as a promising class of advanced electrocatalysts, especially for the HER, with uniqueness attributed to their physical and chemical properties, making them an efficient and cost-effective alternative to noble metals. Porous Co-MoP-x nanotubes were obtained by the precipitation and phosphatization under varying temperatures (x = 500–800 °C in Ar with NaH_2PO_2), and the temperature had a noted effect on the HER performance [277]. However, CoMoP-600 was adjudged to be the best with a lower η_{10} of 220 mV and higher TOF (2.0 s^{-1}) compared to CoMoP-500, CoMoP-700, and CoMoP-800 in 0.5 M H_2SO_4 [315]. This possibly emanates from the nanotube structures with larger specific surface area and short electron path during HER along with bimetallic effect with P heteroatom thus indicating the substantial effect of porous one-dimensional shapes on promoting the HER activity. The amorphous $CoMoP_x$ nanosheets arrays grown on carbon fiber paper (a-$CoMoP_x$/CF) were produced through the hydrothermal treatment (at 100 °C for 3 h) and phosphidation (at 300 °C for 1 h with NaH_2PO_2) (Fig. 17a, b) [316]. The resulting a-CoMoPx/CF displayed outstanding HER activity in 1.0 M KOH at a low η_{10} of 59 mV, surpassing the performance of CoP_x/CF and MoP/CF (Fig. 17c). The higher TOF of 3.38 s^{-1} and maintained current stability or 50 h has been attributed to its unique hierarchical coupling properties of nanosheets arrays and carbon fiber with abundant defects. Additionally, the presence of nanosheets of CoMoPx on carbon fibers with a high electron conductivity facilitate the tolerance of the hydrogen adsorption energy as evidenced by the DFT. Thus, a-CoMoPx/CF had a lowest ΔGH* (Figs. 17d). Hollow FeP nanospheres doped with transition metals (Mn, Co, and Ni) were synthesized using solvothermal methods (at 120 °C for 1 h) followed by phosphorization (at 300 °C for 3 h in N_2) which enhanced the HER due to the doping effect. Among these, Co-FeP with a larger surface area, enhanced charge transfer, and optimized chemical state resulted in superior HER activity at a lower η_{10} of 126 mV compared to Ni-FeP, Mn-FeP, and FeP [319]. This indicates the privileged usage of Co-dopant in promoting the HER performance of FeP. The porous heterojunction CoP_4/FeP_4 nanocage was prepared through co-precipitation for 24 h followed by phosphate calcination (at 400 °C for 2 h in Ar with NaH_2PO_2). It facilitated the rapid electron transport leading to higher HER activity at a lower η_{10} of 265 mV in comparison to FeP_4 and NF [320]. This is possibly attributable to the synergism of FeP/Co and nanocage shape with accessible metal sites and stabilized inner core against dissolution or aggregation. The direct growth of porous nanosheets Co—Fe PBAs on Ni-foam (Fe-CoP/NF) via chemical reduction and phosphorization (at 400 °C for 3 h in N_2 with NaH_2PO_2) has been accomplished. The ensued product demonstrated remarkable HER activity in 1.0 M KOH at lower η_{10} of 78 mV and a higher compared to $CoFe_2O_4$/NF, besides excellent stability for 30 h [321]. This superior performance can be attributed to the porous nanosheet architectures and NF, which provide abundant active sites, facilitating high electrolyte contact and tolerating the adsorption of intermediates or products. This study boosts the importance of using metal-foam support for enhancement of the HER performance.

Likewise, porous FeCo-MOF)-based phosphide (MOF CoFeP) nanoarrays were fabricated on NF through a hydrothermal process (at 90 °C for 24 h) followed by phosphorization (at 350 °C for 2 h in N_2 with NaH_2PO_2) of CoPBA [322]. The resulting MOF CoFeP material, composed of hollow nanosheets, exhibited superior HER activity at a low η_{10} of 200 mV relative to MOF CoFeO, MOF CoFe, MOF Fe, and MOF Co, along with excellent stability over 30 h and high TOF of 1.61 s^{-1}. This improved performance has been attributed to the hierarchical 3D MOF structure, which enhances the physical incorporation of metals, promotes charge transfer, and improves electronic effects.

Hydrothermal treatment at 180 °C for 6 h and phosphidation at 350 °C for 3 h in a nitrogen environment with NaH_2PO_2 have been investigated as methods to synthesize $Co_{0.7}Fe_{0.3}P$@C composed of spherical $Co_{0.7}Fe_{0.3}P$ structure on a carbon nanowire for promoting

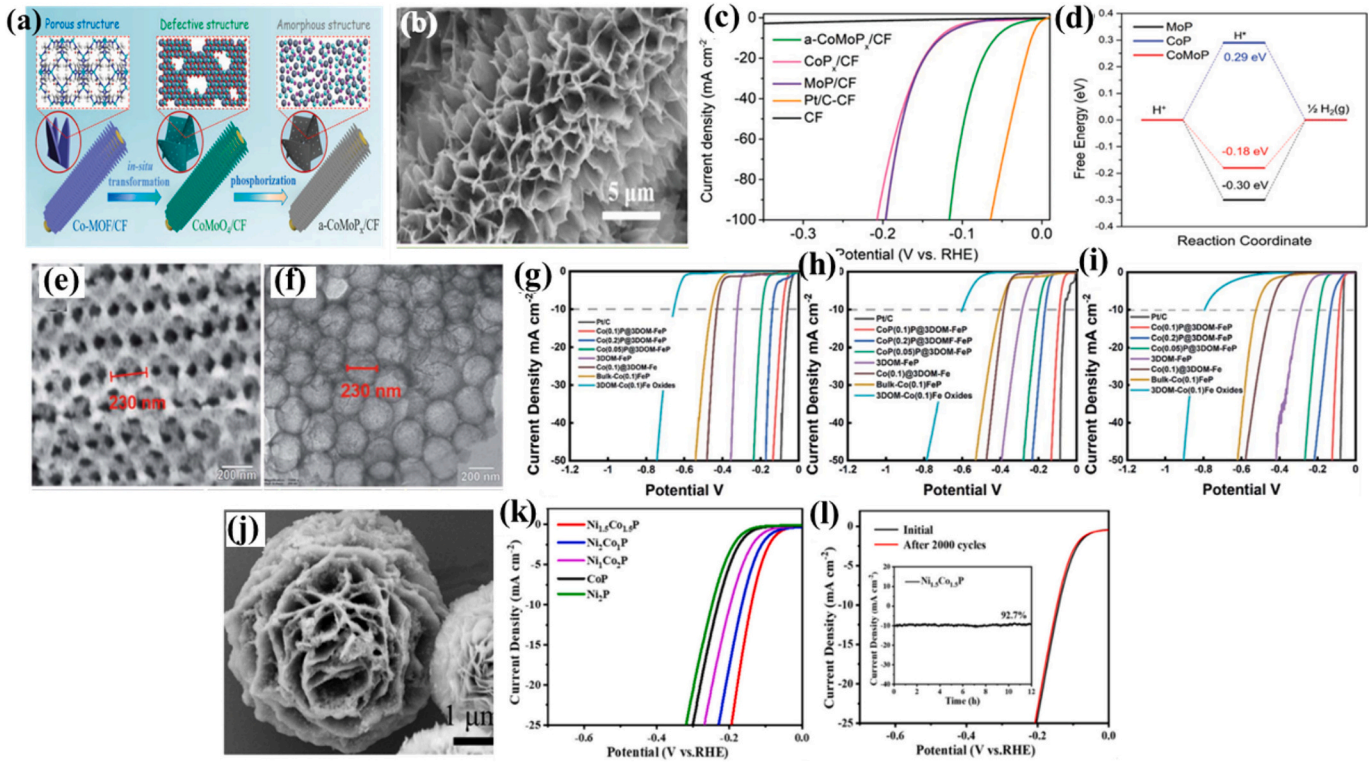

Fig. 17. (a) Preparation schematic and (b) SEM image of a-CoMoP$_x$/CF. (c) LSV curves of a-CoMoP$_x$/CF with others in 1.0 M KOH and their (d) Gibb's free energy. Reproduced with permission from Ref. [316]. Copyright 2020 Wiley-VCH. (e) SEM and (f) TEM image of Co(0.1)P@3DOM-FeP. LSV curves of Co(0.1)P@3DOM-FeP with others tested in (g) 1.0 M KOH, (h) 1.0 M PBS and (i) 0.5 M H_2SO_4. Reproduced with permission from Ref. [317] Copyright 2021 RSC. (j) SEM image of $Ni_{1.5}Co_{1.5}P$/MFs. (k) LSV curves of $Ni_{1.5}Co_{1.5}P$/MFs with others tested in 1.0 M KOH, and (l) HER stability of $Ni_{1.5}Co_{1.5}P$/MFs. Reproduced with permission from Ref. [318] Copyright 2021 Elsevier.

alkaline HER [323]. $FeCoP_2$ nanospheres grown on hierarchical worm-like N/P co-doped porous carbon ($FeCoP_2$@NPPC) were fabricated by sol-gel process for 12 h followed by carbonization at 900 °C for 3 h. The porosity and binary metal effect with the NPPC support facilitated efficient electron transport, increased active site contact area, and improved wetting properties along with reducing ΔGH* of $FeCoP_2$@NPPC. This had the highest HER activity at low η_{10} of 114 mV 0.5 M H_2SO_4 and 150 mV in 1.0 M KOH compared to CoP@NPPC and FeP@NPPC [324]. Thus, Fe-doped VP on porous carbon encompassing NF (Fe_xV_y-PC/NF) delivered higher HER activity in 1.0 M KOH at η_{10} of 66 mV and excellent stability for 5000 cycles [325]. Meanwhile, multiphases doped 3Mn-NiP demonstrated better HER activity in 1.0 M KOH at a lower η_{10} (77 mV), but a higher η_{10} (164 mV) in 0.5 M H_2SO_4 relative to Ni_2Mn_1P in a previous study [326]. These investigations indicate the preferential effect of doped support on the enhancement of the HER performance of $FeCoP_2$. In this context, CoFeP nanospheres supported on N-doped porous carbon (CoFeP-NC) were synthesized in-situ through a combination of hydrothermal treatment at 200 °C for 12 h and phosphorization at 400 °C for 3 h with NaH_2PO_2. The ensued product had a higher HER activity relative to FeP-NC and CoFe-NC [327]. CoFeP-NC exhibited a lower η_{10} of 81 mV in 0.5 M H_2SO_4 and 173 mV in 1 M KOH, attributed to the synergistic effects of CoFeP and its dispersion on porous NC with abundant active sites, enhanced electronic conductivity, which accelerated the electrolyte access.

A range of CoM_xP 0D quantum dots grown on carbon cloth (CC) catalysts (where M = Fe, Mn, and Ni; x = 0, 0.05, 0.2, 0.5, and 1.0) were prepared through ion-exchange and phosphorization of ZIF-67/CC at 350 °C for 4 h with NaH_2PO_2. They had a noticeable HER activity that depended on the M and x [328]. However, $CoFe_{0.05}P$/CC exhibited highest HER activity with low η_{10} of 73/85 mV in acidic/alkaline along with higher TOF and stable current density for 45 h compared to $CoMn_{0.05}P$/CC and $CoNi_{0.05}P$/CC. Moreover, $CoFe_{0.05}P$/CC induced the efficient HER in alkaline simulated seawater, which is important for large-scale appliances. The superior HER activity of $CoFe_{0.05}P$/CC originated from coupling properties of 0D quantum dots (i.e., quantum effect, high surface area, and accessible active sites) and physiochemical merits of CC, which decreased the ΔGH* and ease of desorption of hydrogen during HER as confirmed by the DFT.

Co-Fe-P nanoparticles grown on NF (Co-Fe-P/NF) and synthesized using Prussian blue as a template by the hydrothermal treatment at 120 °C for 5 h and phosphorization at 350 °C for 2 h under NH_3 with a NaH_2PO_2 and assessed for the alkaline HER [329]. Paper ball shape of Co-Fe-P/NF had the highest activity with a lower η_{10} of 115.6 mV compared with FeP/NF, CoP/NF, and NF in 1 M KOH due to porous NF support and bimetallic effect with exposed active sites, which enhanced the electrolyte-electrode interaction and reduced the charge transfer resistance during the HER; Co-Fe-P/NF had the lowest R_{ct} (1.89 Ω) compared with its counterparts. CoP grown on 3D-ordered mesoporous FeP (CoP@3DOM-FeP) were produced through a combination of sol-gel and phosphorus chemical vapor deposition techniques at 480 °C using Fe-EG/Co-PS, which consist of ZIF-67 and polystyrene nanospheres template [317]. The resulting $Co_{(0.1)}$P@3DOM-FeP displayed a spatial interconnected mesoporous structure (Fig. 17e, f), which displayed a higher HER performance at η_{10} of 67.2 mV in 1 M KOH, 71.1 mV in 0.5 M PBS and 76.5 mV in 0.5 H_2SO_4 comparable to Pt/C (Fig. 17g–i). This is derived from the interconnected pores with abundant channels that ease the adsorption of reactants, mass transfer, and desorption of intermediates and products, besides enhancing the electrical conductivity.

3D nanoporous spongy-like NiCoP nanospheres with tunable Ni/Co ratio were obtained through chemical reduction, phosphorization (300 °C for 1 h in Ar with NaH_2PO_2), and etching in 0.1 M HCl. The ensued product had HER performance that was depended on the ratio of Ni/Co. However, $Ni_{0.2}Co_{0.8}P$ improved the HER activity with a low η_{10} of 116/237 mV in 0.5 M H_2SO_4/0.1 M KOH compared to $Ni_{0.4}Co_{0.6}P$,

$Ni_{0.6}Co_{0.4}P$, and $Ni_{0.8}Co_{0.2}P$, CoP and Ni_2P, respectively [330]. This is owing to optimal synergistic effect, higher surface area, and sponge-like nanospheres with accessible active sites.

Ultrathin porous NiCoP nanosheets (NSs) were fabricated through microwave irradiation (700 W for 15 min) followed by phosphorization (300 °C for 3 h in Ar with NaH_2PO_2). They exhibited remarkable HER performance at a lower η_{10} of 105 mV compared to Ni_2P, and CoP, besides stability over 20 h in 1.0 M KOH [330]. This is being attributed to the activity-structure relationship of NiCoP, stemming from its crystalline structure, large surface area, P-rich surface, abundant defect density, and numerous active sites. Similarly, ultrathin $NiCoO_x$ nanosheets with varying thicknesses have been synthesized through solvothermal (60 °C for 3 h) and phosphorization (400 °C for 2 h with NaH_2PO_2) methods, and their HER activity depended on the thickness that could be delicately adjusted by pH (7.8–8.5) [331]. However, NiCoP-8.0 (pH = 8) was found to the best with a lower η_{10} of 34.3 mV and higher HER rate of 238.2 mmol/h g^{-1} in 1 MKOH relative to its NiCoP-7.8, NiCoP-8.0, NiCoP-8.3, and NiCoP-8.5 in addition to 92.3 % current retention after a 20 h. This study delineates the thickness structure and HER activity relationship of $NiCoO_x$ nanosheets.

Ultrathin Ni-CoP with tunable P content were achieved by chemical reduction and phosphorization (300 °C for 2 h with NaH_2PO_2) of Ni-Co (OH). They had HER activity which depended on the P-content [332]. However, Ni-CoP-5 % delivered superb HER activity at a lower η_{10} of 88 mV than those of Ni-CoP-10 %, Ni-CoP-1 %, and bare CoP in 1.0 M besides stability after 5000 cycles [332]. This is because of rich Co-vacancies, interconnected porous architectures, and ultrathin nanosheets with abundant in-plane pores, which optimized Δ H* as established by DFT calculations. Likewise, Ni_2P/CoP nanosheets grown on an NF substrate through the electrodeposition at 10–40 min followed by phosphorization (350 °C for 1 h in N_2 with NaH_2PO_2. The ensued product had HER activity that was depended on the electrodeposition times [333]. However, Ni_2P/CoP-40 formed at a higher time improved the HER activity with the lowest η_{10} of 65.2 mV in 1.0 M PBS and 87.8 mV in 1.0 M KOH, compared to other samples. This was attributed to the great synergism, enhanced wettability, and reduced contact angle with the electrolyte, which accelerated the charge transfer kinetics. 3D $Ni_{0.5}Co_{0.5}P$ nanostructure were prepared via hydrothermal treatment of $NiCo(CO_3)(OH)_2$ (90 °C for 8 h) and phosphorization (250–350 °C for 2 h in Ar with NaH_2PO_2). It had higher HER activity with a lower η_{10} of 87 mV compared to CoP-300 and Ni_2P-300 [333]. In addition to attributes of a higher exchange current density and stability, the synergistic effect of Co and Ni that improved conductivity, electrochemical active surface area, and exposed active sites, as well as the unique 3D hierarchical urchin-like structure facilitated the mass transport and charge transfer.

3D self-assembled nanoflowers of Ni_xCo_yP/MFs with controlled Ni/Co ratios were fabricated by hydrothermal method (180 °C, 12 h) and phosphorization (350 °C, 2.5 h in N_2 with NaH_2PO_2) of $NiCo_2O_4$ and tested for alkaline HER (**Fig. 17j**) [318]. Here, $Ni_{1.5}Co_{1.5}P$/MFs exhibited the best HER activity with a smaller η_{10} of 141 mV relative to those Ni_2Co_1P/MFs, Ni_1Co_2P/MFs, CoS, and Ni_2S in 1 M KOH in addition to 92.7 % current retention after 12 h (**Fig. 17k, l**). This possibly emanates from the nanoflowers' morphology with exposed active sites and stable core against aggregation, which enhanced the accessibility of metal active sites and stabilized them, in addition to enhanced electrolyte interaction. Thus, the $Ni_{1.5}Co_{1.5}P$/MFs had the lowest R_{ct} of 15 Ω, compared to its counterparts. Ultra-small 3D porous NiCoP nanosheets anchored on NF (NiCoP/NF) were synthesized by hydrothermal protocol (120 °C, 5 h) and phosphorization (350 °C, 2 h in N_2 with NaH_2PO_2). It exhibited an outstanding HER performance with a low η_{10} of 58 mV and higher durability [334]. CoNiP grown on NF and N-enriched holey carbon layers derived from CoNi ZIF-8 template (CoNiP@CN/NF) were formed by the electrodeposition and phosphorization (600 °C, 2 h in N_2 with NaH_2PO_2) and assessed for enhanced HER. CoNiP@CN/NF had a low η_{10} of 87 mV and Rct of ~0.2 Ω relative to its counterparts in 1.0 M KOH [335]. This is attributed to the high conductivity of NC and rich active sites besides synergism with CoNiP, which indicate the privilege of using two supports, NF with NC, for enhancement of the HER, owing to their combined unique physicochemical merits. Other supported porous binary electrocatalysts enhanced the HER as well, like Co_xP_y/Ni_xP_y-NPC at η_{10} of 126 mV in 1.0 M KOH [336], Ni-Co-P@CSs micro-carbon spheres at η_{10} of 57 mV in 0.1 M KOH [337], and Ni_2P/CoN-PCP at η_{10} of 94 mV in 1.0 M KOH [338]. Ni-Co-P microflowers were formed via both the solvothermal and hydrothermal processes (Ni-Co-P-H) and exhibited higher HER activity in 0.5 M H_2SO_4, 0.5 M PBS, and 1.0 M KOH at η_{10} of 90, 157, 121 mV, respectively besides durability for 24 h relative to the sample obtained with solvothermal method only [339]. This is due to the porous flower-like shape with accessible active sites, which indicates the effect of the preparation method on promoting the HER activity. A series of flower-like nanostructures were prepared for an increment of the HER-like $(NixFe_{1-x})_2P$/porous graphitized carbon films at η_{10} of 118 mV in 1.0 M KOH [340], Ni_1Fe_1P-MOF at η_{10} of 154 mV in KOH [341], and MoP/Ni2P/NF at η_{10} of 75 mV in KOH [342]. These catalysts displayed lower durability, and their activities were still far from the replacement of Pt/C. NiCoP-CoP nanowires were grown directly on a hierarchical porous NF (NiCoP-CoP/Ni/NF) (Fig. 18a) achieved through the electrodeposition, hydrothermal treatment (120 °C for 8 h), and phosphorization (350 °C for 2 h in N_2 with NaH_2PO_2) of a NiCo precursor/Ni/NF [343]. The resulting NiCoP-CoP/Ni/NF demonstrated exceptional HER activity at a low η_{10} (49 mV) compared with NiCoP-CoP/NF, NiCo salt/Ni/NF, Ni/NF, NiCoslat/NF, and NF beside durability for 50 h in 1.0 M KOH (Fig. 18b, c). This is due to the coupling merits of Ni/NF supports with nanowire shape, which enhanced the electrical conductivity and increased the interaction with the electrolytes. Thus, NiCoP-CoP/Ni/NF had the lowest R_{ct} relative to its counterparts.

Porous $Ti_3C_2T_x$ monolayers, anchored with NiCoP nanoclusters (P-$Ti_3C_2T_x$@NiCoP) were formed by initial synthesis of $Ti_3C_2T_x$ by LiF + HCl etching followed by solvothermal treatment and phosphorization. The ensued material had higher HER activity than $Ti_3C_2T_x$@NiCoP and NiCoP at a low η_{10} of 115/101 mV 0.5 M H_2SO_4/1.0 M KOH [347]. The superior performance of P-$Ti_3C_2T_x$@NiCoP has been attributed to the coupling properties of $Ti_3C_2T_x$ (i.e., high electrical conductivity, abundant metal sites, and defects) with the catalytic merits of NiCoP. This study raises the possibility of using $Ti_3C_2T_x$ as a support for binary metal supplied to enhance the HER. FeNiP nanospheres incorporated into N, P-codoped carbon nanosheets (FeNiP/NPCSs) were formed by the carbonization-phosphorization (at 1000 °C for 2 h in nitrogen) (Fig. 18d) and assessed for electrocatalytic HER activity [344]. FeNiP/NPCSs outperformed FeNiP/NPC and FeNi/NCS with a lower η_{10} of 181/126 mV in 1.0 M KOH/0.5 M H_2SO_4 besides stability after 12 h (**Fig. 18e**). This possibly emanates from the coupling properties of NPCs (i.e., impressive electrical conductivity and higher interaction with electrolytes) and the synergism of FeNiP. Since the ratio of FeNiP could show better activity, 3D honeycomb-like porous carbon nanostructure supported FeNiP nanoparticles $Fe_xNi_{2-x}P$/PC (where $0 < x > 2$) were assessed which had HER activity depended on Fe/Ni ratio, where $Fe_{0.5}Ni_{1.5}P$/PC was found to be the best with a lower η_{10} of 200 mV in 1.0 M KOH alongside durability for 16 h [348]. The enhanced performance is ascribed to the well distribution of spherical $Fe_{0.5}Ni_{1.5}P$ on 3D honeycomb structure with highly conductive and optimized active sites. Fe_2P heterojunction nanosheets (HS) grown on Ni_2P foam (Ni_2P/Fe_2P HS/NF) were obtained through the hydrothermal process, and phosphorization and they outperformed Pt/C with a low η_{10} of 64 mV besides a higher HER rate of 0.18 mmol/h and stability for 100 h in 1 M KOH [349]. This is due to the heterointerfaces and interaction with the support, which tune the adsorption energy of reactants and intermediates, as further confirmed by the DFT. This interaction also stabilizes the Ni_2P against aggregation or dissolution during the HER. Porous NiMn nanosheets grown on NF (Ni-Mn-P/NF) through a hydrothermal process (at 100 °C for 12 h) and phosphorization of Ni_xMn_1LDH (Fig. 18f) [345]. The Ni/Mn ratio had a significant effect on the HER, wherein Ni_2Mn_1P/

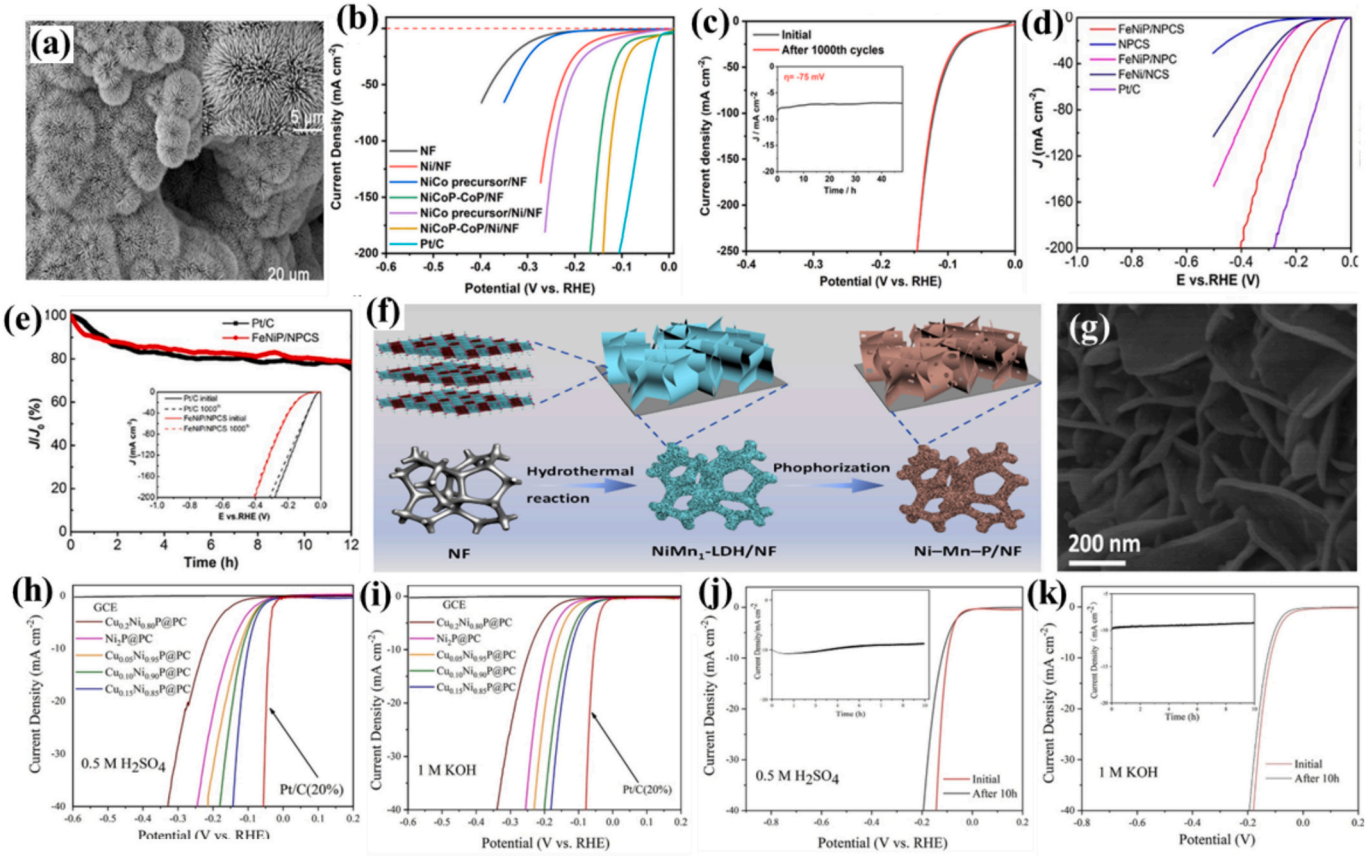

Fig. 18. (a) SEM image of NiCoP-CoP/Ni/NF. (b) LSV curves of NiCoP-CoP/Ni/NF with others measured in 1.0 M KOH and (c) stability tests of NiCoP-CoP/Ni/NF. Reproduced with permission from Ref. [343] Copyright 2021 Elsevier. (d) LSV curves of FeNiP/NPCS with others tested in 0.5 M H_2SO_4, and (e) HER stability of FeNiP/NPCS. Reproduced with permission from Refs. [344] Copyright 2020 Elsevier. (f) Formation process and (g) SEM image of Ni-Mn-P/NF. Reproduced with permission from Refs. [345] Copyright 2020 Elsevier. LSV curves of $Cu_{0.15}Ni_{0.85}P$@PC with others tested in (h) 0.5 M H_2SO_4, (i) 1.0 M KOH. HER stability of $Cu_{0.15}Ni_{0.85}P$@PC with others in (j) 0.5 M H_2SO_4 and (k) 1.0 M KOH. Reproduced with permission from Ref. [346] Copyright 2021 Wiley-VCH.

NF was adjudged to be the best with a η_{10} of 80/120 mV in 0.5 M H_2SO_4/1.0 M KOH compared to Ni_3Mn_1P/NF, Ni_1Mn_1P/NF, Ni_2P, and Ni_2Mn1-LDH (Fig. 18g) [345]. This is due to optimized electronic interaction between Ni/Mn with unique porous nanosheet arrays and NF support. Thus, the combination of the inimitable merits of nanosheet arrays with porous foam structure can enhance the diffusion of reactants, ease the desorption of products, and enhance the interaction with the electrolyte. However, Ni with Mn metals have a relatively poor HER activity. Consequently, the MnCo-P_x, (x = 1, 3, 5) were grown on NF (MnCo-P_3/NF) by the electrodeposition process which exhibited the HER activity depended on x, where MnCo-P_3/NF was identified to be the best [350]. It outperformed MnCo-P1/NF, MnCo-P5/NF, Co-P/NF, and Mn-P/NF with the lowest η_{10} of 47 mV and higher TOF of 0.13 s^{-1} in KOH. This induced porous microspheres with defects and rich active sites, a strong synergy between Mn/Co to modulate the electronic effect, and improved conductivity on the NF and specific surface area. Various Mo-based binary systems have been synthesized for promoting the HER like MoNiP graphene (MoP/MONiP@C) at η_{10} of 134 in 0.5 M H_2SO_4 besides stability for 24 h [351], MoP/MoNiP@NC at η_{10} of 94 mV/137 mV in1.0 M KOH/0.5 M H_2SO_4 with stability for 24 h and high HER rate [352], and Cu-Mo-P/CC at η_{10} of 90.5/132.6/145.9 mV in 1.0 M KOH/1.0 M PBS/0.5 M H_2SO_4 [353]. This is due to their inferior charge transfer resistance, abundant active sites, and modulated d-band of Mo by other metals, which tune the adsorption energies of both reactants and intermediates during the HER.

Compared to Mo, Ni, and Co, Cu metals are known for their supreme electrical conductivity. Not surprisingly, NiCu nanodendrites grown in nickel mesh (NiCuP/NM) and formed by the electrodeposition and phosphidation (at 500 °C for 6 h) had higher HER performance over wide pH [354]. Mainly, NiCuP/NM supported on mesoporous carbon had a low η_{10} of 175 mV in 1.0 M KOH, 250 mV in 1.0 M PBS, and 226 mV in 0.5 M H_2SO_4 compared to CuP/NM and NiP/NM besides a high TOF (0.12–2.6 × 10–6 s^{-1} at η_{400} mV. This is due to its increased surface area, high active sites of NiCu nanodendrites, and impressive electrical conductivity and wettability of NM/NC. This indicates the significant effect of Cu, but the physical mixing with mesoporous NC can devalue the activity relative to its in situ mixed form. The CuNi with different ratios were grown on hierarchical porous carbon ($Cu_xNi_{1-x}P$@PC) using hydrothermal (at 85 °C for 10 h) and phosphorization (at 400 °C for 2 h in N_2 with $NaPO_2H_2$) of Cu/Ni-BMOFs. This drove the formation of ultrafine nanoparticle size (~10 nm) and were well dispersed on PC, and the HER activity depended on the Cu/Ni ratio. However, $Cu_{0.15}Ni_{0.8}P$@PC delivered the highest HER activity at η_{10} of 118 mV in 1.0 M KOH and 102 mV in 0.5 M H_2SO_4 compared to other variants and Ni_2P besides stability for 10 h (Fig. 18h, k) [346]. This indicates the substantial effect of hierarchical porous carbon support on promoting the HER performance of CuNi, although MOF-derived porous carbon is relatively costly and energy-demanding. To this end, porous NiCu alloy nanoparticles with different Ni/Cu ratios were grown on graphitic carbon (NiCuC) and synthesized through physical mixing and phosphorization (at 300 °C for 1 h in Argon). Their activity for HER was depended on the metal ratios [355]. The Ni_2P-Cu_3P@NiCuC was found to be the best at η_{10} of 190 mV in 1.0 M KOH relative to NCP-0, NCP-1, NCP-2, NCP-3, and NCP-4 besides durability for 30 h. The DFT simulation proved the lower ΔGH* on Ni_2P-Cu_3P@NiCuC. This is due to the interconnected porous carbon and highest synergistic interaction among

the NiCu active sites, leading to improved mass transport. Table S2 shows the electrocatalytic HER activity of porous transition binary-metal phosphides formed by various methods.

6. Theoretical studies

6.1. DFT for guiding the experiment

The DFT simulation is an accurate and expeditious method to investigate and predict the HER performance and associated mechanism for HER on various electrocatalysts using various parameters (i.e., shape, composition, electrolyte, and intermediates) [356]. Furthermore, DFT simulation can estimate the effect of various surfaces on HER activity besides the types of relationships among adsorption/desorption energy of H_2O and intermediates (i.e., H^+ and OH^- ions) hydroxyl [357,358]. Mainly, the DFT simulation can construct a volcano plot, which reveals the ΔG_{H^*} for different metals via describing linear correlations between the binding energies of intermediates. Calculation of ΔG_{H^*} is coupled with lattice energy and work function to generate a volcano-shaped relationship and serve as an indication for HER performance. The highest HER rate is represented by the maximum of the volcano plot (location of the binding energy of intermediates close to the peak of the volcano) [356]. The correlation of ΔG_{H^*} with HER activity (exchange current density) in a volcano relationship act as a fundamental descriptor for guiding the design of metal-based catalysts with and without support for HER. The DFT is a powerful tool in guiding the experimental design for active HER electrocatalysts via the identification of optimum active sites for H_2-ads adsorption on the catalyst's surface besides optimizing the catalysts via calculation of ideal ΔG_{H^*} that endow adsorption on the catalyst neither too weakly nor too strongly, thus easing efficient release after HER [359]. This led to understanding HER mechanisms and pathways which subsequently can direct the design of experiments according to such steps for improvement. Moreover, DFT can predict the electronic, structural, and magnetic properties of materials, which are essential merits for understanding their HER behavior, thus endowing the design of novel materials with desired HER performance before being testing at the lab. Finally DFT can screen the potential of several metals under varying conditions and consequently reduce the trial-and-error aspect of experimental work, saving time, resources, and hence allowing more focused and efficient experimentation.

6.2. Theoretical studies of porous transition binary-metal electrocatalysts for HER

Various studies have been carried out to investigate the HER activity and durability of binary metal-based electrocatalysts, but the studies on porous binary systems are not underlined enough. To this end, Nørskov et al. used DFT simulation to predict the HER activity and durability of >700 binary alloys, and the volcano plot revealed the superior performance of binary Pt-based relative to mono Pt [360]. Intriguingly, the volcano plot demonstrates that Ni is the most promising transition metal to be alloyed with Pt for promoting the HER activity because its $|\Delta G_{H^*}|$ was closest to zero. Also, Ni is eminent with its unique ability to optimize the interaction with the active sites, promoted by the structural features and synergetic effects. Moreover, Ni could be easily alloyed with other metals deploying assorted methods (i.e., template, solvothermal, and electrochemical deposition) with and without supports. To check whether metal or non-meta atoms are better for binary metals electrocatalysts, Norskov et al. used DFT simulation to calculate the free

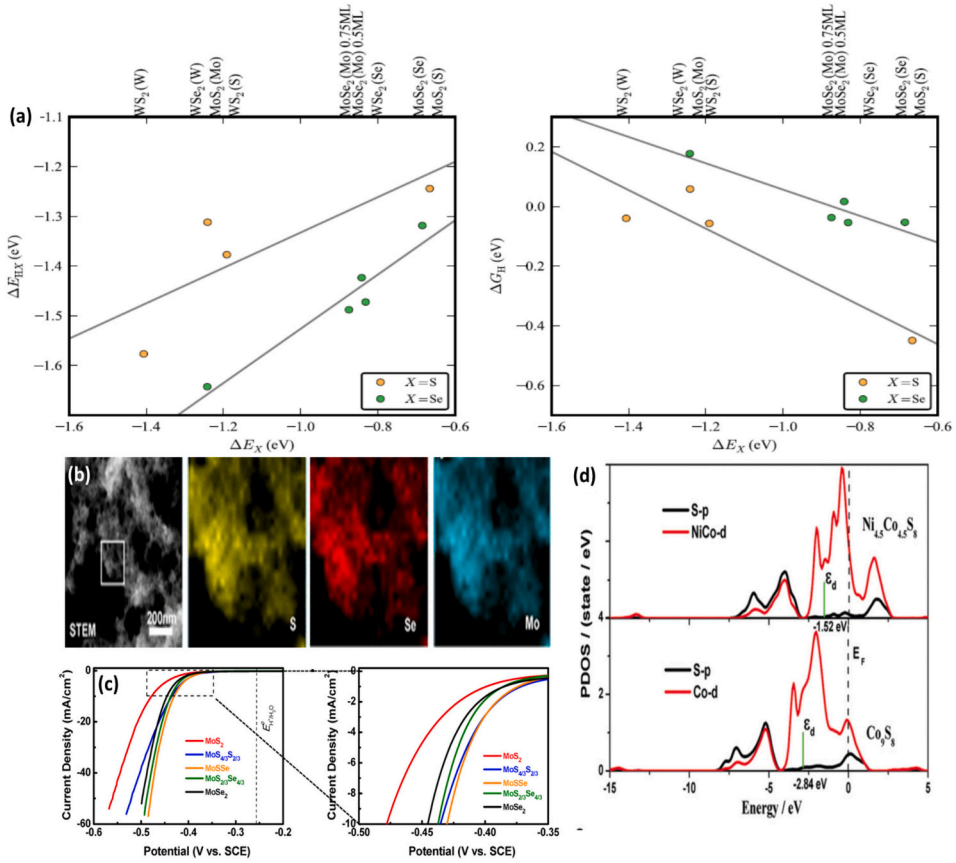

Fig. 19. (a) Plot of HX adsorption energy and ΔG_H based on S and Se (X) adsorption energy (DEX). Reproduced with permission from Ref. [362] Copyright 2014 RSC. (b) HAADF-STEM and elemental mapping images of MoSSe. (c) LSV curves of of $MoS_{2(1-x)}Se_{2x}$ nanoflakes measured in 0.5 M H_2SO_4. Reproduced with permission from Ref. [363] Copyright 2015 ACS. (d) PDOS for Co_9S_8 and $Ni4.5Co_{4.5}S_8$ electrocatalysts. Reproduced with permission from Ref. [366] Copyright 2018 RSC.

energies of hydrogen adsorption (ΔGH) on the active edge sites of edge MoS_2/graphite, WSe_2, and $MoSe_2$ which are about ~0.08, 0.17, and −0.04 eV, respectively (Fig. 19a) [361,362]. Moreover, the strong ΔGH on $MoSe_2$ suggested the high possibility of attaining a thermoneutral ΔGH via binary alloy with tunable S/Se ratio (i.e., $MoS_{2(1-x)}Se_{2x}$ and $WS_{2(1-x)}Se_{2x}$) flakes for efficient HER [363]. Also, modification of the metal atom at the edge via doping can optimize ΔGH and HER as confirmed by the experimental study, which revealed porous flake-like structure of MoSSe (Fig. 19b) and displayed HER η_{10} of mV that is lower than MoS_2, $MoS_{4/3}Se_{2/3}$, $MoS_{2/3}Se_{4/3}$, $MoSe_2$, 219, 172, 171, and 181 mV, respectively (Fig. 19c). MoSSe outperformed various MoSe-based electrocatalysts with different morphologies, like MoSe/graphene sheets [364] and $MoSe_2$ thin films with vertically aligned layers [365], in view of optimized ΔGH via doping with S at the edge of Mo. Likewise, the porous $Ni_{4.3}Co_{4.7}S_8$ sphere with high overlap DOS at the Fermi-level, raise of the d-state center (from −2.84 to −1.52 eV) (Fig. 19d), and high occupation of the anti-bonding e_g ($d^2_{x^2-y}$ and d^2_z) d-orbitals showed a comparative HER activity to commercial Pt/C and a low η_{10} for full water splitting in an alkaline electrolyte [366]. O-coordinated W-Mo/N-doped porous graphene (NPG) was predicted to display Pt-like HER activity in all pH ranges and higher activity than Mo_2-NPG, W_2-NPG, and NPG [367], and it matched the experimental study. Likewise, binary Pt—Ru single atoms outperformed Pt single atoms with a η of 0.05 V [368]. However, their performance is still not practical as they include 4d or 5d transition metals, which heighten the environmental issues.

Unlike these studies, two 3d-transition metal atoms encapsulated NPG (MM' where M is for Fe, Co, Ni and M' are for Ti, V, Cr, Mn, Fe, Co, Ni, Cu, and Zn electrocatalysts were designed for HER in acidic and alkaline electrolytes using the DFT simulation. The DFT showed that FeCr-NPG, FeCo-NPG, FeNi-NPG, NiTi-NPG, NiV-NPG, and NiNi-NPG are expected to be durable thermodynamically via forming solid metal-metal and metal-N bonds (Fig. 20a) and can deliver higher HER performance than Pt under acidic conditions, although FeV-NPG and NiV-NPG are better under alkaline conditions with a predicted theoretical overpotential and kinetic barrier lower than 0.37 and 0.16 eV, respectively. The HER volcano curve of current density (i_0) vs. Gibbs free energy of hydrogen adsorption (ΔG_{H^*}) showed the location of FeCr-NPG, FeCo-NPG, FeNi-NPG, NiTi-NPG, NiV-NPG and NiNi-NPG around the peak of the volcano with a smaller $|\Delta G_{H^*}|$ ranged from 0.01 eV to −0.02 eV and higher HER activity than Pt catalyst ($\Delta G_{H^*} = -0.09$ eV) (Fig. 20b). The mechanism in alkaline electrolytes includes H_2O adsorption, dissociation, OH^- desorption, and H_2 production (Fig. 20c).

Notably, only 10 MM'-NPGs had a strong ability of H_2O adsorption, and their calculated ΔG_{diss} for H_2O-dissociation revealed the ability of FeTi-NPG, FeV-NPG, FeMn-NPG, CoTi-NPG, CoV-NPG, CoCr-NPG, NiTi-NPG, and NiV-NPG to adsorb/activate H_2O at room temperature (Fig. 20d). The expected theoretical overpotential of FeV-NPG, NiV-NPG, FeMn-NPG, CoCr-NPG, FeTi-NPG, CoTi-NPG, NiTi-NPG, and CoV-NPG was about 0.32, 0.37, 0.65, 0.66, 0.76, 0.79, 0.96, and 1.06 eV, respectively. This is due to the superior ability to endow the interaction of the d-orbital of NiV with σ* orbitals of H_2O to accelerate the H_2O-dissociation to H/OH radicals, which are captured by Ni/V atoms with inferior energy barriers in alkaline electrolyte. This study can pave the way for the preparation of FeV-NPG and NiV-NPG for HER in different electrolytes. There are various binary metal-based electrocatalysts with different shapes and compositions that have been examined for the HER by the DFT simulation, which varied in their performance under acidic and

Table 1
Comparison of HER activity under acidic and alkaline conditions for MM'-NPG with other catalysts.

Catalyst	$\lvert\Delta G_{H^*}\rvert$(eV)	Electrolyte	Refs
FeCr-NPG0.01	0.01	Acidic	[369]
NiV-NPG	0.02	Acidic	[369]
PtPt-NPG	0.43	Acidic	[369]
Pt-layer/Ru(101)	0.05	Acidic	[370]
Pt(111)	0.19	Acidic	[370]
Pt_2/Ru(101)	0.06	Acidic	[370]
Pt@C_9N_4	0.06	Acidic	[371]
PtN1C	0.08	Acidic	[372]
Pt-NG	1.49	Acidic	[373]
Mo-ISA/N1C	0.04	Acidic	[374]
MoS_2|P	0.24	Acidic	[375]
Mo–N/C@MoS_2	0.24	Acidic	[376]
W-SAC	0.03	Acidic	[377]
$Mo_1N_1C_2$	0.08	Acidic	[378]
Ru-MoS_2	0.33	Acidic	[379]
Pd–MoS_2	0.02	Acidic	[380]
Ni@Ni-Fe	0.14	Acidic	[381]
NiV-NPG	0	Alkaline	[369]
Cr–Co_4N	0.58	Alkaline	[382]
CoP–MoO_2	0.70	Alkaline	[383]
D-PtC_2N_1-III	0.17	Alkaline	[384]
NiP	0.82	Alkaline	[385]
NiS_2	0.80	Alkaline	[381]
Co-NiS_2	1.38	Alkaline	[381]

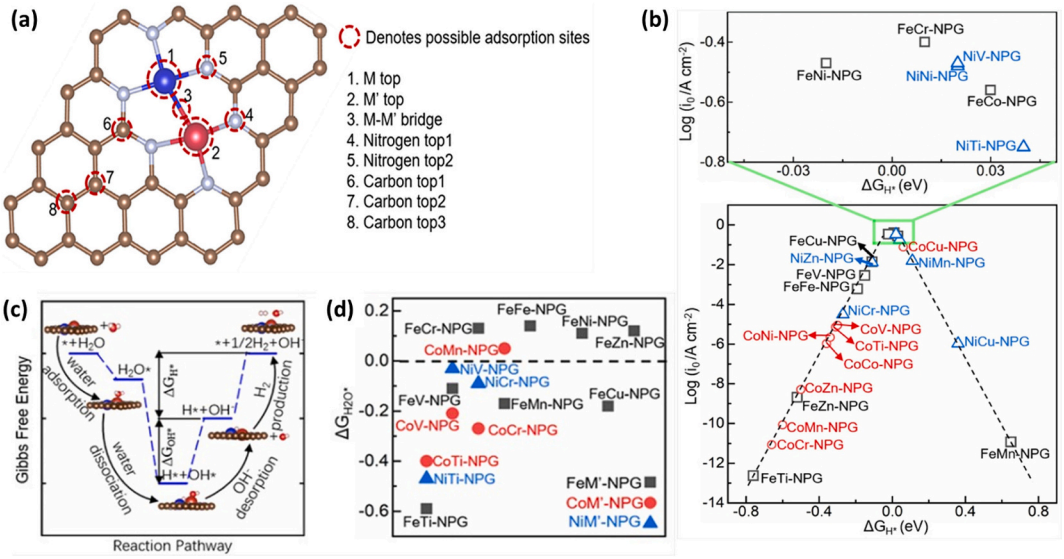

Fig. 20. (a) Molecular structure with possible H adsorption sites on MM'-NPG surface, (b) HER volcano plot of i_0 vs. ΔG_{H^*} on MM'-NPG, (c) the elementary steps, and (d) free energy changes of H_2O adsorption on MM'-NPG surfaces for alkaline HER. Reproduced with permission from Ref. [369] Copyright 2021 Elsevier.

alkaline conditions, although binary systems were always superior to mono-metallic ones (Table 1). Notably, both Ni and Mo are the most promising metals to be alloyed with others to promote HER activity close to Pt-based catalysts, but NiV-NPG is predicted to enhance HER in both acidic and alkaline electrolytes. However, the effect of porosity on HER activity and stability is still ambiguous, and all theoretical studies have mainly focused on the composition rather than the morphology of binary metal catalysts for HER. More DFT studies are needed to optimize the structural merits of porous binary metal-based electrocatalysts and direct the synthesis of novel HER electrocatalysts.

7. Conclusions and future perspectives

This comprehensive review discusses the controlled fabrication of porous binary transition/noble metals and transition metal electrocatalysts (i.e., carbides, oxides, nitrides, phosphides, and chalcogenides) for the HER. This is rooted in the experimental (i.e., synthesis strategies and electrochemical tests) and theoretical insights (i.e., DFT simulations), including the associated mechanisms and fundamental and educational pathways. Various self-standing and supported porous binary transition/noble metals have been synthesized in various morphological forms (i.e., spherical-like, nanodandelions, nanodendrites, nanosheets, nanotubes, and nanofibers) and were assessed for the HER (Fig. 21). This has been accomplished deploying various methods such as hydrothermal, microwave, template, electrospinning, electrochemical, ion-exchange, and co-precipitation, among others. These electrocatalysts displayed an η_{10} of 9–150 mV in various electrolytes with stability of 2.8–100 h, where $VRu_{0.027}O_x$/GDY nanoclusters [192] and Ni_xRh_{1-x}@200 nanofibers [190] had the lowest η_{10} of 13.0 and 9.4, respectively. Porous binary transition metals carbides/oxides/nitrides/phosphides, and metal chalcogenides were fabricated in different nanostructure forms (i.e., rods, sheets, tubes, fibers, cubes, foam, cage, urchin-like, flowers, and needles), but the Co-based electrocatalysts, including Co-M (M = W, Mo, Fe, Cu, Ni, Zn, and Mn) with and without supports were the most common (Fig. 21). These electrocatalysts exhibited η_{10} of 32–400 mV and stability of 1.1–100 h in various electrolytes, however NiFe(1:1)P-MOF nanoflowers [341] and NiCoP-CoP/Ni/NF nanowires [343] were found to be the best with η_{10} of 32 mV and 49 mV, respectively. The solvothermal is the most common protocol deployed and has been promising due to its simplicity and relatively high yields besides its feasibility from supported or self-standing porous binary metals with various morphologies.

However, the current fabrication methods are not scalable, owing to their complications and low yield (i.e., few milligrams) [386]. The characterization of these electrocatalysts at the atomic level is technically demanding and requires advanced techniques to elucidate their surface structure-HER performance relationship. The higher costs are still challenging because the majority of high-performance and durable porous binary metal-based electrocatalysts involve expensive or scarce metals (i.e., Pt, Pd, Ir, and Ru), which limit their practical use. The obtained HER activity of thus reported porous binary transition metals is still inferior, including the consumption of −1 V to deliver current density $\leq$ 500 mA/cm^2 and durability of a few hours $\sim \leq$ 4.1 h, which are not adequate for large-scale appliances. Additionally, these electrocatalysts can not perform under high current density at 0.5–1 A/cm^2, and most of them function in either acidic or alkaline electrolytes. The practical applications require electrocatalysts to be able to work in different electrolytes with various pH (i.e., acidic, neutral, and alkaline) at high current density 500 mAcm^{-2}–1000 mA/cm^2 along with durability spanning either weeks or months. The insufficient durability of these electrocatalysts resulting from the harsh conditions and corrosive environments under high currents, can lead to degradation, aggregation, surface destruction, and metal dissolution during HER. Meanwhile, the complex interactions of transition metals with either reactants and intermediates or products at high current density lead to limited mass transport and instability, thus subsequently losing activity. Moreover, the higher cost of hydrogen production through the electrochemical HER is still elevated $\sim \geq$7 USD/kg, which is nearly 4 times of other methods (i.e., reforming or gasification). Therefore, numerous outlooks could be considered to address the current shortcomings of porous binary metal-based catalysts which comprise:

- Simple, one-step, productive, low-energy demand and greener preparative methods ought to be developed for porous binary metal-based electrocatalysts. This could be achieved by direct co-reduction of binary metal precursors deploying strong reducing agents (i.e., $NaBH_4$, ascorbic acid, and hydrazine) in aqueous-solutions of ionic/non-ionic copolymers (i.e., Pluronic F127, polyvinylpyrrolidone (PVP), Brij 58, and CTAB) as in-situ templates under mild conditions. This approach can create distinct porous structures with unique features (i.e., accessible active sites, high surface area, and stability) and comprise mixed metal atoms at atomic scale rather than segregation, which are highly desirable features in HER [142,144,145].
- The in-situ preparation of porous binary metals on solid supports (i.e., carbon cloth, carbon fleece, metal oxide/hydroxide/sulfide) can form cathodes with high electrical conductivity and stability at high current density $\sim$ 500–1000 mAcm^{-2} under different pH conditions. This protocol can allow the homogenous distribution and stabilization of metal active sites inside the skeleton of supports, which make them more accessible, reducing charge transfer resistance, enhancing stability against dissolution, and weakening the adsorption of intermediates thus culminating in high HER durability for several weeks. Meanwhile, other supports, like MXenes [387,388], MOFs [389], g-C_3N_4 [70,390,391], and graphdiyne [392]) could be used instead of activated carbon, due to their unique electronic merits to enhance the electrochemical HER.
- Mixing of two metals with dissimilar oxophilic effects could boost the polarity to ease H_2O dissociation at low overpotential that leads to the optimum H-desorption/discharge step, thus rendering the activation energies for H-desorption closer to the thermodynamic potential during HER electrocatalysts. This can lead to outstanding current density ($\geq$1000 mAcm^{-2}) at low overpotential and enhance the durability for several weeks, as we have demonstrated in our recent work [277]. Moreover, conducting the HER on porous transition metals in ionic liquid, organic electrolytes, and solid polymer electrolytes can lead to an outstanding performance with impressive current density and long-term durability due to the stability of these electrolytes and high electrical conductivity.
- More theoretical studies (i.e., DFT) ought to be conducted with and without experimental data on the porous binary metal-based electrocatalysts to optimize their electronic effect, active sites, phases, strain, phase engineering, and support interaction during HER. Also, machine learning can allow electrocatalysts' screening to identify promising bimetallic catalyst candidates, understand the structure-HER property relationships, and predict their HER activity quickly/efficiently. This is besides accelerating the electrocatalysts' design and identification of descriptors/features that correlate with improved HER activity and save time and laboratory resources.
- The in-situ characterization tools (i.e., XPS, Raman, FTIR, and EXAFS) could be deployed during HER electrocatalysis to decipher the structural-HER activity relationship along with the role of electrolytes (i.e., type, concentration, and composition), and estimate the adsorption/desorption kinetics of intermediates.
- The cell design could be modified to allow the direct storage of hydrogen produced, and additional current collectors could be developed for better interaction with the electrocatalysts.

Declaration of competing interest

The authors declare that they have no known competing financial interests or personal relationships that could have appeared to influence

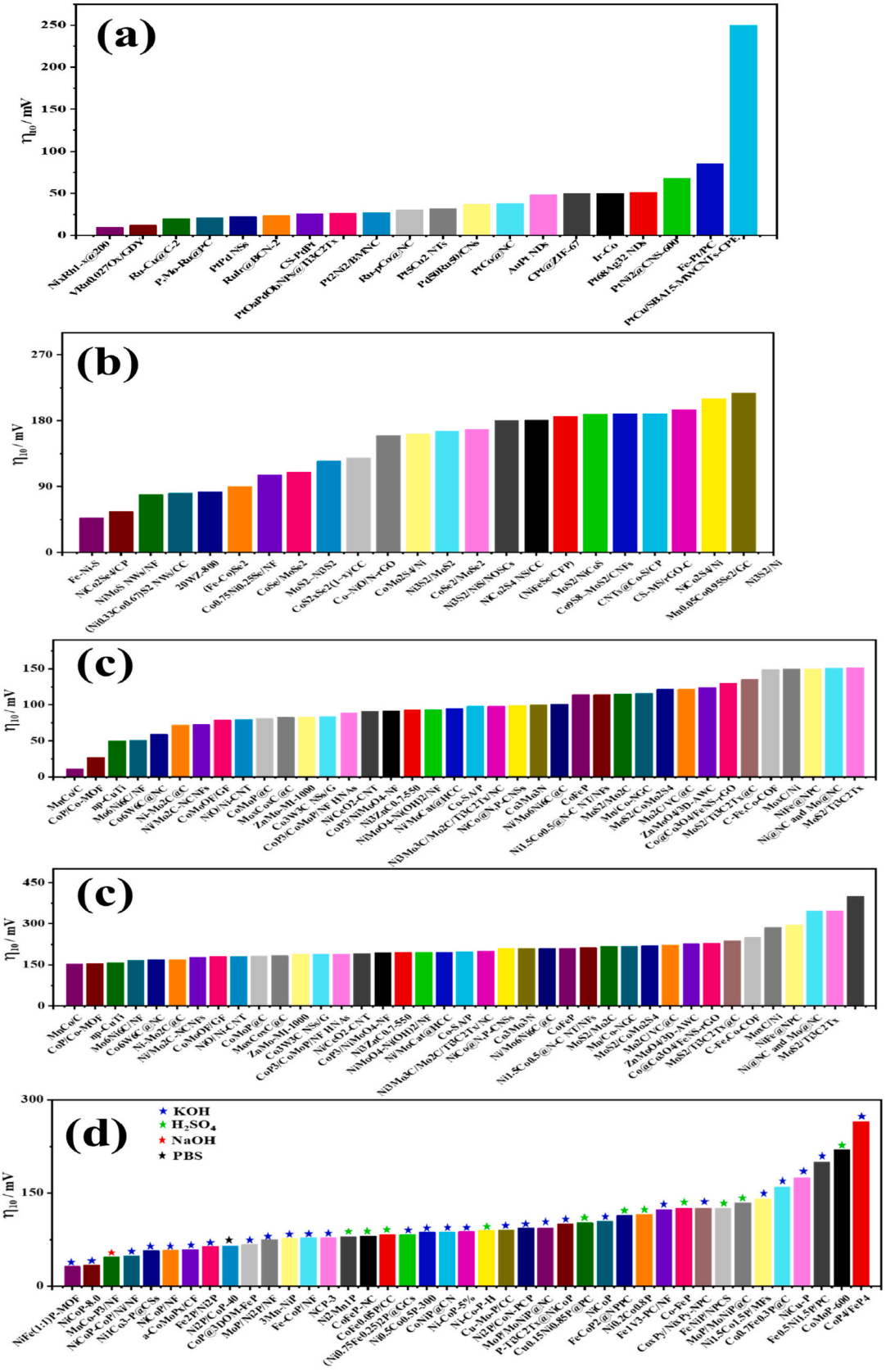

Fig. 21. Comparison of the HER activity of porous binary transition metals including (a) transition-noble, (b) dichalcogenide, (c) oxide/carbides/nitride, and (d) binary metal phosphide.

the work reported in this paper.

Data availability

Data will be made available on request.

Acknowledgment

The authors greatly appreciate their organizations for supporting this work. Eid thanks the Gas Processing Center, College of Engineering, Qatar University, for supporting this work. Ozoemena thanks the South Africa's National Research Foundation (NRF) and the Department of Science and Innovation for their support through the SARChI Chair program (UID no.: 132739).

Appendix A. Supplementary data

Supplementary data to this article can be found online at https://doi.org/10.1016/j.ccr.2024.216238.

References

[1] Q. Lu, K. Eid, W. Li, A.M. Abdullah, G. Xu, R.S. Varma, Green Chem. 23 (2021) 5394–5428.
[2] H. Zhang, Y. Fu, H.T. Nguyen, B. Fox, J.H. Lee, A.K.-T. Lau, H. Zheng, H. Lin, T. Ma, B. Jia, Coord. Chem. Rev. 494 (2023) 215272.
[3] Q. Lu, K. Eid, W. Li, Nanomaterials 12 (2022) 2379.
[4] Q. Lu, J. Li, K. Eid, X. Gu, Z. Wan, W. Li, R.S. Al-Hajri, A.M. Abdullah, J. Electroanal. Chem. 916 (2022) 116361.
[5] T.P. Mofokeng, A.K. Ipadeola, Z.N. Tetana, K.I. Ozoemena, ACS omega 5 (2020) 20461–20472.
[6] H. Jiang, G.F. Chen, G. Hai, W. Wang, Z. Liang, L.X. Ding, Y. Yuan, J. Lu, M. Antonietti, H. Wang, Angew. Chem. Int. Ed. 135 (2023) e202305695.
[7] P. Caprioglio, D.S. Cruz, S. Caicedo-Dávila, F. Zu, A.A. Sutanto, F. Peña-Camargo, L. Kegelmann, D. Meggiolaro, L. Gregori, C.M. Wolff, Energy Environ. Sci. 14 (2021) 4508–4522.
[8] H.I. Abdu, K. Eid, A.M. Abdullah, M.H. Sliem, A. Elzatahry, X. Lu, Green Chem. 22 (2020) 5437–5446.
[9] Z. Zeb, Y. Huang, L. Chen, W. Zhou, M. Liao, Y. Jiang, H. Li, L. Wang, L. Wang, H. Wang, Coord. Chem. Rev. 482 (2023) 215058.
[10] P. Aggarwal, D. Sarkar, K. Awasthi, P.W. Menezes, Coord. Chem. Rev. 452 (2022) 214289.
[11] A.K. Ipadeola, A.K. Lebechi, L. Gaolatlhe, A.B. Haruna, M. Chitt, K. Eid, A. M. Abdullah, K.I. Ozoemena, Electrochem. Commun. 136 (2022) 107207.
[12] A. Gamal, K. Eid, A.M. Abdullah, Int. J. Hydrog. Energy 47 (2021) (2021) 5901–5928.
[13] A. Abdelgawad, B. Salah, Q. Lu, A.M. Abdullah, M. Chitt, A. Ghanem, R.S. Al-Hajri, K. Eid, J. Electroanal. Chem. 938 (2023) 117426.
[14] K. Bhunia, M. Chandra, S.K. Sharma, D. Pradhan, S.-J. Kim, Coord. Chem. Rev. 478 (2023) 214956.
[15] S. Zhang, C. Wang, X. Zhang, H. Xia, B. Huang, S. Guo, J. Li, E. Wang, A.C.S. Appl, Mater. Interf. 13 (2021) 32997–33005.
[16] L. Cui, Y. Liu, X. Fang, C. Yin, S. Li, D. Sun, S. Kang, Green Chem. 20 (2018) 1354–1361.
[17] T.-Y. Shuai, Z. Qi-Ni, H. Xu, Z. Zhi-Jie, G.-R. Li, Green Chem. 25 (2023) 1749–1789.
[18] J. Zhu, L. Hu, P. Zhao, L.Y.S. Lee, K.-Y. Wong, Chem. Rev. 120 (2020) 851–918.
[19] Y. Duan, P. Guo, D. Sui, D. Deng, T. Lu, Y. Yang, Int. J. Hydrog. Energy 47 (2022) 36098–36109.
[20] H. Jin, X. Wang, C. Tang, A. Vasileff, L. Li, A. Slattery, S.Z. Qiao, Adv. Mater. 33 (2021) 2007508.
[21] H. Liu, J. Li, Y. Zhang, R. Ge, J. Yang, Y. Li, J. Zhang, M. Zhu, S. Li, B. Liu, Chem. Eng. J. 473 (2023) 145397.
[22] W.-T. Chung, I.M. Mekhemer, M.G. Mohamed, A.M. Elewa, A.F. EL-Mahdy, H.-H. Chou, S.-W. Kuo, K.C.-W. Wu, Coord. Chem. Rev. 483 (2023) 215066.
[23] I.F. Teixeira, N.V. Tarakina, I.F. Silva, G.A.A. Diab, N.L. Salas, A. Savateev, M. Antonietti, J. Mater. Chem. A 10 (2022) 18156–18161.
[24] D. Wan, B. Yan, J. Chen, S. Wu, J. Hong, D. Song, X. Zhao, X. Chi, S. Zeng, Z. Huang, C. Li, K. Han, W. Zhou, Y. Cao, A. Rusydi, S.J. Pennycook, P. Yang, R. Ariando, Q.-H. Xu, X.R. Xu, T. Venkatesan Wang, Chem. Mater. 31 (2019) 2320–2327.
[25] H. Wu, C. Feng, L. Zhang, J. Zhang, D.P. Wilkinson, Electrochem. Energy Rev. 4 (2021) 473–507.
[26] H. Du, R.-M. Kong, X. Guo, F. Qu, J. Li, Nanoscale 10 (2018) 21617–21624.
[27] Y. Lu, W. Wang, H. Cheng, H. Qiu, W. Sun, X. Fang, J. Zhu, Y. Zheng, Int. J. Hydrog. Energy 47 (2022) 3733–3740.
[28] Z. Durmus, A.W. Maijenburg, Int. J. Hydrog. Energy 47 (2022) 36784–36813.
[29] B. Zhu, R. Zou, Q. Xu, Adv. Energy Mater. 8 (2018) 1801193.
[30] H. Jin, H. Yu, H. Li, K. Davey, T. Song, U. Paik, S.Z. Qiao, Angew. Chem. Int. Ed. 134 (2022) e202203850.
[31] H. Javan, E. Asghari, H. Ashassi-Sorkhabi, M. Moradi-Haghighi, Int. J. Hydrog. Energy 45 (2020) 19324–19334.
[32] Y. Wang, Z. Hu, W. Chen, S. Wu, G. Li, S. Chou, Small Struct. 2 (2021) 2000135.
[33] X. Liu, J. Niu, S. Rajendran, Y. Lei, J. Qin, X. Zhang, Int. J. Hydrog. Energy 47 (2021) 41994–42000.
[34] X. Wen, J. Guan, Appl. Mater. Today 16 (2019) 146–168.
[35] J. Ying, H. Wang, Front. Chem. 9 (2021) 700020.
[36] J. Mohammed-Ibrahim, X. Sun, J. Energy Chem. 34 (2019) 111–160.
[37] A. Eftekhari, Int. J. Hydrog. Energy 42 (2017) 11053–11077.
[38] F. Guo, T.J. Macdonald, A.J. Sobrido, L. Liu, J. Feng, G. He, Adv. Sci. 10 (2023) 2301098.
[39] X. Zhou, H. Dong, A.-M. Ren, Int. J. Hydrog. Energy 41 (2016) 5670–5681.
[40] J.R. Varcoe, P. Atanassov, D.R. Dekel, A.M. Herring, M.A. Hickner, P.A. Kohl, A. R. Kucernak, W.E. Mustain, K. Nijmeijer, K. Scott, Energy Environ. Sci. 7 (2014) 3135–3191.
[41] A.K. Ipadeola, K.I. Ozoemena, RSC Adv. 10 (2020) 17359–17368.
[42] Y. Zheng, Y. Jiao, M. Jaroniec, S.Z. Qiao, Angew. Chem. Int. Ed. 54 (2015) 52–65.
[43] B.E. Conway, B.V. Tilak, Electrochim. Acta 47 (2002) 3571–3594.
[44] G.K. Gebremariam, A.Z. Jovanović, I.A. Pašti, Hydrogen 4 (2023) 776–806.
[45] K. Chen, B. Xu, L. Shen, D. Shen, M. Li, L.-H. Guo, RSC Adv. 12 (2022) 19452–19469.
[46] S. Wan, O. Xu, X. Zhu, Ionics 27 (2021) 445–456.
[47] N. Dubouis, P. Lemaire, B. Mirvaux, E. Salager, M. Deschamps, A. Grimaud, Energy Environ. Sci. 11 (2018) 3491–3499.
[48] Y.-S. Hsu, S.T. Rathnayake, M.M. Waegele, J. Chem. Phys. 160 (2024).
[49] P. Cavaliere, Proton exchange membrane water electrolysis, in: Water Electrolysis for Hydrogen Production, Springer International Publishing, Cham, 2023, pp. 233–285.
[50] T. Wang, X. Cao, L. Jiao, Carbon Neutrality 1 (2022) 21.
[51] J. Yu, D. Wei, Z. Zheng, W. Yu, H. Shen, Y. Qu, S. Wen, Y.-U. Kwon, Y. Zhao, J. Colloid Interface Sci. 566 (2020) 505–512.
[52] K. Eid, Y.H. Ahmad, S.Y. AlQaradawi, N.K. Allam, Cat. Sci. Technol. 7 (2017) 2819–2827.
[53] K. Eid, Y.H. Ahmad, H. Yu, Y. Li, X. Li, S.Y. AlQaradawi, H. Wang, L. Wang, Nanoscale 9 (2017) 18881–18889.
[54] F. Wu, K. Eid, A.M. Abdullah, W. Niu, C. Wang, Y. Lan, A.A. Elzatahry, G. Xu, ACS Appl. Mater. Interfaces 12 (2020) 31309–31318.
[55] H. Zhang, H. Wang, K. Eid, L. Wang, Part. Part. Syst. Charact. 32 (2015) 863–868.
[56] X. Li, W. Yan, B. Fan, Z. Wang, J. Alloys Compd. 960 (2023) 170730.
[57] S. Zhai, Y. Feng, Z.-Y. Yuan, Int. J. Hydrog. Energy 48 (2023) 34677–34699.
[58] M. Zhang, W. Zhou, X. Yan, X. Huang, S. Wu, J. Pan, Z. Shahnavaz, T. Li, X. Yu, Fuel 333 (2023) 126323.
[59] Z. Chen, H. Hu, L. Yin, Z. Zhao, J.-H. Choi, G. Liu, F. Geng, Proc. Natl. Acad. Sci. 120 (2023) e2209760120.
[60] K. Pellumbi, J. Wolf, S.C. Viswanathan, L. Wickert, M.-A. Kräenbring, J. T. Kleinhaus, K. Junge Puring, F. Özcan, D. Segets, U.-P. Apfel, RSC Sustainabil. 1 (2023) 631–639.
[61] J. Lai, S. Li, F. Wu, M. Saqib, R. Luque, G. Xu, Energy Environ. Sci. 9 (2016) 1210–1214.
[62] H.F. Wang, R. Chen, J. Feng, M. Qiao, S. Doszczeczko, Q. Zhang, A.B. Jorge, M. M. Titirici, ChemElectroChem 5 (2018) 1786–1804.
[63] R. Yang, Y. Zhou, Y. Xing, D. Li, D. Jiang, M. Chen, W. Shi, S. Yuan, Appl. Catal. B Environ. 253 (2019) 131–139.
[64] A. Huang, P. Liu, P. Lin, M. Fang, G. Jin, C. Chen, Ionics 29 (2023) 1531–1541.
[65] S. Chaitoglou, R. Amade, R. Ospina, E. Bertran-Serra, ACS Appl. Energy Mater. 6 (2023) 6120–6131.
[66] R. Rajalakshmi, G. Srividhya, C. Viswanathan, N. Ponpandian, Appl. Catal. B Environ. 339 (2023) 123089.
[67] M.I. Zappia, S. Bellani, Y. Zuo, M. Ferri, F. Drago, L. Manna, F. Bonaccorso, Front. Chem. 10 (2022) 1045212.
[68] B. Salah, A.K. Ipadeola, A.M. Abdullah, A. Ghanem, K. Eid, Int. J. Mol. Sci. 24 (2023) 11832.
[69] K. Eid, ChemCatChem (2024) e202301747.
[70] B. Salah, A. Abdelgawad, Q. Lu, A.K. Ipadeola, R. Luque, K. Eid, Green Chem. 25 (2023) 6032–6040.
[71] J. Gu, Y.-W. Zhang, F.F. Tao, Chem. Soc. Rev. 41 (2012) 8050–8065.
[72] C. Zhu, D. Du, A. Eychmüller, Y. Lin, Chem. Rev. 115 (2015) 8896–8943.
[73] B. Lim, Y. Xia, Angew. Chem. Int. Ed. 50 (2011) 76–85.
[74] B. Salah, A.K. Ipadeola, A.M. Abdullah, K. Eid, ACS Appl. Eng. Mater. 1 (2023) 2196–2206.
[75] S. Lu, K. Eid, M. Lin, L. Wang, H. Wang, H. Gu, J. Mater. Chem. A 4 (2016) 10508–10513.
[76] J. Hao, B. Liu, M. Takahashi, S. Maenosono, J. Yang, Cat. Sci. Technol. 13 (2023) 4141–4147.
[77] X. Kong, H. Wu, K. Lu, X. Zhang, Y. Zhu, H. Lei, ACS Appl. Mater. Interfaces 15 (2023) 41205–41223.
[78] S. Lu, K. Eid, Y. Deng, J. Guo, L. Wang, H. Wang, H. Gu, J. Mater. Chem. A 5 (2017) 9107–9112.
[79] Q. Lu, H. Wang, K. Eid, Z.A. Alothman, V. Malgras, Y. Yamauchi, L. Wang, Chem. Asian J. 11 (2016) 1939–1944.
[80] L. Sun, H. Wang, K. Eid, S.M. Alshehri, V. Malgras, Y. Yamauchi, L. Wang, Electrochim. Acta 188 (2016) 845–851.
[81] Q. Lu, X. Gu, J. Li, W. Li, R. Luque, K. Eid, Ultrason. Sonochem. 98 (2023) 106494.

[82] J. Kim, Y. Hong, K. Lee, J.Y. Kim, Adv. Energy Mater. 10 (2020) 2002049.
[83] Z. Su, T. Chen, Small 17 (2021) 2005354.
[84] J. Tang, J. Xu, Z. Ye, Y. Ma, X. Li, J. Luo, Y. Huang, J. Alloys Compd. 885 (2021) 160995.
[85] K.A. Adegoke, N.W. Maxakato, Coord. Chem. Rev. 457 (2022) 214389.
[86] D.P. Sahoo, K.K. Das, S. Mansingh, S. Sultana, K. Parida, Coord. Chem. Rev. 469 (2022) 214666.
[87] F. Wu, W. Niu, J. Lai, W. Zhang, R. Luque, G. Xu, Small 15 (2019) 1804407.
[88] T. Ni, Y. Zhong, J. Sunarso, W. Zhou, R. Cai, Z. Shao, Electrochim. Acta 207 (2016) 58–65.
[89] F. Yang, Y. Zhang, P.-F. Liu, Y. Cui, X.-R. Ge, Q.-S. Jing, Int. J. Hydrog. Energy 41 (2016) 6773–6780.
[90] Y. Fan, Y. Zhang, Y. Cui, J. Wang, M. Wei, X. Zhang, W. Li, RSC Adv. 6 (2016) 83373–83379.
[91] M. Chen, Q. Su, N. Kitiphatpiboon, J. Zhang, C. Feng, S. Li, Q. Zhao, A. Abudula, Y. Ma, G. Guan, Fuel 331 (2023) 125794.
[92] Y. Huo, S. Xiu, L.-Y. Meng, B. Quan, Chem. Eng. J. 451 (2023) 138572.
[93] J. Lai, W. Niu, R. Luque, G. Xu, Nano Today 10 (2015) 240–267.
[94] M. Ohtani, T. Muraoka, Y. Okimoto, K. Kobiro, Inorg. Chem. 56 (2017) 11546–11551.
[95] H.M. Kareem, R.T. Abd Alrubaye, IOP Conference Series: Materials Science and Engineering, IOP Publishing, 2019, p. 062013.
[96] L. Mai, Q. An, Q. Wei, J. Fei, P. Zhang, X. Xu, Y. Zhao, M. Yan, W. Wen, L. Xu, Small 10 (2014) 3032–3037.
[97] K. Kan, E. Yamamoto, M. Ohtani, K. Kobiro, Eur. J. Inorg. Chem. 2020 (2020) 4435–4441.
[98] V.M. Dhavale, S. Kurungot, ACS Catal. 5 (2015) 1445–1452.
[99] Q. Chen, H. Li, Z. Wu, L. Zhu, C. Li, X. Zhu, Y. Sun, Mater. Today Chem. 30 (2023) 101585.
[100] F. Ma, R. Jin, K. Zhou, Y. Zhu, T. Huang, Q. Lu, L. Gai, L. Liu, R.S. Varma, K. Eid, Chem. Eng. J. 492 (2024) 151988.
[101] S. Khalid, C. Cao, L. Wang, Y. Zhu, Sci. Rep. 6 (2016) 22699.
[102] E. Isarain-Chávez, M.D. Baró, C. Alcantara, S. Pané, J. Sort, E. Pellicer, ChemSusChem 11 (2018) 367–375.
[103] A.K. Ipadeola, A.B. Haruna, A.M. Abdullah, M.F. Shibl, D. Ahmadaliev, K. I. Ozoemena, K. Eid, Catal. Today 421 (2023) 114178.
[104] A. Kumar, Y. Kuang, Z. Liang, X. Sun, Mater. Today Nano 11 (2020) 100076.
[105] A.K. Ipadeola, K. Eid, A.M. Abdullah, K.I. Ozoemena, Langmuir 38 (2022) 11109–11120.
[106] F. Saleem, Z. Zhang, B. Xu, X. Xu, P. He, X. Wang, J. Am. Chem. Soc. 135 (2013) 18304–18307.
[107] P.P. Wang, H. Sun, Y. Ji, W. Li, X. Wang, Adv. Mater. 26 (2014) 964–969.
[108] W. Wang, N. Zhang, Z. Shi, Z. Ye, Q. Gao, M. Zhi, Z. Hong, Chem. Eng. J. 338 (2018) 55–61.
[109] Y. Bi, A. Nautiyal, H. Zhang, H. Yan, J. Luo, X. Zhang, Ceram. Int. 44 (2018) 5402–5410.
[110] J. Bashir, M.B. Chowdhury, R.R. Kathak, S. Dey, A.T. Tasnim, M.A. Amin, Y. V. Kaneti, M.K. Masud, M.S.A. Hossain, Mater. Adv. 4 (2023) 408–431.
[111] J. Kim, H. Kim, G.H. Han, S. Hong, J. Park, J. Bang, S.Y. Kim, S.H. Ahn, Exploration, Wiley Online Library, 2022, p. 20210077.
[112] D.V. Shinde, T.M. Kokumai, J. Buha, M. Prato, L. De Trizio, L. Manna, J. Mater. Chem. A 8 (2020) 10787–10795.
[113] H.-Y. Chiu, Y.-C. Liu, Y.-T. Hsieh, I.-W. Sun, ACS omega 2 (2017) 4911–4919.
[114] H. Kim, J. Kim, G.H. Han, W. Guo, S. Hong, J. Park, S.H. Ahn, J. Ind. Eng. Chem. 95 (2021) 357–366.
[115] X. Chia, N.A.A. Sutrisnoh, M. Pumera, ACS Appl. Mater. Interfaces 10 (2018) 8702–8711.
[116] Z. Zhongming, L. Linong, Y. Xiaona, Z. Wangqiang, L. Wei, Nat. Commun. 12 (2021) 3783.
[117] Z. Liu, R. Che, A.A. Elzatahry, D. Zhao, ACS Nano 8 (2014) 10455–10460.
[118] S. Zhu, N. Zhao, J. Li, X. Deng, J. Sha, C. He, Nano Today 29 (2019) 100796.
[119] L. Lu, R. Capek, A. Kornowski, N. Gaponik, A. Eychmüller, Angew. Chem. Int. Ed. 117 (2005) 6151–6155.
[120] J. Jiang, A. Kucernak, Electrochem. Commun. 11 (2009) 623–626.
[121] S. Fu, C. Zhu, Q. Shi, D. Du, Y. Lin, RSC Adv. 6 (2016) 69233–69238.
[122] S. Fu, C. Zhu, J. Song, M.H. Engelhard, H. Xia, D. Du, Y. Lin, ACS Appl. Mater. Interfaces 8 (2016) 35213–35218.
[123] X. Lu, M. Wu, Z. Lu, J. Hu, J. Xie, A. Hao, Y. Cao, J. Alloys Compd. 942 (2023) 169095.
[124] H. Wang, H.Y. Jeong, M. Imura, L. Wang, L. Radhakrishnan, N. Fujita, T. Castle, O. Terasaki, Y. Yamauchi, J. Am. Chem. Soc. 133 (2011) 14526–14529.
[125] C. Li, M. Iqbal, J. Lin, X. Luo, B. Jiang, V. Malgras, K.C.-W. Wu, J. Kim, Y. Yamauchi, Acc. Chem. Res. 51 (2018) 1764–1773.
[126] Y.-C. Liang, Y.-W. Juan, K.-T. Lu, U.-S. Jeng, S.-A. Chen, W.-T. Chuang, C.-J. Su, C.-L. Liu, C.-W. Pao, J.-F. Lee, J. Phys. Chem. C 116 (2012) 26649–26655.
[127] Y. Yamauchi, A. Takai, M. Komatsu, M. Sawada, T. Ohsuna, K. Kuroda, Chem. Mater. 20 (2008) 1004–1011.
[128] S. Butcha, S. Assavapanumat, S. Ittisanronnachai, V. Lapeyre, C. Wattanakit, A. Kuhn, Nat. Commun. 12 (2021) 1314.
[129] J. Dong, T. Sun, Y. Zhang, H. Zhang, S. Lu, D. Hu, J. Chen, L. Xu, J. Colloid Interface Sci. 599 (2021) 603–610.
[130] Y. Saadat, O.Q. Imran, C.O. Osuji, R. Foudazi, J. Mater. Chem. A 9 (2021) 21607–21658.
[131] Y. Kang, Y. Guo, J. Zhao, B. Jiang, J. Guo, Y. Tang, H. Li, V. Malgras, M.A. Amin, H. Nara, Small 18 (2022) 2203411.
[132] K. Kani, H. Lim, A.E. Whitten, K. Wood, A.J. Yago, M.S.A. Hossain, J. Henzie, J. Na, Y. Yamauchi, J. Mater. Chem. A 9 (2021) 2754–2763.
[133] J. McBain, Trans. Faraday Soc. 9 (1913) 99–101.
[134] S. Yin, H. Wang, K. Deng, Z. Dai, Z. Wang, Y. Xu, X. Li, H. Xue, L. Wang, Chem Eur J 25 (2019) 5316–5321.
[135] H. Wang, S. Ishihara, K. Ariga, Y. Yamauchi, J. Am. Chem. Soc. 134 (2012) 10819–10821.
[136] C. Li, H. Wang, Y. Yamauchi, Chem. Eur. J. 19 (2013) 2242–2246.
[137] H. Wang, M. Imura, Y. Nemoto, L. Wang, H.Y. Jeong, T. Yokoshima, O. Terasaki, Y. Yamauchi, Chem. Eur. J. 18 (2012) 13142–13148.
[138] G.-L. Li, X.-C. Xu, B.-B. Yang, S. Cao, X. Wang, X. Fu, Y. Shi, Y. Yan, X. Song, C. Hao, Electrochim. Acta 331 (2020) 135375.
[139] Y. Li, H. Yu, Z. Wang, S. Liu, Y. Xu, X. Li, L. Wang, H. Wang, Int. J. Hydrog. Energy 45 (2020) 5997–6005.
[140] K. Eid, H. Wang, P. He, K. Wang, T. Ahamad, S.M. Alshehri, Y. Yamauchi, L. Wang, Nanoscale 7 (2015) 16860–16866.
[141] L. Sun, H. Wang, K. Eid, L. Wang, Sci. Technol. Adv. Mater. 17 (2016) 58–62.
[142] K. Eid, H. Wang, V. Malgras, Z.A. Alothman, Y. Yamauchi, L. Wang, J. Phys. Chem. C 119 (2015) 19947–19953.
[143] K. Eid, V. Malgras, P. He, K. Wang, A. Aldalbahi, S.M. Alshehri, Y. Yamauchi, L. Wang, RSC Adv. 5 (2015) 31147–31152.
[144] K. Eid, H. Wang, V. Malgras, S.M. Alshehri, T. Ahamad, Y. Yamauchi, L. Wang, J. Electroanal. Chem. 779 (2016) 250–255.
[145] K. Eid, H. Wang, V. Malgras, Z.A. Alothman, Y. Yamauchi, L. Wang, Chem. Eur. J. 11 (2016) 1388–1393.
[146] K. Eid, J. Electroanal. Chem. 961 (2024) 118207.
[147] H.-Y. Hsueh, C.-T. Yao, R.-M. Ho, Chem. Soc. Rev. 44 (2015) 1974–2018.
[148] T.H. Epps III, R.K. O'Reilly, Chem. Sci. 7 (2016) 1674–1689.
[149] H.Y. Hsueh, H.Y. Chen, Y.C. Hung, Y.C. Ling, S. Gwo, R.M. Ho, Adv. Mater. 25 (2013) 1780–1786.
[150] M. Park, C. Harrison, P.M. Chaikin, R.A. Register, D.H. Adamson, Science 276 (1997) 1401–1404.
[151] B.-H. Sohn, J.-M. Choi, S.I. Yoo, S.-H. Yun, W.-C. Zin, J.C. Jung, M. Kanehara, T. Hirata, T. Teranishi, J. Am. Chem. Soc. 125 (2003) 6368–6369.
[152] J.-J. Duan, X.-X. Zheng, H.-J. Niu, J.-J. Feng, Q.-L. Zhang, H. Huang, A.-J. Wang, J. Colloid Interface Sci. 560 (2020) 467–474.
[153] Y. Chen, A.-J. Wang, P.-X. Yuan, X. Luo, Y. Xue, J.-J. Feng, Biosens. Bioelectron. 132 (2019) 294–301.
[154] Y.-C. Shi, A.-J. Wang, P.-X. Yuan, L. Zhang, X. Luo, J.-J. Feng, Biosens. Bioelectron. 111 (2018) 47–51.
[155] A.S. Nugraha, V. Malgras, J. Kim, J. Bo, C. Li, M. Iqbal, Y. Yamauchi, T. Asahi, Small Meth. 2 (2018) 1800283.
[156] W. Menezes, V. Zielasek, K. Thiel, A. Hartwig, M. Bäumer, J. Catal. 299 (2013) 222–231.
[157] K. Mikkelsen, B. Cassidy, N. Hofstetter, L. Bergquist, A. Taylor, D.A. Rider, Chem. Mater. 26 (2014) 6928–6940.
[158] M. Aizawa, J.M. Buriak, J. Am. Chem. Soc. 128 (2006) 5877–5886.
[159] H. Wang, S. Yin, K. Eid, Y. Li, Y. Xu, X. Li, H. Xue, L. Wang, A.C.S. Sustain, Chem. Eng. 6 (2018) 11768–11774.
[160] A.K. Taylor, D.S. Perez, X. Zhang, B.K. Pilapil, M.H. Engelhard, B.D. Gates, D. A. Rider, J. Mater. Chem. A 5 (2017) 21514–21527.
[161] A.A. Ensafi, M. Jafari-Asl, B. Rezaei, Phys. Chem. Chem. Phys. 17 (2015) 23770–23782.
[162] S. Bai, C. Wang, M. Deng, M. Gong, Y. Bai, J. Jiang, Y. Xiong, Angew. Chem. Int. Ed. 53 (2014) 12120–12124.
[163] Y. Liu, S. Liu, Z. Che, S. Zhao, X. Sheng, M. Han, J. Bao, J. Mater. Chem. A 4 (2016) 16690–16697.
[164] J.-J. Feng, L. Liu, X. Ma, J. Yuan, A.-J. Wang, Int. J. Hydrog. Energy 42 (2017) 2071–2080.
[165] Z. Xing, C. Han, D. Wang, Q. Li, X. Yang, ACS Catal. 7 (2017) 7131–7135.
[166] X. Weng, Q. Liu, A.-J. Wang, J. Yuan, J.-J. Feng, J. Colloid Interface Sci. 494 (2017) 15–21.
[167] S.-S. Chen, L.-J. Nan, J.-J. Feng, L. Zhang, K.-M. Fang, X. Luo, A.-J. Wang, Int. J. Hydrog. Energy 43 (2018) 6096–6106.
[168] B. Cui, B. Hu, J. Liu, M. Wang, Y. Song, K. Tian, Z. Zhang, L. He, ACS Appl. Mater. Interfaces 10 (2018) 23858–23873.
[169] J. Li, L. Liu, Y. Ai, Z. Hu, L. Xie, H. Bao, J. Wu, H. Tian, R. Guo, S. Ren, Chem. Eur. J. 25 (2019) 7191–7200.
[170] H.-Y. Chen, M.-X. Jin, L. Zhang, A.-J. Wang, J. Yuan, Q.-L. Zhang, J.-J. Feng, J. Colloid Interface Sci. 543 (2019) 1–8.
[171] B. Sarkar, D. Das, K.K. Nanda, Green Chem. 22 (2020) 7884–7895.
[172] Y. Qin, X. Han, S. Gadipelli, J. Guo, S. Wu, L. Kang, J. Callison, Z. Guo, J. Mater. Chem. A 7 (2019) 6543–6551.
[173] J. Yin, Q. Fan, Y. Li, F. Cheng, P. Zhou, P. Xi, S. Sun, J. Am. Chem. Soc. 138 (2016) 14546–14549.
[174] X. Zhang, Z. Luo, P. Yu, Y. Cai, Y. Du, D. Wu, S. Gao, C. Tan, Z. Li, M. Ren, Nat. Catal. 1 (2018) 460–468.
[175] H. Yu, Z. Wang, Z. Dai, Q. Mao, Y. Xu, X. Li, L. Wang, H. Wang, Sustain. Energy Fuel 4 (2020) 4878–4883.
[176] B.T. Jebaslinhepzybai, N. Prabu, M. Sasidharan, Int. J. Hydrog. Energy 45 (2020) 11127–11137.
[177] H. Zhang, X. Guo, W. Liu, D. Wu, D. Cao, D. Cheng, J. Colloid Interface Sci. 629 (2023) 53–62.
[178] R. Nivetha, K. Gothandapani, V. Raghavan, Q. Van Le, S. Pitchaimuthu, M. Muthuramamoorty, S. Pandiaraj, A. Alodhayb, S. Kwan Jeong, A. Nirmala Grace, ChemCatChem 13 (2021) 4342–4349.

[179] M. Xu, X. Chen, C. Li, T. Wang, Y. Zeng, S. Mu, J. Yu, Energy Fuel 35 (2021) 17861–17868.
[180] X. Fan, H. Zhou, X. Guo, ACS Nano 9 (2015) 5125–5134.
[181] J. Yang, G. Ning, L. Yu, Y. Wang, C. Luan, A. Fan, X. Zhang, Y. Liu, Y. Dong, X. Dai, J. Mater. Chem. A 7 (2019) 17790–17796.
[182] S. Sarkar, U. Subbarao, S.C. Peter, J. Mater. Chem. A 5 (2017) 15950–15960.
[183] W. Xu, S. Zhu, Y. Liang, Z. Cui, X. Yang, A. Inoue, H. Wang, J. Mater. Chem. A 5 (2017) 18793–18800.
[184] J. Chen, J. Chen, D. Yu, M. Zhang, H. Zhu, M. Du, Electrochim. Acta 246 (2017) 17–26.
[185] X.-X. Lin, A.-J. Wang, K.-M. Fang, J. Yuan, J.-J. Feng, A.C.S. Sustain, Chem. Eng. 5 (2017) 8675–8683.
[186] C. Ray, S. Dutta, Y. Negishi, T. Pal, Chem. Commun. 52 (2016) 6095–6098.
[187] T. Li, R. Wang, M. Yang, S. Zhao, Z. Li, J. Miao, Z.-D. Gao, Y. Gao, Y.-Y. Song, Sustain. Energy Fuel 4 (2020) 380–386.
[188] J. Tian, W. Wu, Z. Tang, Y. Wu, R. Burns, B. Tichnell, Z. Liu, S. Chen, Catalysts 8 (2018) 329.
[189] E. Chiani, S.N. Azizi, S. Ghasemi, Int. J. Hydrog. Energy 46 (2021) 25468–25485.
[190] D. Jin, A. Yu, Y. Lee, M.H. Kim, C. Lee, J. Mater. Chem. A 8 (2020) 8629–8637.
[191] H. Qi, X. Guan, G. Lei, M. Zhao, H. He, K. Li, G. Zhang, F. Zhang, X. Fan, W. Peng, Nanomaterials 11 (2021) 1228.
[192] Y. Gao, Y. Xue, T. Liu, Y. Liu, C. Zhang, C. Xing, F. He, Y. Li, Adv. Sci. 8 (2021) 2102777.
[193] Y. Zhu, H.A. Tahini, Z. Hu, J. Dai, Y. Chen, H. Sun, W. Zhou, M. Liu, S.C. Smith, H. Wang, Nat. Commun. 10 (2019) 149.
[194] Z. Kang, H. Guo, J. Wu, X. Sun, Z. Zhang, Q. Liao, S. Zhang, H. Si, P. Wu, L. Wang, Adv. Funct. Mater. 29 (2019) 1807031.
[195] D. Li, X. Chen, Y. Lv, G. Zhang, Y. Huang, W. Liu, Y. Li, R. Chen, C. Nuckolls, H. Ni, Appl. Catal. B Environ. 269 (2020) 118824.
[196] T. Qiu, J. Cheng, Z. Liang, H. Tabassum, J. Shi, Y. Tang, W. Guo, L. Zheng, S. Gao, S. Xu, Appl. Catal. B Environ. 316 (2022) 121626.
[197] W. Wu, J. Liu, N. Johannes, Int. J. Hydrog. Energy 46 (2021) 609–621.
[198] M. Yang, L. Jiao, H. Dong, L. Zhou, C. Teng, D. Yan, T.-N. Ye, X. Chen, Y. Liu, H.-L. Jiang, Sci. Bull. 66 (2021) 257–264.
[199] C. Li, H. Jang, S. Liu, M.G. Kim, L. Hou, X. Liu, J. Cho, Adv. Energy Mater. 12 (2022) 2200029.
[200] W.F. Chen, K. Sasaki, C. Ma, A.I. Frenkel, N. Marinkovic, J.T. Muckerman, Y. Zhu, R.R. Adzic, Angew. Chem. Int. Ed. 51 (2012) 6131–6135.
[201] B. Cao, G.M. Veith, J.C. Neuefeind, R.R. Adzic, P.G. Khalifah, J. Am. Chem. Soc. 135 (2013) 19186–19192.
[202] Q. Lu, G.S. Hutchings, W. Yu, Y. Zhou, R.V. Forest, R. Tao, J. Rosen, B. T. Yonemoto, Z. Cao, H. Zheng, Nat. Commun. 6 (2015) 6567.
[203] X. Jia, Y. Zhao, G. Chen, L. Shang, R. Shi, X. Kang, G.I. Waterhouse, L.Z. Wu, C. H. Tung, T. Zhang, Adv. Energy Mater. 6 (2016).
[204] X. Li, L. Yang, T. Su, X. Wang, C. Sun, Z. Su, J. Mater. Chem. A 5 (2017) 5000–5006.
[205] C. He, J. Tao, J. Catal. 347 (2017) 63–71.
[206] M.Y. Zu, P.F. Liu, C. Wang, Y. Wang, L.R. Zheng, B. Zhang, H. Zhao, H.G. Yang, ACS Energy Lett. 3 (2017) 78–84.
[207] Y.-Q. Wang, L. Zhao, X.-L. Sui, D.-M. Gu, Z.-B. Wang, Ceram. Int. 45 (2019) 17128–17136.
[208] C. Qin, A. Fan, X. Zhang, S. Wang, X. Yuan, X. Dai, J. Mater. Chem. A 7 (2019) 27594–27602.
[209] X. Li, X. Wang, J. Zhou, L. Han, C. Sun, Q. Wang, Z. Su, J. Mater. Chem. A 6 (2018) 5789–5796.
[210] D. Jiang, Y. Xu, R. Yang, D. Li, S. Meng, M. Chen, A.C.S. Sustain, Chem. Eng. 7 (2019) 9309–9317.
[211] S. Chen, F. Bi, K. Xiang, Y. Zhang, P. Hao, M. Li, B. Zhao, X. Guo, ACS Sustain. Chem. Eng. 7 (2019) 15278–15288.
[212] A. Sivanantham, P. Ganesan, S. Shanmugam, Adv. Funct. Mater. 26 (2016) 4661–4672.
[213] D. Wu, Q. Xu, J. Qian, X. Li, Y. Sun, Chem. Eur. J. 25 (2019) 3105–3111.
[214] R. Wang, Q. Yuan, P. Sun, R. Nie, X. Wang, J. Alloys Compd. 789 (2019) 100–107.
[215] F. Kong, X. Fan, A. Kong, Z. Zhou, X. Zhang, Y. Shan, Adv. Funct. Mater. 28 (2018) 1803973.
[216] C.C. Yang, S.F. Zai, Y.T. Zhou, L. Du, Q. Jiang, Adv. Funct. Mater. 29 (2019) 1901949.
[217] M. Hou, R. Lan, Z. Hu, Z. Chen, Nanoscale 11 (2019) 17093–17103.
[218] J. Luo, W.H. Guo, Q. Zhang, X.H. Wang, L. Shen, H.C. Fu, L.L. Wu, X.H. Chen, H. Q. Luo, N.B. Li, Nanoscale 12 (2020) 19992–20001.
[219] J. Chen, B. Ren, H. Cui, C. Wang, Small 16 (2020) 1907556.
[220] F. Han, S. Yun, J. Shi, Y. Zhang, Y. Si, C. Wang, N. Zafar, J. Li, X. Qiao, Appl. Catal. B Environ. 273 (2020) 119004.
[221] C. He, J. Tao, Mater. Today Energy 8 (2018) 65–72.
[222] M. Li, Y. Zhu, H. Wang, C. Wang, N. Pinna, X. Lu, Adv. Energy Mater. 9 (2019) 1803185.
[223] Y. Liu, G.-D. Li, L. Yuan, L. Ge, H. Ding, D. Wang, X. Zou, Nanoscale 7 (2015) 3130–3136.
[224] Q.-Q. Pan, C.-Y. Xu, X. Li, J.-F. Zhang, X.-L. Hu, Y. Geng, Z.-M. Su, Chem. Eng. J. 405 (2021) 126962.
[225] L. Lei, D. Huang, Y. Chen, S. Chen, R. Deng, J. Mater. Chem. A 9 (2021) 8730–8739.
[226] S.M. El-Refaei, P.A. Russo, P. Amsalem, N. Koch, N. Pinna, ACS Appl. Nano Mater. 3 (2020) 4147–4156.
[227] J. Chen, G. Liu, Y.-Z. Zhu, M. Su, P. Yin, X.-J. Wu, Q. Lu, C. Tan, M. Zhao, Z. Liu, J. Am. Chem. Soc. 142 (2020) 7161–7167.
[228] S.-F. Hung, Y. Zhu, G.-Q. Tzeng, H.-C. Chen, C.-S. Hsu, Y.-F. Liao, H. Ishii, N. Hiraoka, H.M. Chen, ACS Energy Lett. 4 (2019) 2813–2820.
[229] J. Wan, Z. Zhao, H. Shang, B. Peng, W. Chen, J. Pei, L. Zheng, J. Dong, R. Cao, R. Sarangi, J. Am. Chem. Soc. 142 (2020) 8431–8439.
[230] M. Kim, M.A.R. Anjum, M. Choi, H.Y. Jeong, S.H. Choi, N. Park, J.S. Lee, Adv. Funct. Mater. 30 (2020) 2002536.
[231] Y. Guo, J. Tang, J. Henzie, B. Jiang, W. Xia, T. Chen, Y. Bando, Y.-M. Kang, M.S. A. Hossain, Y. Sugahara, ACS Nano 14 (2020) 4141–4152.
[232] T. Li, G. Luo, Q. Liu, S. Li, Y. Zhang, L. Xu, Y. Tang, J. Yang, H. Pang, Chem. Eng. J. 410 (2021) 128325.
[233] J. Song, C. Zhu, B.Z. Xu, S. Fu, M.H. Engelhard, R. Ye, D. Du, S.P. Beckman, Y. Lin, Adv. Energy Mater. 7 (2017) 1601555.
[234] J. Luo, J.-H. Im, M.T. Mayer, M. Schreier, M.K. Nazeeruddin, N.-G. Park, S. D. Tilley, H.J. Fan, M. Grätzel, Science 345 (2014) 1593–1596.
[235] W. Ma, R. Ma, C. Wang, J. Liang, X. Liu, K. Zhou, T. Sasaki, ACS Nano 9 (2015) 1977–1984.
[236] A. Kumar, S. Bhattacharyya, ACS Appl. Mater. Interfaces 9 (2017) 41906–41915.
[237] T. Li, S. Li, Q. Liu, J. Yin, D. Sun, M. Zhang, L. Xu, Y. Tang, Y. Zhang, Adv. Sci. 7 (2020) 1902371.
[238] Z. Huang, J. Liu, Z. Xiao, H. Fu, W. Fan, B. Xu, B. Dong, D. Liu, F. Dai, D. Sun, Nanoscale 10 (2018) 22758–22765.
[239] Y. Yang, Z. Lin, S. Gao, J. Su, Z. Lun, G. Xia, J. Chen, R. Zhang, Q. Chen, ACS Catal. 7 (2017) 469–479.
[240] C. Xu, F. Wu, X. Yang, K. Feng, M. Zhang, Y. Wang, L. Yang, N. Jiang, S. Yin, J. Alloys Compd. 920 (2022) 165826.
[241] Z.W. Seh, K.D. Fredrickson, B. Anasori, J. Kibsgaard, A.L. Strickler, M. R. Lukatskaya, Y. Gogotsi, T.F. Jaramillo, A. Vojvodic, ACS Energy Lett. 1 (2016) 589–594.
[242] J. Liu, Y. Liu, D. Xu, Y. Zhu, W. Peng, Y. Li, F. Zhang, X. Fan, Appl. Catal. B Environ. 241 (2019) 89–94.
[243] Y.-Y. Ma, C.-X. Wu, X.-J. Feng, H.-Q. Tan, L.-K. Yan, Y. Liu, Z.-H. Kang, E.-B. Wang, Y.-G. Li, Energy Environ. Sci. 10 (2017) 788–798.
[244] Y. Luo, L. Tang, U. Khan, Q. Yu, H.-M. Cheng, X. Zou, B. Liu, Nat. Commun. 10 (2019) 269.
[245] X. Xu, F. Nosheen, X. Wang, Chem. Mater. 28 (2016) 6313–6320.
[246] F. Yu, Y. Gao, Z. Lang, Y. Ma, L. Yin, J. Du, H. Tan, Y. Wang, Y. Li, Nanoscale 10 (2018) 6080–6087.
[247] T. Liu, P. Li, N. Yao, G. Cheng, S. Chen, W. Luo, Y. Yin, Angew. Chem. Int. Ed. 131 (2019) 4727–4732.
[248] C. Huang, X. Miao, C. Pi, B. Gao, X. Zhang, P. Qin, K. Huo, X. Peng, P.K. Chu, Nano Energy 60 (2019) 520–526.
[249] Y.-H. Chang, C.-T. Lin, T.-Y. Chen, C.-L. Hsu, Y.-H. Lee, W. Zhang, K.-H. Wei, L.-J. Li, Adv. Mater. 25 (2013) 756–760.
[250] J. Zhang, X. Meng, J. Zhao, Z. Zhu, ChemCatChem 6 (2014) 2059–2064.
[251] J. Jiang, Q. Liu, C. Zeng, L. Ai, J. Mater. Chem. A 5 (2017) 16929–16935.
[252] C. Chen, A. Wu, H. Yan, Y. Xiao, C. Tian, H. Fu, Chem. Sci. 9 (2018) 4746–4755.
[253] Y. Wang, W. Wu, Y. Rao, Z. Li, N. Tsubaki, M. Wu, J. Mater. Chem. A 5 (2017) 6170–6177.
[254] M.A. Ahsan, A.R. Puente Santiago, Y. Hong, N. Zhang, M. Cano, E. Rodriguez-Castellon, L. Echegoyen, S.T. Sreenivasan, J.C. Noveron, J. Am. Chem. Soc. 142 (2020) 14688–14701.
[255] S. Li, Z. Yang, Z. Liu, Y. Ma, Y. Gu, L. Zhao, Q. Zhou, W. Xu, J. Colloid Interface Sci. 592 (2021) 349–357.
[256] P. Li, D. Zheng, M. Gao, X. Zuo, L. Sun, Q. Zhou, J. Lin, ACS Appl. Energy Mater. 4 (2021) 8875–8882.
[257] Y. Zhang, S. Yun, X. Qiao, M. Sun, J. Dang, C. Dang, J. Yang, J. Alloys Compd. 893 (2022) 162349.
[258] P. Zhang, T. Zhan, H. Rong, Y. Feng, Y. Wen, J. Zhao, L. Wang, X. Liu, W. Hou, J. Colloid Interface Sci. 579 (2020) 1–11.
[259] A. Arshad, S. Yun, J. Shi, M. Sun, N. Zafar, A. Hagfeldt, Chem. Eng. J. 435 (2022) 134913.
[260] Y. Guo, Q. Huang, J. Ding, L. Zhong, T.-T. Li, Y. Hu, J. Qian, S. Huang, Int. J. Hydrog. Energy 46 (2021) 2182–2190.
[261] Z. Zhang, H. Wang, Y. Li, M. Xie, C. Li, H. Lu, Y. Peng, Z. Shi, Chem. Res. Chin. Univ. (2022) 1–8.
[262] Z. Weng, W. Liu, L.-C. Yin, R. Fang, M. Li, E.I. Altman, Q. Fan, F. Li, H.-M. Cheng, H. Wang, Nano Lett. 15 (2015) 7704–7710.
[263] K. Zhang, Y. Zhao, D. Fu, Y. Chen, J. Mater. Chem. A 3 (2015) 5783–5788.
[264] J. Wang, H.-X. Zhong, Z.-L. Wang, F.-L. Meng, X.-B. Zhang, ACS Nano 10 (2016) 2342–2348.
[265] J.A. Vigil, T.N. Lambert, B.T. Christensen, J. Mater. Chem. A 4 (2016) 7549–7554.
[266] Y. Tang, W. Li, L. Jiao, F. Li, Y. Yang, X. Wang, W. Gao, R. Li, New J. Chem. 41 (2017) 12956–12961.
[267] A. Majeed, X. Li, P.-X. Hou, H. Tabassum, L. Zhang, C. Liu, H.-M. Cheng, Appl. Catal. B Environ. 269 (2020) 118823.
[268] Q. Yuan, Y. Yu, P.C. Sherrell, J. Chen, X. Bi, Chem. Asian J. 15 (2020) 1728–1735.
[269] V. Elayappan, R. Shanmugam, S. Chinnusamy, D.J. Yoo, G. Mayakrishnan, K. Kim, H.S. Noh, M.K. Kim, H. Lee, Appl. Surf. Sci. 505 (2020) 144642.
[270] F. Aftab, H. Duran, K. Kirchhoff, M. Zaheer, B. Iqbal, M. Saleem, S.N. Arshad, ChemCatChem 12 (2020) 932–943.
[271] Q. Qin, P. Li, L. Chen, X. Liu, ACS Appl. Mater. Interfaces 10 (2018) 39828–39838.
[272] J. Zhu, W. Tu, Z. Bai, H. Pan, P. Ji, H. Zhang, Z. Deng, H. Zhang, Electrochim. Acta 323 (2019) 134821.
[273] Y. Li, B. Huang, Y. Sun, M. Luo, Y. Yang, Y. Qin, L. Wang, C. Li, F. Lv, W. Zhang, Small 15 (2019) 1804212.

[274] J. Sun, J. Liu, H. Chen, X. Han, Y. Wu, J. He, C. Han, G. Yang, Y. Shan, J. Colloid Interface Sci. 558 (2020) 100–105.
[275] S. Wang, J. Wang, X. Wang, L. Li, J. Qin, M. Cao, J. Energy Chem. 53 (2021) 422–432.
[276] L. Jia, P. Wagner, J. Chen, Inorganics 10 (2022) 53.
[277] B. Salah, A. Abdelgawad, J.K. El-Demellawi, Q. Lu, Z. Xia, A.M. Abdullah, K. Eid, ACS Appl. Mater. Interfaces 16 (2024) 18768–18781.
[278] Y. Yuan, S. Adimi, T. Thomas, J. Wang, H. Guo, J. Chen, J.P. Attfield, F.J. DiSalvo, M. Yang, Innovation 2 (2021) 100096.
[279] P. Yang, X. Ge, L. Fan, M. Li, L. Zhang, X. Li, Z. Kang, H. Guo, F. Dai, D. Sun, J. Solid State Chem. 292 (2020) 121696.
[280] M.R. Rizk, M.G. Abd El-Moghny, A. Mazhar, M.S. El-Deab, B. El-Anadouli, Sustain. Energy Fuel 5 (2021) 986–994.
[281] C. Yu, J. Lu, L. Luo, F. Xu, P.K. Shen, P. Tsiakaras, S. Yin, Electrochim. Acta 301 (2019) 449–457.
[282] J. Liu, Y. Yang, B. Ni, H. Li, X. Wang, Small 13 (2017) 1602637.
[283] S. Hu, H. Wu, C. Feng, Y. Ding, Int. J. Hydrog. Energy 45 (2020) 21040–21050.
[284] K.C. Majhi, M. Yadav, Int. J. Hydrog. Energy 45 (2020) 24219–24231.
[285] L. Chang, Z. Sun, Y.H. Hu, Electrochem. Energy Rev. 4 (2021) 194–218.
[286] S. Tang, X. Li, M. Courté, J. Peng, D. Fichou, Inorg. Chem. Front. 7 (2020) 2241–2247.
[287] Z. Huang, Z. Yang, Q. Jia, N. Wang, Y. Zhu, Y. Xia, Nanoscale 14 (2022) 4726–4739.
[288] B. Wang, Z. Wang, X. Wang, B. Zheng, W. Zhang, Y. Chen, J. Mater. Chem. A 6 (2018) 12701–12707.
[289] M. Hassan, M.M. Baig, K.H. Shah, A. Hussain, S.A. Hassan, A. Ali, J. Phys. Chem. Solids 167 (2022) 110780.
[290] H. Zhu, J. Zhang, R. Yanzhang, M. Du, Q. Wang, G. Gao, J. Wu, G. Wu, M. Zhang, B. Liu, Adv. Mater. 27 (2015) 4752–4759.
[291] M.S. Faber, R. Dziedzic, M.A. Lukowski, N.S. Kaiser, Q. Ding, S. Jin, J. Am. Chem. Soc. 136 (2014) 10053–10061.
[292] X. Liu, W. Liu, M. Ko, M. Park, M.G. Kim, P. Oh, S. Chae, S. Park, A. Casimir, G. Wu, Adv. Funct. Mater. 25 (2015) 5799–5808.
[293] Z. Huang, Z. Yang, M.Z. Hussain, B. Chen, Q. Jia, Y. Zhu, Y. Xia, Electrochim. Acta 330 (2020) 135335.
[294] Z. Huang, Z. Yang, M.Z. Hussain, Q. Jia, Y. Zhu, Y. Xia, J. Mater. Sci. Technol. 84 (2021) 76–85.
[295] W. Zhang, H. Zhang, R. Luo, M. Zhang, X. Yan, X. Sun, J. Shen, W. Han, L. Wang, J. Li, J. Colloid Interface Sci. 548 (2019) 48–55.
[296] R. Xu, R. Wu, Y. Shi, J. Zhang, B. Zhang, Nano Energy 24 (2016) 103–110.
[297] X. Xu, H. Liang, F. Ming, Z. Qi, Y. Xie, Z. Wang, ACS Catal. 7 (2017) 6394–6399.
[298] S. Kim, K. Min, H. Kim, R. Yoo, S.E. Shim, D. Lim, S.-H. Baeck, Int. J. Hydrog. Energy 47 (2022) 8165–8176.
[299] Y. Cao, Y. Meng, S. Huang, S. He, X. Li, S. Tong, M. Wu, ACS Sustain. Chem. Eng. 6 (2018) 15582–15590.
[300] X. Tang, J.-Y. Zhang, B. Mei, X. Zhang, Y. Liu, J. Wang, W. Li, Chem. Eng. J. 404 (2021) 126529.
[301] L. Huang, L. Xu, Y. Yang, H. Yu, H. Tao, D. Li, X. Dong, J. Mater. Sci. Mater. Electron. 31 (2020) 6607–6617.
[302] X. Shang, J.-F. Qin, J.-H. Lin, B. Dong, J.-Q. Chi, Z.-Z. Liu, L. Wang, Y.-M. Chai, C.-G. Liu, J. Colloid Interface Sci. 523 (2018) 121–132.
[303] W. Zhu, M. Ren, N. Hu, W. Zhang, Z. Luo, R. Wang, J. Wang, L. Huang, Y. Suo, J. Wang, ACS Sustain. Chem. Eng. 6 (2018) 5011–5020.
[304] L.-L. Feng, G. Yu, Y. Wu, G.-D. Li, H. Li, Y. Sun, T. Asefa, W. Chen, X. Zou, J. Am. Chem. Soc. 137 (2015) 14023–14026.
[305] C. Guan, X. Liu, A.M. Elshahawy, H. Zhang, H. Wu, S.J. Pennycook, J. Wang, Nanoscale Horiz. 2 (2017) 342–348.
[306] Q. Zhang, C. Ye, X.L. Li, Y.H. Deng, B.X. Tao, W. Xiao, L.J. Li, N.B. Li, H.Q. Luo, ACS Appl. Mater. Interfaces 10 (2018) 27723–27733.
[307] Y. Liu, X. Hua, C. Xiao, T. Zhou, P. Huang, Z. Guo, B. Pan, Y. Xie, J. Am. Chem. Soc. 138 (2016) 5087–5092.
[308] Y. Yang, K. Zhang, H. Lin, X. Li, H.C. Chan, L. Yang, Q. Gao, ACS Catal. 7 (2017) 2357–2366.
[309] Y. Fan, D. Wang, D. Han, Y. Ma, S. Ni, Z. Sun, X. Dong, L. Niu, Nanoscale 9 (2017) 5887–5895.
[310] K. Liu, F. Wang, K. Xu, T.A. Shifa, Z. Cheng, X. Zhan, J. He, Nanoscale 8 (2016) 4699–4704.
[311] S. Liu, Y. Jiang, M. Yang, M. Zhang, Q. Guo, W. Shen, R. He, M. Li, Nanoscale 11 (2019) 7959–7966.
[312] Z. Ma, H. Meng, M. Wang, B. Tang, J. Li, X. Wang, ChemElectroChem 5 (2018) 335–342.
[313] Y. Guo, Y. Liu, Y. Liu, C. Zhang, K. Jia, J. Su, K. Wang, Catalysts 12 (2022) 739.
[314] J. Zhou, Y. Dou, T. He, A. Zhou, X.-J. Kong, X.-Q. Wu, T. Liu, J.-R. Li, Nano Res. 14 (2021) 4548–4555.
[315] Y. Lin, M. Liu, Y. Pan, J. Zhang, J. Mater. Sci. 52 (2017) 10406–10417.
[316] H. Huang, A. Cho, S. Kim, H. Jun, A. Lee, J.W. Han, J. Lee, Adv. Funct. Mater. 30 (2020) 2003889.
[317] G. Cho, Y. Park, H. Kang, Y.-K. Hong, T. Lee, D.-H. Ha, Appl. Surf. Sci. 510 (2020) 145427.
[318] H. Yan, X. Xiao, X. Liu, Y. Song, Int. J. Hydrog. Energy 47 (2022) 23230–23239.
[319] L.M. Cao, Y.W. Hu, S.F. Tang, A. Iljin, J.W. Wang, Z.M. Zhang, T.B. Lu, Adv. Sci. 5 (2018) 1800949.
[320] Y. Wu, Y. Wang, Z. Wang, X. Li, J. Mater. Chem. A 9 (2021) 23574–23581.
[321] T. Chen, M. Qian, X. Tong, W. Liao, Y. Fu, H. Dai, Q. Yang, Int. J. Hydrog. Energy 46 (2021) 29889–29895.
[322] A. Muthurasu, G.P. Ojha, M. Lee, H.Y. Kim, J. Phys. Chem. C 124 (2020) 14465–14476.
[323] Y. Liu, Q. Wang, L. Wu, Y. Long, J. Li, S. Song, H. Zhang, Cryst. Growth Des. 18 (2018) 3404–3410.
[324] Y.-N. Wang, Z.-J. Yang, D.-H. Yang, L. Zhao, X.-R. Shi, G. Yang, B.-H. Han, ACS Appl. Mater. Interfaces 13 (2021) 8832–8843.
[325] N. Suo, X. Han, C. Chen, X. He, Z. Dou, Z. Lin, L. Cui, J. Xiang, Electrochim. Acta 333 (2020) 135531.
[326] C. Zhang, D. Li, Y. Xu, J. Mater. Res. 37 (2022) 807–817.
[327] C. Zhao, F. Wei, H. Lv, D. Zhao, N. Wang, L. Li, N. Li, X. Wang, Materials 14 (2021) 1473.
[328] X. Zhang, C. Sun, S. Xu, M. Huang, Y. Wen, X.-R. Shi, Nano Res. 15 (2022) 8897–8907.
[329] S. Li, L. Bai, H. Shi, X. Hao, L. Chen, Z. Ma, X. Qin, G. Shao, Int. J. Hydrog. Energy 46 (2021) 27883–27890.
[330] S. Maity, D.K. Singh, D. Bhutani, S. Prasad, U.V. Waghmare, S. Sampath, E. Muthusamy, Mater. Res. Bull. 140 (2021) 111312.
[331] X. Lv, X. Li, C. Yang, X. Ding, Y. Zhang, Y.Z. Zheng, S. Li, X. Sun, X. Tao, Adv. Funct. Mater. 30 (2020) 1910830.
[332] Y. Zhao, J. Zhang, Y. Xie, B. Sun, J. Jiang, W.-J. Jiang, S. Xi, H.Y. Yang, K. Yan, S. Wang, Nano Lett. 21 (2021) 823–832.
[333] Y. Tan, J. Feng, L. Kang, L. Liu, F. Zhao, S. Zhao, D.J. Brett, P.R. Shearing, G. He, I. P. Parkin, Energy Environ.Mater. 6 (2023) 12398.
[334] Z. Hou, Y. Zhu, W. Du, X. Jia, T. Huang, K.-J. Huang, J. Ind. Eng. Chem. 112 (2022) 85–95.
[335] L. Yang, L. Zhang, Appl. Catal. B Environ. 259 (2019) 118053.
[336] L. Zhu, Y. Huang, B. Wang, Y. Zhang, R. Zou, L. Yan, W. Sun, J. Solid State Electrochem. (2022) 1–11.
[337] D.T. Tran, H.T. Le, N.H. Kim, J.H. Lee, Appl. Catal. B Environ. 253 (2019) 235–245.
[338] T. Sun, S. Zhang, L. Xu, D. Wang, Y. Li, Chem. Commun. 54 (2018) 12101–12104.
[339] X. Liu, S. Deng, D. Xiao, M. Gong, J. Liang, T. Zhao, T. Shen, D. Wang, ACS Appl. Mater. Interfaces 11 (2019) 42233–42242.
[340] H. Zhao, Y. Wang, L. Fang, W. Fu, X. Yang, S. You, P. Luo, H. Zhang, Y. Wang, J. Mater. Chem. A 7 (2019) 20357–20368.
[341] X. Xu, T. Wang, C. Zhao, Z. Huang, M. Zheng, R. Jia, Y. Liu, Microporous Mesoporous Mater. 312 (2021) 110760.
[342] C. Du, M. Shang, J. Mao, W. Song, J. Mater. Chem. A 5 (2017) 15940–15949.
[343] X. Gao, K. Lu, J. Chen, J. Min, D. Zhu, M. Tan, Int. J. Hydrog. Energy 46 (2021) 23205–23213.
[344] J.-T. Ren, Y.-S. Wang, L. Chen, L.-J. Gao, W.-W. Tian, Z.-Y. Yuan, Chem. Eng. J. 389 (2020) 124408.
[345] D. Jiang, W. Ma, R. Yang, B. Quan, D. Li, S. Meng, M. Chen, Electrochim. Acta 329 (2020) 135121.
[346] B. Qu, M. Wei, X. Lu, J. Zhu, ChemistrySelect 6 (2021) 12926–12933.
[347] S.M. Kang, M. Kim, J.B. Lee, S. Xu, N.C.S. Selvam, P.J. Yoo, Nanoscale 13 (2021) 12854–12864.
[348] J. Huo, Y. Chen, Y. Liu, J. Guo, L. Lu, W. Li, Y. Wang, H. Liu, Sustain. Mater. Technol. 22 (2019) e00117.
[349] X. Wang, B. Wang, Y. Chen, M. Wang, Q. Wu, K. Srinivas, B. Yu, X. Zhang, F. Ma, W. Zhang, J. Mater. Sci. Technol. 105 (2022) 266–273.
[350] D. Guo, D. Duan, J. Gao, X. Zhou, S. Liu, Y. Wang, Int. J. Hydrog. Energy 47 (2022) 6620–6630.
[351] J. Li, H. Zheng, C. Xu, Z. Su, X. Li, J. Sun, Inorg. Chem. 60 (2021) 1624–1630.
[352] J. Li, Y. Liu, X. Li, Q. Pan, D. Sun, L. Men, B. Sun, C. Xu, Z. Su, Chem. Eng. J. 431 (2022) 133696.
[353] Y.-J. Tang, Y. Chen, H.-J. Zhu, A.-M. Zhang, X.-L. Wang, L.-Z. Dong, S.-L. Li, Q. Xu, Y.-Q. Lan, J. Mater. Chem. A 6 (2018) 21969–21977.
[354] M. Asnavandi, B.H. Suryanto, W. Yang, X. Bo, C. Zhao, ACS Sustain. Chem. Eng. 6 (2018) 2866–2871.
[355] L. Yu, J. Zhang, Y. Dang, J. He, Z. Tobin, P. Kerns, Y. Dou, Y. Jiang, Y. He, S. L. Suib, ACS Catal. 9 (2019) 6919–6928.
[356] R. Subbaraman, D. Tripkovic, K.-C. Chang, D. Strmcnik, A.P. Paulikas, P. Hirunsit, M. Chan, J. Greeley, V. Stamenkovic, N.M. Markovic, Nat. Mater. 11 (2012) 550–557.
[357] K. Ye, Y.-Y. Li, R.-Z. Liao, RSC Adv. 6 (2016) 90035–90045.
[358] B. Mondal, K. Sengupta, A. Rana, A. Mahammed, M. Botoshansky, S.G. Dey, Z. Gross, A. Dey, Inorg. Chem. 52 (2013) 3381–3387.
[359] M. Chen, T.J. Smart, S. Wang, T. Kou, D. Lin, Y. Ping, Y. Li, J. Mater. Chem. A 8 (2020) 8783–8812.
[360] J. Greeley, T.F. Jaramillo, J. Bonde, I. Chorkendorff, J.K. Nørskov, Nat. Mater. 5 (2006) 909–913.
[361] B. Hinnemann, P.G. Moses, J. Bonde, K.P. Jørgensen, J.H. Nielsen, S. Horch, I. Chorkendorff, J.K. Nørskov, J. Am. Chem. Soc. 127 (2005) 5308–5309.
[362] C. Tsai, K. Chan, F. Abild-Pedersen, J.K. Nørskov, Phys. Chem. Chem. Phys. 16 (2014) 13156–13164.
[363] Q. Gong, L. Cheng, C. Liu, M. Zhang, Q. Feng, H. Ye, M. Zeng, L. Xie, Z. Liu, Y. Li, ACS Catal. 5 (2015) 2213–2219.
[364] H. Tang, K. Dou, C.-C. Kaun, Q. Kuang, S. Yang, J. Mater. Chem. A 2 (2014) 360–364.
[365] D. Kong, H. Wang, J.J. Cha, M. Pasta, K.J. Koski, J. Yao, Y. Cui, Nano Lett. 13 (2013) 1341–1347.
[366] Y. Tang, H. Yang, J. Sun, M. Xia, W. Guo, L. Yu, J. Yan, J. Zheng, L. Chang, F. Gao, Nanoscale 10 (2018) 10459–10466.
[367] Y. Yang, Y. Qian, H. Li, Z. Zhang, Y. Mu, D. Do, B. Zhou, J. Dong, W. Yan, Y. Qin, Sci. Adv. 6 (2020) eaba6586.

[368] L. Zhang, R. Si, H. Liu, N. Chen, Q. Wang, K. Adair, Z. Wang, J. Chen, Z. Song, J. Li, Nat. Commun. 10 (2019) 4936.
[369] X. Zheng, Y. Yao, W. Ye, P. Gao, Y. Liu, Chem. Eng. J. 413 (2021) 128027.
[370] L. Li, G. Zhang, B. Wang, T. Yang, S. Yang, J. Mater. Chem. A 8 (2020) 2090–2098.
[371] Y. Zhou, G. Gao, J. Kang, W. Chu, L.-W. Wang, Nanoscale 11 (2019) 18169–18175.
[372] X. Gao, Y. Zhou, Y. Tan, B. Yang, Z. Cheng, Z. Shen, Int. J. Hydrog. Energy 44 (2019) 14861–14868.
[373] V. Fung, G. Hu, Z. Wu, D.-E. Jiang, J. Phys. Chem. C 124 (2020) 19571–19578.
[374] X. Gao, Y. Zhou, Y. Tan, B. Yang, Z. Cheng, Z. Shen, J. Jia, Appl. Surf. Sci. 473 (2019) 770–776.
[375] C. Jian, W. Hong, Q. Cai, J. Li, W. Liu, Appl. Catal. B Environ. 266 (2020) 118649.
[376] I.S. Amiinu, Z. Pu, X. Liu, K.A. Owusu, H.G.R. Monestel, F.O. Boakye, H. Zhang, S. Mu, Adv. Funct. Mater. 27 (2017) 1702300.
[377] W. Chen, J. Pei, C.T. He, J. Wan, H. Ren, Y. Wang, J. Dong, K. Wu, W.C. Cheong, J. Mao, Adv. Mater. 30 (2018) 1800396.
[378] W. Chen, J. Pei, C.T. He, J. Wan, H. Ren, Y. Zhu, Y. Wang, J. Dong, S. Tian, W. C. Cheong, Angew. Chem. Int. Ed. 129 (2017) 16302–16306.
[379] D. Wang, Q. Li, C. Han, Z. Xing, X. Yang, Appl. Catal. B Environ. 249 (2019) 91–97.
[380] Z. Luo, Y. Ouyang, H. Zhang, M. Xiao, J. Ge, Z. Jiang, J. Wang, D. Tang, X. Cao, C. Liu, Nat. Commun. 9 (2018) 2120.
[381] J. Yin, J. Jin, H. Zhang, M. Lu, Y. Peng, B. Huang, P. Xi, C.H. Yan, Angew. Chem. Int. Ed. 131 (2019) 18849–18855.
[382] N. Yao, P. Li, Z. Zhou, Y. Zhao, G. Cheng, S. Chen, W. Luo, Adv. Energy Mater. 9 (2019) 1902449.
[383] H. Zhao, Z. Li, X. Dai, M. Cui, F. Nie, X. Zhang, Z. Ren, Z. Yang, Y. Gan, X. Yin, J. Mater. Chem. A 8 (2020) 6732–6739.
[384] W. Liu, J. Ji, X. Yan, W. Liu, Y.-C. Huang, K. Wang, P. Jin, X. Yao, J. Jiang, J. Mater. Chem. A 8 (2020) 5255–5262.
[385] R.W. Cross, N.Y. Dzade, Catalysts 10 (2020) 307.
[386] K. Eid, A.M. Abdullah, Electrochem. Commun. 136 (2022) 107237.
[387] Q. Peng, J. Rehman, K. Eid, A.S. Alofi, A. Laref, M.D. Albaqami, R.G. Alotabi, M. F. Shibl, Nanomaterials 12 (2022) 2825.
[388] K. Eid, Q. Lu, S. Abdel-Azeim, A. Soliman, A.M. Abdullah, A.M. Abdelgwad, R. P. Forbes, K.I. Ozoemena, R.S. Varma, M.F. Shibl, J. Mater. Chem. A 10 (2022) 1965–1975.
[389] M.A. Ahsan, T. He, K. Eid, A.M. Abdullah, M.F. Sanad, A. Aldalbahi, B. Alvarado-Tenorio, A. Du, A.R. Puente Santiago, J.C. Noveron, ACS Appl. Mater. Interfaces 14 (2022) 3919–3929.
[390] K. Eid, M.H. Sliem, M. Al-Ejji, A.M. Abdullah, M. Harfouche, R.S. Varma, ACS Appl. Mater. Interfaces 14 (2022) 40749–40760.
[391] K. Eid, A. Gamal, A.M. Abdullah, Green Chem. 25 (2023) 1276–1310.
[392] X. Gao, H. Liu, D. Wang, J. Zhang, Chem. Soc. Rev. 48 (2019) 908–936.